

RICE UNIVERSITY

Electron-positron pair production in Au+Au
collisions at a center-of-mass energy of 27 GeV per
nucleon pair as part of the Beam Energy Scan
Program at STAR

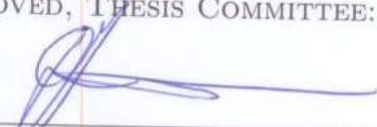
by

Joseph W. Butterworth

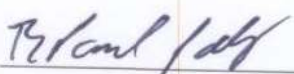
A THESIS SUBMITTED
IN PARTIAL FULFILLMENT OF THE
REQUIREMENTS FOR THE DEGREE

Doctor of Philosophy

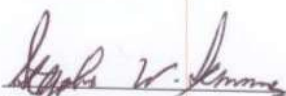
APPROVED, THESIS COMMITTEE:



Franciscus J.M. Geurts, Chair
Associate Professor of Physics and
Astronomy



Paul Padley
Professor of Physics and Astronomy
Associate Chair of the Undergraduate
Program



Stephen Semmes
Noah Harding Professor of Mathematics

Houston, Texas

April, 2017

ABSTRACT

Electron-positron pair production in Au+Au collisions at a center-of-mass energy of 27 GeV per nucleon pair as part of the Beam Energy Scan Program at STAR

by

Joseph W. Butterworth

This thesis reports the e^+e^- pair production in the top 80% most central Au on Au collisions at $\sqrt{s_{NN}} = 27$ GeV from the STAR experiment. The production exhibits an excess yield, in the low invariant mass region ($M_{ee} \lesssim 1.2 \text{ GeV}c^{-2}$), when compared to a hadronic cocktail without ρ contributions. We show that this excess yield is successfully described by model calculations that include a broadening of the ρ spectral function in a hot, dense medium. We also show agreement between the excess yield and model calculations, once detector acceptances have been corrected. Our results are a part of a larger systematic study of the e^+e^- pair production in the Relativistic Heavy Ion Collider Beam Energy Scan Program and are presented with data from Au on Au collisions at $\sqrt{s_{NN}} = 19.6, 39, 62.4, \text{ and } 200$ GeV. Each collision energy e^+e^- pair measurement has an excess yield with respect to a hadronic model without ρ contributions, and each excess yield is described by model calculations that include a broadening of the ρ spectral function in a hot, dense medium. This suggests that the ρ meson is modified by the hot, dense medium. We report the acceptance-corrected excess yields as a function of $\sqrt{s_{NN}}$, charged particle multiplicity, and predicted lifetimes. We also report that there is no statistically significant dependence of the excess yield on $\sqrt{s_{NN}}$, charged particle multiplicity, and predicted lifetimes for

Au on Au collisions with a 0–80% centrality.

Acknowledgments

First, I would like to acknowledge and thank Jennie, my family (Sharon, Steve, Mike, Dan, Amy K., Terry+boys), and all of my friends (especially James, Joey, Angel, and Yury) in being such a wonderful group of people that made graduate school a bit more fun.

I would also like to thank: my colleagues at the STAR Collaboration (*i.e.*, Jerome, Zhangbu, Gene, Wayne, Bill, the detector operators, TOF+MTD group, and others) for their hard work and kindness – without them, there would be no data for my thesis; the dielectron group (Chi, Shuai, Jie, Xin, Zebo, Yifei, Rongrong, Takahito, Florian, Tetyana, and others) for the many conversations about electron-positron pair production and for listening to me present on a semi-regular basis; Bingchu, Patrick, and Yi who were instrumental in systematically studying electron-positron production in the Beam Energy Scan program; Lijuan for her unsolicited support, recognition, and conversations – it has meant a great deal to me; the STAR Rice group (Bill, Daniel, Daniel, David, Geary, Jay, Kefeng, Pablo, Nick, and Ted) and Bonner Lab colleagues for the many conversations, distractions, and help along the way – it’s been fun; and my thesis and advising committee members (Professors Paul Padley, Stephen Semmes, Pat Hartigan, and Reggie Dufour) for guiding me through the thesis process.

Last, and certainly not least, a special thanks goes to Professor Geurts, my advisor/supervisor, who has supported and challenged me to do more than the bare minimum. Without him and his patience, the journey would not have been as fulfilling. I sincerely appreciate all his efforts and time. Cheers~

Contents

Abstract	ii
Acknowledgments	iv
List of Illustrations	viii
1 Introduction to heavy ion collisions and electromagnetic probes	1
1.1 Quantum Chromodynamics	1
1.1.1 Phase Diagram	17
1.1.2 Quark-Gluon Plasma	20
1.2 Evidence of the Quark-Gluon Plasma	21
1.3 Beam Energy Scan Program	26
1.4 Electromagnetic Probes	28
1.4.1 Introduction	28
1.4.2 Uses	29
1.4.3 Popular Topics	32
2 Theoretical Models	39
2.1 Introduction	39
2.2 Rho-Brown	39
2.3 Effective Many-body Theory by Rapp <i>et al.</i>	43
2.3.1 Thermal e^+e^- Production Rate	43
2.3.2 Chiral Symmetry Restoration Observable	49
2.4 Parton-Hadron-String Dynamics	50

2.4.1	Initial Collisions/Conditions	51
2.4.2	Formation of a Quark-Gluon Plasma	52
2.4.3	Partonic Stage – Quark-Gluon Plasma	52
2.4.4	Hadronization	53
2.4.5	Hadronic Stage	53
2.4.6	e^+e^- Production	54
2.5	Past Results	55
2.6	Goal for the Beam Energy Scan Program	59
3	Data Collection	63
3.1	RHIC	64
3.2	STAR	64
3.2.1	Trigger Systems	66
3.2.2	Time Projection Chamber	69
3.2.3	Time of Flight	73
4	Analysis	78
4.1	Event Selection	78
4.2	Track Selection	80
4.3	Electron Identification	81
4.3.1	Purity	83
4.4	e^+e^- Continuum	87
4.5	Efficiencies	94
4.5.1	Tracking	94
4.5.2	Matching	95
4.5.3	Electron Identification	98
4.5.4	Pair Formation	99
4.6	Systematic Uncertainties	102
4.6.1	Tracking	102

4.6.2	Matching	105
4.6.3	Electron Identification	106
4.6.4	Hadron Contamination	109
4.6.5	Charge Acceptance	112
4.6.6	Total Systematic Uncertainty	115
5	Hadronic Cocktail	117
5.1	Monte Carlo Cocktail	117
5.1.1	Parent Invariant Mass	118
5.1.2	Parent Rapidity	120
5.1.3	Parent Transverse Momentum	120
5.1.4	Parent Decay	124
5.1.5	Momentum Resolution	126
5.2	$c\bar{c}$ and Drell-Yan	129
5.3	Scaling	130
5.4	Cocktail Uncertainties	134
6	Results	137
6.1	Beam Energy Scan Program Results	144
6.2	Conclusions	150
6.3	Future Studies	154
	Bibliography	158

Illustrations

1.1	A quark (q) and anti-quark(\bar{q}) being pulled apart. As the pair is separated, the color field snaps and creates a new $q\bar{q}$ to keep the quarks confined. This figure was taken from [1].	3
1.2	The measurements of α_s as a function of Q . This figure was taken from [2].	4
1.3	An illustration of handedness. The massless fermion spin (s) is projected onto the direction of the momentum (\hat{p}). (Left) The direction of momentum and spin point in the same direction, which is a helicity of $+1/2$, or right-handed. (Right) The direction of momentum and spin point in the opposite directions, which is a helicity of $-1/2$, or left-handed.	7
1.4	The different potentials (V) based on the sign of μ^2 . The potential on the left represents the $\mu^2 > 0$ case and the potential on the right represents the $\mu^2 < 0$ case, where $\nu = \sqrt{\frac{-\mu^2}{\lambda}}$. This figure was taken from [1].	13
1.5	A ball sitting in a potential that is rotationally symmetric. This figure was taken from [3].	16
1.6	A conjectured phase diagram for QCD matter. This figure was taken from [4].	19
1.7	The evolution of a heavy ion collision. This figure was taken from [5].	21
1.8	History of the Universe from the Big Bang to present day. This figure was taken from [6].	22

1.9	The coordinate system used for making measurements at the STAR experiment. (a) Two heavy ions the moment before they collide. The momentum vector (P) is used to illustrate the coordinates with respect to the z -axis. (b) The transverse momentum vector is used to illustrate the coordinates with respect to the transverse plane. Also shown is a transverse view of two gold atoms colliding. The transverse distance between the centers of the nuclei is known as the impact parameter (b).	24
1.10	The dihadron azimuthal distributions of h^+h^- for $p + p$ collisions (bar graph), minimum bias $d+Au$ collisions (red points), $d+Au$ collisions of the top 20% centrality (green triangles), and central (0-5%) Au+Au collisions (blue stars). This figure was taken from [7].	25
1.11	(a) The elliptic flow v_2 for π , K_S^0 , p , and Λ as a function of p_T . (b) v_2 normalized by the number of quarks (n_q) for π , K_S^0 , p , and Λ as a function of p_T/n_q . This figure was taken from [8].	27
1.12	The ratio of hadron yields in Au+Au collisions at $\sqrt{s_{NN}} = 200$ GeV from STAR. The horizontal bars represent the statistical model fit to the ratios of hadron yields. This figure was taken from [9].	28
1.13	The relative yields to the photon transverse momentum/energy spectrum from different stages of the collision. This figure was created based on [10].	30
1.14	The chronological divisions of the e^+e^- invariant mass spectrum, where x fm/c represents the typical time ($c = 1$) after the start of the collision. This figure was taken from [11].	31
1.15	Sources of prompt photons: (a) quark anti-quark annihilation (b) quark gluon Compton scattering, and (c + d) quark fragmentation.	34

1.16	The estimated masses for the up, down, charm, strange, truth, and beauty quarks and the relative contribution to each mass from different mechanisms. The yellow bar represents the contribution to the mass from the breaking of chiral symmetry and the blue bar represents the contributions to the mass from the breaking of electroweak symmetry (Higgs mechanism). This figure was taken from [12].	37
2.1	Example self-energy diagrams that are considered a part of the in-medium ρ propagator. (a) The self-energy of the ρ and its pion cloud. (b) The self-energy of the ρ interacting with mesons, in this case, $a_1(1260)$. (c) The self-energy of the ρ interacting with baryons, in this case, $N^*(1520)$	45
2.2	The comparison of the e^+e^- yield normalized by the number of charged particles in the collision and the lifetime of the fireball as a function of $\sqrt{s_{NN}}$. The solid purple line represents the normalized total yield from the hadronic component (red short-dashed line) and the QGP component (yellow dashed line) with the quantity indicated by the left y-axis. The blue dot-dashed line is the fireball lifetime and the duration is indicated on the right y-axis. This figure was taken from [13].	49
2.3	The a_1 (red) and ρ (black) spectral functions at different temperatures. This figure was taken from [14].	51

- 2.4 (Left) The black solid points represent the e^+e^- invariant mass spectrum. The black solid line represents the hadronic cocktail (the summation of simulated known contributions to the e^+e^- continuum) with its components represented by the colored lines. (Right) The same invariant mass data are shown as black solid points with a dashed blue line representing hadronic cocktail calculations with a dropping ρ mass and a long-dashed red line representing hadronic cocktail calculations with a broadened ρ -spectral function. This figure was taken from [15]. 56
- 2.5 (Left) The solid red points represent the invariant mass measurement, while the solid red line connects the points. The other solid colored curves represent expected hadronic contributions to the $\mu^+\mu^-$ mass spectrum. The solid black triangles represent the difference between the data (red points) and the expected contributions (colored curves). (Right) The $\mu^+\mu^-$ invariant mass difference (solid black triangles) between the hadronic contributions and data points similar to (Left), but a different centrality selection. The curves show model predictions when using a broadened spectral function (Rapp/Wambach, solid blue curve), an unmodified spectral function (Vacuum ρ , dot-dashed red curve), a cocktail ρ based on the ratio $\rho/\omega = 1.2$ (cockt. ρ , solid red curve), and $D\bar{D} \rightarrow \mu^+\mu^-X$. This figure was taken from [16]. . . 57

2.6 (Left a) STAR’s e^+e^- invariant mass spectrum produced from 0-80% centrality Au+Au minimum-bias collisions at $\sqrt{s_{NN}} = 200$ GeV shown as the solid black points. The solid black curve represent the hadronic cocktail and the sum of the known hadronic sources (perforated multicolored curves) excluding ρ . (Left b) The solid black points represents the ratio of data to the hadronic cocktail. The solid red curve represents the ratio of the effective many-body theory plus the hadronic cocktail to the cocktail. The dashed blue curve represents the ratio of Parton-Hadron-String Dynamics (PHSD) plus the hadronic cocktail to the hadronic cocktail. (Right) PHENIX’s e^+e^- invariant mass spectrum produced from 0-92% centrality Au+Au minimum-bias collisions at $\sqrt{s_{NN}} = 200$ GeV shown as the solid black points. The hadronic cocktail without ρ contributions is represented by the dashed green curve. The contributions, ρ and QGP, from the effective many-body theory are shown as the dashed red and dashed blue lines, respectively. The solid black line represents the total expected contribution to the e^+e^- invariant mass spectrum. The left and right figures were taken from [17, 18], respectively. 59

2.7 The average chemical freeze-out temperature versus baryon chemical potential (bottom) and collision energy (top). The temperature is extracted from grand canonical ensemble fits to the ratio of particle yields. This figure was taken from [19]. 61

2.8 The ratio of protons and anti-protons to π^+ and π^- yields as a function of $\sqrt{s_{NN}}$ for different centralities. These ratios serve as an approximation of the total baryon density. The yields were taken from [19, 20]. 62

3.1	An aerial view of the Relativistic Heavy Ion Collider and the accelerator complex that supplies the gold ions to the RHIC. This figure was taken from [21].	65
3.2	An exploded view of the Solenoidal Tracker At RHIC (STAR), where sections of the detector are missing to illustrate different subsystems such as TOF. When taking data, the BBC and the end-cap electromagnetic calorimeter (EMMC) to the BBC's right are actually positioned directly against the barrel of STAR. This figure was taken from [22].	66
3.3	A schematic view of one of the BBCs. This figure was taken from [23].	67
3.4	The VPD subsystem. (a) The VPD assemblies. Each assembly is mounted with the beam pipe going through the center. (b) The hollow cylinder of each VPD assembly contains a photomultiplier tube (PMT) with a lead converter in front. This figure was taken from [24].	68
3.5	The physical location of the ZDC (the cross-hatched area in (a) and the red box in (b)) with respect to the beam pipes and interaction point (labeled "Intersection Point" in (b)). In this figure, ions are being collided. (a) The $x - y$ plane showing the beam pipes going into/out of the page. (b) The $z - x$ plane showing the beam pipes moving along the width of the page. This figure was taken from [25].	70
3.6	A schematic view of the Time Projection Chamber. This figure was taken from [26].	71
3.7	One sector of twelve that make up a TPC endcap. There are two endcaps, so the TPC consists of twenty-four sectors in total. This figure was taken from [26].	72

3.8	Side views of a TOF multi-resistive plate chamber. (Top) The short edge of an MRPC. The face of this side runs parallel with the beam pipe. (Bottom) The long side. The face of this side runs perpendicular to the beam pipe. This figure was taken from [27]. . . .	74
3.9	(Top) The positioning of a TOF tray on the outside of the TPC. (Bottom) The orientation of the MRPCs inside of a TOF tray, where the left side is positioned over the center of the TPC. This figure was taken from [28].	75
3.10	The β^{-1} as a function of momentum for particles from Au+Au collisions at $\sqrt{s_{NN}} = 27$ GeV. The dashed lines represent the expected β^{-1} for a given species. The corresponding species from bottom left to top right: e , π , K, p, and d.	76
4.1	(Left) The $n\sigma_e$ vs. momentum distribution for all quality tracks. (Right) The $n\sigma_e$ vs. momentum distribution for all quality tracks after rejecting the slow hadrons using the TOF system.	82
4.2	The $n\sigma_e$ distribution for quality tracks with a $n\sigma_\pi > 3$ in momentum (p) slice of 0.4 to 0.42 $\text{GeV}c^{-1}$. The yellow curve at $n\sigma_e \sim 2$ is the fit to the $\pi\pi$ peak, where the mean and width are used in the multi-Gaussian fit for the corresponding $\pi\pi$ Gaussian.	84
4.3	The raw yield counts for electrons as a function of momentum. The red and blue lines are the exponential extrapolations used to estimate the yield.	86
4.4	(Left) The raw yield counts for kaons as a function of momentum. The red line is the exponential extrapolation used to estimate the yield. (Right) The raw yield counts for protons as a function of momentum. The red line is the exponential extrapolation used to estimate the yield.	87

4.5	The electron purity as a function of momentum. The green region represents the systematic uncertainty of the purity derived from varying yield extrapolations. The gray shaded region represents the region where the yield totals have been extrapolated by exponential functions.	88
4.6	Invariant mass as a function of ϕ_v	89
4.7	The event plane angle Ψ_2 distribution before any corrections (blue), after re-centering (red), and after shifting (pink). The pink distribution is the event plane angle used for event pooling.	92
4.8	(Top) The raw invariant mass distributions normalized by the number of events for the e^+e^- (open points), correlated and combinatorial backgrounds (red histogram), and the signal (closed points). (Bottom) The ratio of the signal to background invariant mass distributions. The vertical error bars represent the statistical uncertainties and the horizontal error bars represent the bin width.	93
4.9	The matching efficiency as a function of p_T for electrons (red dot) and π (blue square). (Left) Negative charge. (Right) Positive charge. The uncertainties are statistical.	97
4.10	Electron identification efficiencies as a function of momentum. (Left) β^{-1} efficiencies for the count method (blue points) and the fit method (red points). The fit method is used as an alternative calculation for systematic uncertainty approximation and discussed in Sec. 4.6. (Right) The $n\sigma_e$ efficiencies by the fit method (open circles) and count method (brown crosses).	99
4.11	Flowchart for the Monte Carlo virtual photon generator used to create electron pair efficiencies from the single track efficiencies.	100

4.12	<p>ϕ_v efficiency as a function of invariant mass. The embedding ϕ_v efficiency from π^0 Dalitz decay based on the reconstructed track properties are used as the ϕ_v efficiencies in this analysis (open red points). An alternative embedding ϕ_v efficiency from π^0 Dalitz decays with the simulation values are also shown (solid black circles). Another alternative ϕ_v from the γ^* Monte Carlo are shown for comparison (open green squares).</p>	103
4.13	<p>The difference in (TPC fit points for tracking) efficiency calculations between the data and embedding driven methods as a function of transverse momentum. (Left) Electrons. (Right) Positrons. The uncertainties shown are statistical.</p>	104
4.14	<p>The difference in <i>TPC fit points for dE/dx</i> efficiency calculations between the data and embedding driven methods as a function of transverse momentum. (Left) Electrons. (Right) Positrons. The uncertainties shown are statistical.</p>	105
4.15	<p>The difference in <i>gDCA</i> efficiency calculations between the data and embedding driven methods as a function of transverse momentum. (Left) Electrons. (Right) Positrons. The uncertainties shown are statistical.</p>	106
4.16	<p>The difference in <i>matching</i> efficiency calculations between the scaled π and pure electron methods with respect to the scaled π efficiency as a function of transverse momentum. (Left) Electrons. (Right) Positrons. The uncertainties shown are statistical.</p>	107
4.17	<p>The difference between the fit method and count method “slow hadron rejection” efficiency calculations as a function of momentum. The straight line fit to the difference is used as the systematic uncertainty.</p>	108

4.18	The difference between the fit and count method efficiency calculations as a function of momentum. The different markers represent the absolute (red) and relative (blue with respect to the count method, pink with respect to the fit method) differences between the two methods.	109
4.19	The invariant mass distribution of K^+K^- (red square), K^+K^+ (blue triangle), K^+K^- (red triangle), the direct sum (pink triangle), and geometric mean (open square).	111
4.20	The invariant mass distribution of e^+e^- (red) and $h^+h^-/h^+e^-/h^-e^+$ (blue). The uncertainties are statistical only.	112
4.21	The relative systematic uncertainty of hadron contamination as a function of invariant mass. The quoted uncertainty in this analysis is from a similar study on Au+Au collisions at $\sqrt{s_{NN}} = 39$ GeV. For reference, the relative uncertainties from Au+Au collisions at $\sqrt{s_{NN}} = 27$ are shown for when the geometric mean was corrected with a charge acceptance correction (red square) and without a charge acceptance correction (blue open point). Vertical error bars shown are statistical.	113
4.22	The ratio e^+e^+ to e^-e^- as a function of invariant mass for pairs constructed from the same event and from mixed event samples. (Left) The ratio with a finer invariant mass binning for quality assurance. (Right) The ratio with the invariant mass binning used in the presentation of the final figures. The error bars are statistical uncertainties.	114
4.23	The systematic uncertainty of the charge-acceptance correction as a function of invariant mass.	114

4.24	The total systematic uncertainty as a function of the e^+e^- invariant mass for the top 80% most central Au+Au collisions at $\sqrt{s_{NN}} = 27$ GeV.	116
5.1	The Tsallis Blave Wave fits on π , K, p spectra from [19, 20].	122
5.2	The p_T resolution of the embedding sample as a function of p_T [GeVc $^{-1}$]. The p_T resolution is given as the Gaussian σ of $\left(\frac{p_T^{reco}-p_T^{sim}}{p_T^{reco}}\right)$ as a function of p_T . The red line is the result of fitting Eq. 5.31.	128
5.3	The double Crystal Ball function (Eq. 5.25) fit to $\frac{p_T^{reco}-p_T^{sim}}{p_T^{sim}}$ for p_T from 0.2 to 2.0 GeVc $^{-1}$	129
5.4	The $c\bar{c}$ cross-section measurements as a function of collision energy [29, 30, 31, 32, 33]. The dashed curves represent the upper and lower limits of the FONLL predictions [34] and the red curve is the upper FONLL limit curve fitted to the measurements.	133
5.5	The e^+e^- invariant mass distribution from $c\bar{c}$ decays with different assumptions for the correlation between the daughters. The black solid line is the distribution as is from PYTHIA. The red dot-dashed line is the distribution after randomizing each daughter's ϕ . The green dashed line is the distribution after randomizing both ϕ and η for each daughter. The blue dotted line is the distribution after randomizing each daughter's ϕ , η , and p_T	136

- 6.1 (Top) The corrected e^+e^- invariant mass spectrum (blue points) in the STAR detector acceptance. For comparison, the hadronic cocktail is shown as the solid black curve. (Bottom) The ratio of the measurements (*i.e.*, data) to cocktail as a function of invariant mass. The error bars represent the statistical uncertainties. The open boxes represent the systematic uncertainties. The gray band represents the cocktail uncertainties. 138
- 6.2 (Top) The corrected e^+e^- invariant mass spectrum (black points) in the STAR detector acceptance shown with e^+e^- contributions from the hadronic cocktail (solid black curve), the QGP (blue dashed curve), ρ with a broadened spectral function (HG_med/pink dashed curve), and the sum of the calculations (red solid curve). The QGP and ρ calculations have been provided by Rapp *et al.* [35, 36]. 139
- 6.3 The comparison of the hadronic cocktail plus contributions from Rapp *et al.* over the hadronic cocktail and data over the hadronic cocktail as a function of invariant mass. The cocktail uncertainties are represented by the gray band. The data statistical and systematic uncertainties are represented by the error bars and open boxes, respectively. 140
- 6.4 The STAR detector acceptance correction factor as a function of invariant mass and transverse momentum. 141
- 6.5 The relative difference between the STAR detector acceptance effect from the γ^* Monte Carlo simulation in Sec. 4.5.4 and Rapp *et al.*'s STAR detector acceptance effect with respect to the γ^* Monte Carlo simulation. To be conservative, a flat 6% systematic uncertainty is used. 142

- 6.6 The acceptance-corrected excess yields, normalized by dN_{ch}/dy at mid-rapidity, as a function of invariant mass shown as the black points with statistical and systematic uncertainties as the error bars and open boxes, respectively. Model calculations by Rapp *et al.* are also shown to make comparisons with the data. Their calculations (red line, “Sum”) consist of contributions from the ρ (blue short-dashed line, “HG_med”), which has a spectral function that is modified by the hot, dense medium, and the QGP (pink long-dashed line, “QGP”). 143
- 6.7 (Left) The top panel contains the e^+e^- invariant mass spectrum in the STAR acceptance ($p_T^e > 0.2 \text{ GeV}c^{-1}$, $p_T^e < 3 \text{ GeV}c^{-1}$, $|\eta^e| < 1$, and $|Y^{ee}| < 1$) with a hadronic cocktail and calculations from Rapp *et al.* The bottom panel contains the ratio of data to cocktail as a function of invariant mass and the ratio of calculations from Rapp *et al.*+cocktail to cocktail as a function of invariant mass. The statistical and systematic uncertainties are represented by the error bars and green boxes, respectively. The hadronic cocktail uncertainties are represented by the gray band. (Right) The acceptance-corrected excess yields, which have been normalized by dN_{ch}/dy , as a function of invariant mass, with theory calculations. The excess yields in Au+Au at $\sqrt{s_{NN}} = 19.6 \text{ GeV}$ are from [37]. The excess yields in Au+Au at $\sqrt{s_{NN}} = 200 \text{ GeV}$ are from [17, 38]. The excess yields in In+In are from [16, 39]. Both figures are from [37]. . . 145

- 6.8 (Left) The corrected e^+e^- invariant mass spectrum within the STAR acceptance for Au+Au collisions at $\sqrt{s_{NN}} = 27, 39, \text{ and } 62.4 \text{ GeV}$ with the hadronic cocktail for Au+Au at $\sqrt{s_{NN}} = 62.4 \text{ GeV}$ added for reference. (Middle) The ratio of the data to the cocktail as a function on invariant mass as represented by the blue points. The ratio of the cocktail plus contributions from the Rapp *et al.* calculations to the cocktail as a function of invariant mass as represented by the red curve. (Right) The acceptance-corrected excess yields, normalized by dN_{ch}/dy at mid-rapidity, as a function of invariant mass are shown as black points. Calculations by Rapp *et al.* are added to the cocktail to give the *Sum* of contributions to the e^+e^- invariant mass spectrum as shown by the red curve. The calculations for the contributions from the ρ , which is modeled with a spectral function that is modified by the medium, and the QGP. The statistical and systematic uncertainties are represented by the error bars and open boxes, respectively. Cocktail uncertainties are represented by the gray bands. 146
- 6.9 The acceptance-corrected excess yields, normalized by dN_{ch}/dy , integrated over 0.4 to 0.75 $\text{GeV}c^{-2}$ as a function of collision energy (closed markers). The data points are from STAR's Au+Au collisions at $\sqrt{s_{NN}} = 19.6, 27, 39, 62.4, \text{ and } 200 \text{ GeV}$ and NA60's In+In collisions at $\sqrt{s_{NN}} = 17.3 \text{ GeV}$. The statistical and systematic uncertainties are represented as the error bars and boxes, respectively. The corresponding model calculations by Rapp *et al.* are shown for comparison (open circles). 149

- 6.10 The acceptance-corrected excess yields, normalized by dN_{ch}/dy , integrated over 0.4 to 0.75 GeVc⁻² as a function of dN_{ch}/dy . The data points are from STAR's Au+Au collisions at $\sqrt{s_{NN}} = 19.6, 27, 39, 62.4, \text{ and } 200$ GeV with 0-80% centrality, STAR's Au+Au collisions at $\sqrt{s_{NN}} = 200$ GeV with centralities of 40-80%, 10-40%, and 0-10% (red squares), and NA60's In+In collisions at $\sqrt{s_{NN}} = 17.3$ GeV. The statistical and systematic uncertainties are represented as the error bars and boxes, respectively. 150
- 6.11 The acceptance-corrected excess yields, normalized by dN_{ch}/dy , integrated over 0.4 to 0.75 GeVc⁻² as a function of predicted fireball lifetimes by Rapp *et al.* The data points are from STAR's Au+Au collisions at $\sqrt{s_{NN}} = 19.6, 27, 39, 62.4, \text{ and } 200$ GeV with 0-80% centrality, STAR's Au+Au collisions at $\sqrt{s_{NN}} = 200$ GeV with centralities of 40-80%, 10-40%, and 0-10% (red squares), and NA60's In+In collisions at $\sqrt{s_{NN}} = 17.3$ GeV. The predicted yields by Rapp *et al.*, normalized by dN_{ch}/dy , integrated from 0.4 to 0.75 GeVc⁻¹ are plotted against predicted fireball lifetimes for comparison. The statistical and systematic uncertainties are represented as the error bars and boxes, respectively. 152
- 6.12 (Left) The e⁺e⁻ excess yield from Au+Au collisions at $\sqrt{s_{NN}} = 19.6$ GeV. (Right) The acceptance-corrected excess yields, normalized by dN_{π}/dy , integrated over 0.4 to 0.75 GeVc⁻² as a function of collision energy. The red points are actual measurements, while the blue points are the 19.6 GeV value projected on the Phase II collision energies with the expected uncertainties with iTPC and more collisions. The statistical and systematic uncertainties are represented by the error bars and open brackets, respectively. For details, please refer to the text. The left and right figures are from [40, 41], respectively. 157

Chapter 1

Introduction to heavy ion collisions and electromagnetic probes

The aim of this thesis is to search for and study modifications to the ρ -meson invariant mass spectrum through the reconstruction of electron-positron pairs, e^+e^- , that have been produced during the collision of gold (Au) ions at a center-of-mass energy per nucleon pair of 27 GeV. An introduction to the collisions of heavy ions and electromagnetic probes is discussed in this chapter. The following chapters cover the theoretical motivation (Chapter 2), data collection (Chapter 3), data analysis (Chapter 4), modeling of known hadronic contributions (Chapter 5), and conclusions (Chapter 6).

1.1 Quantum Chromodynamics

Quantum chromodynamics (QCD) is a theory that describes the strong interaction (*i.e.*, force) between quarks and gluons, where the strong interaction is carried by gluons. There are six types (*i.e.*, flavors) of quarks: up (u), down (d), charm (c), strange (s), truth (t), and beauty (b). Quarks are fermions because they have a spin of $1/2$ and follow Fermi-Dirac statistics. Quarks also possess a fractional baryon charge of $+1/3$ (B) and a fractional electric charge such that u , c , and t have a fraction electric charge of $+2/3$ elementary charge (e) and d , s , and b have a fractional electric charge of $-1/3 e$. Anti-quarks have opposite baryon and electric charges. Gluons have a spin of 1, like the electromagnetic force carrier, the photon. Gluons carry no electric

charge. Both quarks and gluons carry color-charges (referred to simply as “color”). Color is a property of the particle that explains how quark combinations and gluon combinations can satisfy the Pauli exclusion principle (*e.g.*, the color property allows all three u quarks to form a Δ^{++} baryon – this combination of quarks would violate the Pauli exclusion principle without the color property to distinguish the u quarks [46]). Each quark flavor comes in three colors (red, green, and blue). Gluons carry both color and anti-color, whereas quarks carry color and anti-quarks carry anti-color. For gluons, there are nine possible combinations of colors and anti-colors, which can be arranged into a color octet and a color singlet that is color neutral. Since a colorless gluon has not been observed and a colorless gluon does not carry color between quarks, there are only eight colored states possible for gluons to carry.

QCD has two defining features: confinement and asymptotic freedom. Confinement is the feature where quarks are not found alone, but found bound together as colorless particles called hadrons. A hadron with a quark-antiquark pair is known as a meson (*e.g.*, π , ρ , and $a_1(1260)$), and a hadron with a quark-quark-quark triplet is known as a baryon (*e.g.*, proton, neutron, and Δ^{++}). An example of confinement in the laboratory setting is a jet, which essentially is a collimated shower of hadrons. One method to produce a jet is to collide an electron (e^-) and positron (e^+) head-on. In some collisions, the electron and positron annihilate into a photon (γ) that decays into a $q\bar{q}$ pair (*i.e.*, $\gamma \rightarrow q\bar{q}$). The $q\bar{q}$ pair then separates and as the distance between the pair grows, so does the strong interaction between the pair. It becomes energetically favorable for the color field (gluon) between quarks to snap and, at the snapping point, a new $q\bar{q}$ forms in-between the original pair. The new pair ensures that the overall collision system remains colorless and quarks are not found alone. This process will continue to repeat and create many hadrons in the directions of

the original q and \bar{q} . Ultimately, resulting in a pair of jets (*i.e.*, a dijet). Figure 1.1 illustrates a $q\bar{q}$ pair being separated and the creation of $q\bar{q}$ pairs as the original pair is pulled apart.

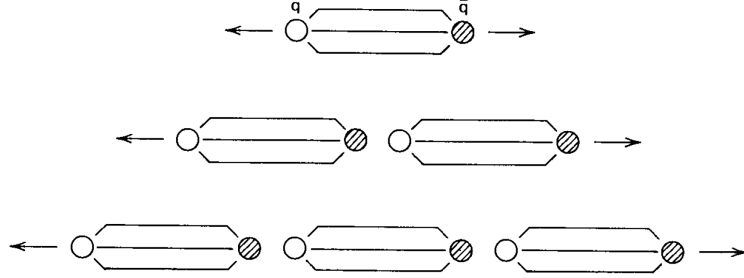


Figure 1.1 : A quark (q) and anti-quark(\bar{q}) being pulled apart. As the pair is separated, the color field snaps and creates a new $q\bar{q}$ to keep the quarks confined. This figure was taken from [1].

The other feature of QCD, asymptotic freedom, is a property that describes the ability of quarks to move around freely at short distances, *e.g.*, inside a hadron. This feature is confirmed by measuring the strong coupling constant (α_s) for different interaction ranges, where the strong coupling constant describes the strength of the strong force at some distance. Measurements are performed as a function of momentum transfer (Q^2), which corresponds to the interaction range. In Fig. 1.2, measurements of α_s are shown as a function of Q . The coupling constant decreases as Q increases. The decrease in α_s at small interaction distances supports the feature of asymptotic freedom, where quarks move around freely at short distances. The behavior of α_s (*i.e.*, the slope of α_s) is known as “running”. Hence, α_s is a running coupling constant.

The dynamics of QCD is described by the QCD Lagrangian,

$$\mathcal{L}_{QCD} = \sum_q \bar{\Psi}_q (i\not{D} - M) \Psi_q - \frac{1}{4} F^{\mu\nu} F_{\mu\nu}, \quad (1.1)$$

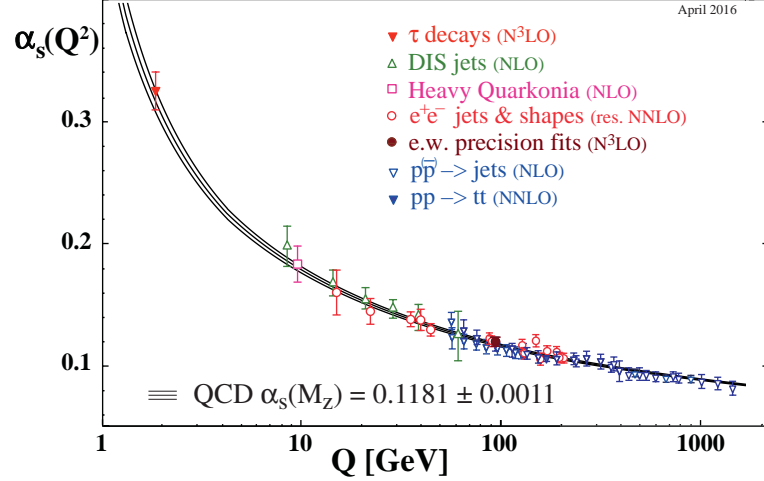


Figure 1.2 : The measurements of α_s as a function of Q . This figure was taken from [2].

where q is the quark flavor (u, d, \dots) index, Ψ_q is a Dirac spinor representing the quark field, i is the imaginary unit, $\not{D} = \gamma_\mu D_\mu$, γ_μ is a Dirac γ -matrix, and D_μ is a covariant derivative defined as $\partial_\mu - igG_\mu$, $F_{\mu\nu} = \partial_\mu G_\nu - \partial_\nu G_\mu + ig[G_\mu G_\nu]$ representing a gluon field tensor, G_ν represents a gluon field, μ and ν are space-time indexes, g is the coupling constant, and M is the mass matrix for the six quark flavors and is defined as

$$M = \begin{pmatrix} m_u & 0 & 0 & 0 & 0 & 0 \\ 0 & m_d & 0 & 0 & 0 & 0 \\ 0 & 0 & m_s & 0 & 0 & 0 \\ 0 & 0 & 0 & m_c & 0 & 0 \\ 0 & 0 & 0 & 0 & m_b & 0 \\ 0 & 0 & 0 & 0 & 0 & m_t \end{pmatrix}, \quad (1.2)$$

where m is the mass and the subscript on m is the quark flavor. Each Ψ_q represents three colors (red, green, and blue) for each quark flavor (*i.e.*, Ψ_q^c , where $c = \text{red, green, blue}$), and each $G_\nu = G_\nu^a \lambda^a / 2$ represents the eight possible color states such that a is the color index and λ^a are the 3×3 Gell-Mann matrices [47]

$$\begin{aligned} \lambda_1 &= \begin{pmatrix} 0 & 1 & 0 \\ 1 & 0 & 0 \\ 0 & 0 & 0 \end{pmatrix}, \lambda_2 = \begin{pmatrix} 0 & -i & 0 \\ i & 0 & 0 \\ 0 & 0 & 0 \end{pmatrix}, \lambda_3 = \begin{pmatrix} 1 & 0 & 0 \\ 0 & -1 & 0 \\ 0 & 0 & 0 \end{pmatrix}, \\ \lambda_4 &= \begin{pmatrix} 0 & 0 & 1 \\ 0 & 0 & 0 \\ 1 & 0 & 0 \end{pmatrix}, \lambda_5 = \begin{pmatrix} 0 & 0 & -i \\ 0 & 0 & 0 \\ i & 0 & 0 \end{pmatrix}, \lambda_6 = \begin{pmatrix} 0 & 0 & 0 \\ 0 & 0 & 1 \\ 0 & 1 & 0 \end{pmatrix}, \\ \lambda_7 &= \begin{pmatrix} 0 & 0 & 0 \\ 0 & 0 & -i \\ 0 & i & 0 \end{pmatrix}, \lambda_8 = \frac{1}{\sqrt{3}} \begin{pmatrix} 1 & 0 & 0 \\ 0 & 1 & 0 \\ 0 & 0 & -2 \end{pmatrix}. \end{aligned} \quad (1.3)$$

QCD is symmetrical when it comes to color, is approximately symmetrical for flavor transformations, and has a symmetry that distinguishes confinement and deconfinement. The color symmetry is described the Lie group $SU(3)$ (*i.e.*, special unitary group of degree 3) and the symmetry ($SU(3)_{color}$) is invariant under local color transformations [48]

$$S(x) = e^{ig\Theta^a(x)\lambda^a/2}, \quad (1.4)$$

where λ^a are the Gell-Mann matrices, Θ^a are arbitrary real numbers, g is the coupling constant, and a is the gluon color-anticolor index. The Dirac spinor (Ψ) transforms as

$$\Psi \rightarrow S(x)\Psi, \quad (1.5)$$

and the gluon field (G_μ) transforms as

$$G_\mu \rightarrow S(x) \left(G_\mu + \frac{i}{g} \partial_\mu^x \right) S^\dagger(x). \quad (1.6)$$

The approximate flavor symmetry is described by the Lie groups $U(3)_L \times U(3)_R$ [48] (*i.e.*, unitary groups of degree 3, where L and R correspond to left- and right-handed) that is made possible by the low mass of the quark flavors u , d , and s . The u and d quarks have masses of about 2 and 6 $\text{MeV}c^{-2}$, respectively, and the s quark has a mass of about 100 $\text{MeV}c^{-2}$. Since the masses are low, the masses may be ignored in a first order approximation of the Lagrangian for u , d , and s . The QCD Lagrangian becomes

$$\mathcal{L}_{QCD} = \bar{\Psi} i \not{D} \Psi - \frac{1}{4} F^{\mu\nu} F_{\mu\nu}, \quad (1.7)$$

where Ψ is now a collection of the three quark fields ($u(x), d(x), s(x)$). The Lagrangian can be manipulated further by splitting Ψ into left- and right-handed components.

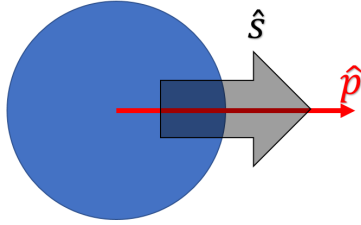
Handedness, in the case of massless fermions, refers to the helicity of the particle, where the helicity operator projects spin onto the momentum direction. There are two eigenvalues $+1/2$ and $-1/2$, which correspond to right and left handed, respectively. The handedness is shown in Fig. 1.3. The left-handed Ψ is denoted as Ψ_L and the right-handed Ψ is denoted as Ψ_R , where $\Psi_L + \Psi_R = \Psi$, $\Psi_L = 0.5(1-\gamma^5)\Psi$, and $\Psi_R = 0.5(1+\gamma^5)\Psi$. The γ^5 is a product of the Dirac γ -matrices and is defined as

$$\gamma^5 \equiv i\gamma^0\gamma^1\gamma^2\gamma^3 = \begin{pmatrix} 0 & 1 \\ 1 & 0 \end{pmatrix}. \quad (1.8)$$

The splitting of Ψ into left- and right-handed components allows the Lagrangian to be rewritten as

$$\mathcal{L}_{QCD} = \bar{\Psi}_L i \not{D} \Psi_L + \bar{\Psi}_R i \not{D} \Psi_R - \frac{1}{4} F^{\mu\nu} F_{\mu\nu}. \quad (1.9)$$

Right Handed



Left Handed

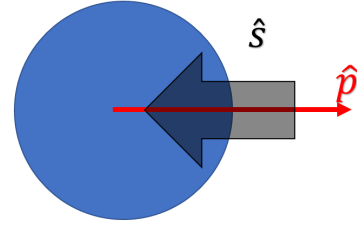


Figure 1.3 : An illustration of handedness. The massless fermion spin (s) is projected onto the direction of the momentum (\hat{p}). (Left) The direction of momentum and spin point in the same direction, which is a helicity of $+1/2$, or right-handed. (Right) The direction of momentum and spin point in the opposite directions, which is a helicity of $-1/2$, or left-handed.

By splitting \mathcal{L}_{QCD} , it becomes apparent that the gluons interact with the quarks irrespective of their handedness (*i.e.*, the same coupling constant for both cases) and the handedness of the quark does not change through the QCD interaction. And since the mass of the quark flavors are ignored, each handed quark field may be replaced with another handed quark field of a different flavor and same handedness. By being able to mix quark flavors within their set of handedness, this suggests that there is a $U(3)_L \times U(3)_R$ symmetry present [48]. The $U(3)_L \times U(3)_R$ symmetry can be rewritten as

$$U(3)_L \times U(3)_R = U_V(1) \times U_A(1) \times SU_V(3) \times SU_A(3), \quad (1.10)$$

where the subscripts A and V correspond to the type of currents the fields couple to and that is axial ($\gamma^\mu \gamma^5$) and vector (γ^μ), respectively. Each symmetry group (*i.e.*, $U_V(1)$, $U_A(1)$, $SU_V(3)$, and $SU_A(3)$) has a different physical consequence and is discussed in the immediately preceding text.

The $U_V(1)$ symmetry is the result of the Lagrangian being invariant to a global

phase transformation to all quark flavors, where Ψ transforms as

$$\Psi \rightarrow e^{i\vec{\Theta}}\Psi \quad (1.11)$$

and $\vec{\Theta}$ is an arbitrary constant vector. The invariance holds true in both cases of the quarks being massless and having mass, and the physical consequence of the $U_V(1)$ symmetry is baryon number conservation.

The $U_A(1)$ symmetry is the result of the Lagrangian being invariant to a global axial phase transformation to all quark flavors, where Ψ transforms as

$$\Psi \rightarrow e^{i\vec{\Theta}\gamma^5}\Psi. \quad (1.12)$$

In the massless quark scenario, this transformation is invariant when applied to the classical Lagrangian. However, when applied in a full quantum approach, the transformation is no longer invariant and the associated current diverges. The divergence arises from quantum corrections and is referred to as the axial anomaly. The quantum anomaly is responsible for intrinsic parity violation [49], where intrinsic parity ($P \times (-1)^s$) is the parity quantum number (P) with the spatial configuration considered through its spin (s). Parity violation occurs when the initial and final intrinsic parities do not equate. Examples of the intrinsic parity violation includes $\omega \rightarrow \pi\pi\pi$ and $K^* \rightarrow K\pi\pi$ [48, 49]. In the process $\omega \rightarrow \pi\pi\pi$, ω has an intrinsic parity of +1 and 3π has an intrinsic parity of -1. In the process $K^* \rightarrow K\pi\pi$, K^* has an intrinsic parity of +1, and $K\pi\pi$ has an intrinsic parity of -1. In both cases, the intrinsic parity is not conserved.

The $SU_V(3) \times SU_A(3)$ symmetries are present in the massless QCD Lagrangian, as the Lagrangian is invariant to both vector and axial transformations in the massless scenario. The vector transformation rotates Ψ as

$$\Psi \rightarrow e^{i\vec{\Theta}\cdot\frac{\lambda}{2}}\Psi, \quad (1.13)$$

where λ are the Gell-Mann matrices and Θ are the components of an arbitrary vector. The vector transformation is also invariant in the scenario where quarks have masses. The physical consequences of the $SU_V(3)$ symmetry are the multiplets of hadrons with constituent light quarks (*e.g.*, the mesons: π^0 , π^+ , π^- , K^+ , K^- , K^0 , \bar{K}^0 , and η and the baryons: p , n , Λ , Σ^+ , Σ^0 , Σ^- , Ξ^0 , and Ξ^-). The axial transformation of Ψ follows

$$\Psi \rightarrow e^{i\vec{\Theta} \cdot \frac{\lambda}{2} \gamma^5} \Psi. \quad (1.14)$$

When the transformation is applied to the QCD Lagrangian with mass, Eq. 1.1, the invariance is broken and is an explicit breaking of the symmetry. There is also a spontaneous breaking of the symmetry, too. The physical consequences of the $SU_A(3)$ symmetry breaking are the absence of degenerate states with opposite parity and the creation of the π , K , and η . The degenerate states of opposite parity, also known as chiral partners, would be between pairs of pseudoscalar & scalar mesons (*e.g.*, π and σ , respectively) and vector & axial-vector mesons (*e.g.*, ρ and $a_1(1260)$, respectively). However, there are no observed degenerate states and an invariant mass difference is observed between the partners. For example, ρ has a mass of 775 MeVc^{-2} and $a_1(1260)$ has a mass of 1230 MeVc^{-2} . A mass difference, or splitting, of 455 MeVc^{-2} .

Finally, the massless \mathcal{L}_{QCD} is scale invariant [49]. Scale invariance is when the action (S) is invariant under a scale transformation, where the quark fields ($\psi(x)$), and gluon fields (G_μ), and space-time (x) variables transform as

$$x \rightarrow x' = e^{-\lambda x}, \psi(x) \rightarrow \psi'(x') = e^{3\lambda/(2x)} \psi(x), G_\mu(x) \rightarrow G'_\mu = e^\lambda G_\mu(x). \quad (1.15)$$

The new action (S') follows:

$$S' = \int d^4x \mathcal{L}'(x) = \int d^4\lambda^4 \mathcal{L}(\lambda x) = S. \quad (1.16)$$

Hence, it is scale invariant. However, there is a “trace anomaly”. QCD must be renormalized, and the scale defined for QCD (Λ_{QCD}) is set making the full QCD not scale invariant. There is an associated order parameter with the anomaly and that is the expectation value of the energy-momentum tensor ($\langle\Theta_\mu^\mu\rangle$) given by

$$\langle\Theta_\mu^\mu\rangle = \frac{\beta_{QCD}}{2g^3} \langle\text{Tr}F_{\mu\nu}F^{\mu\nu}\rangle + \sum_{q=u,d,s} m_q (1 + \gamma) \langle\bar{\psi}\psi\rangle, \quad (1.17)$$

where β_{QCD} is the beta function of QCD, g^3 is the $SU(3)$ gauge coupling constant, m_q is the quark flavor (q) mass, and γ is the anomalous dimension. The first term is the dominate contribution and contains the gluon condensate

Chiral Partners

Chiral partners are pairs of hadrons that rotate into one another under a chiral rotation. One such pair is the axial-vector meson $a_1(1260)$ and the vector meson ρ . To demonstrate that these two mesons are partners, ρ and a_1 -like states can be constructed out of quark fields and then rotated into one another [3]. This is done in the scenario where only two quark flavors, the u and d flavors, are considered. Since the s quark is not considered, the $SU(3)_V \times SU(3)_A$ symmetry is no longer applicable, but $SU(2)_V \times SU(2)_A$ symmetry is applicable in a similar fashion. Instead of the Gell-Mann matrices and Ψ being a collection of three quark fields, the \mathcal{L}_{QCD} may be approximated with a two quark flavor version that contains the three 2×2 Pauli matrices ($\vec{\tau}$)

$$\tau_1 = \begin{pmatrix} 0 & 1 \\ 1 & 0 \end{pmatrix}, \tau_2 = \begin{pmatrix} 0 & -i \\ i & 0 \end{pmatrix}, \tau_3 = \begin{pmatrix} 1 & 0 \\ 0 & -1 \end{pmatrix}, \quad (1.18)$$

and Ψ is a collection quark fields $u(x)$ and $d(x)$, respectively. The vector and axial-vector transformations (R_V and R_A) are analogous to their three quark flavor coun-

terparts, where Eqs. 1.13 and 1.14 now transform as

$$\begin{aligned}\Psi &\rightarrow e^{i\vec{\theta}\cdot\frac{\vec{\tau}}{2}}\Psi, \\ \Psi &\rightarrow e^{i\vec{\theta}\cdot\frac{\vec{\tau}}{2}\gamma^5}\Psi,\end{aligned}\tag{1.19}$$

respectively.

The ρ -like state ($\vec{\rho}_\mu$) can be described by $\vec{\rho}_\mu = \frac{1}{\sqrt{2}}\bar{\psi}\gamma_\mu\vec{\tau}\psi$, where μ is a space-time index, ψ and $\bar{\psi}$ represent quark and anti-quark fields (*i.e.*, a meson), respectively, and $\gamma_\mu\vec{\tau}$ means that the state transforms like a vector particle (*i.e.*, vector meson). The $a_1(1260)$ -like state ($\vec{a}_{1\mu}$) is described by $\vec{a}_{1\mu} = \frac{1}{\sqrt{2}}\bar{\psi}\gamma_\mu\vec{\tau}\gamma_5\psi$, where the where μ is a space-time index, ψ and $\bar{\psi}$ represent quark and anti-quark fields (*i.e.*, a meson), respectively, and $\gamma_\mu\vec{\tau}\gamma^5$ means that the state transforms like an axial-vector particle (*i.e.*, axial-vector meson).

Rotating $\vec{\rho}_\mu$ with R_V is as follows:

$$\begin{aligned}R_V\vec{\rho}_\mu &= \frac{1}{\sqrt{2}}R_V\bar{\psi}\gamma_\mu\vec{\tau}R_V\psi \\ &= \frac{1}{\sqrt{2}}\bar{\psi}e^{i\theta\frac{\vec{\tau}}{2}}\gamma_\mu\vec{\tau}e^{-i\theta\frac{\vec{\tau}}{2}}\psi = \frac{1}{\sqrt{2}}\psi^\dagger\left(1+i\theta^j\frac{\tau^j}{2}\right)\gamma_0\gamma_\mu\tau^i\left(1-i\theta^j\frac{\tau^j}{2}\right)\psi \\ &= \frac{1}{\sqrt{2}}\bar{\psi}\gamma_\mu\tau^i\psi - \frac{1}{\sqrt{2}}\frac{1}{2}\bar{\psi}\gamma_\mu\tau^i i\tau^j\theta^j\psi + \frac{1}{\sqrt{2}}\frac{1}{2}\bar{\psi}\gamma_\mu i\tau^j\theta^j\tau^i\psi \\ &= \vec{\rho} + \theta^j\epsilon_{ijk}\frac{1}{\sqrt{2}}\bar{\psi}\gamma_\mu\tau^k\psi \\ &= \vec{\rho} + \vec{\theta} \times \vec{\rho},\end{aligned}\tag{1.20}$$

where $\bar{\psi} = \psi^\dagger\gamma_0$, $e^{-i\theta\frac{\vec{\tau}}{2}} \simeq 1 - i\vec{\tau}\frac{\theta}{2}$, $\gamma_0\gamma_5 = -\gamma_5\gamma_0$, and $[\tau^i, \tau^j] = 2i\epsilon_{ijk}\tau^k$. The vector transformation rotates the ρ into itself. However, when rotating $\vec{\rho}_\mu$ with R_A as follows:

$$\begin{aligned}
R_A \vec{\rho}_\mu &= \frac{1}{\sqrt{2}} R_A \bar{\psi} \gamma_\mu \vec{\tau} R_A \psi \\
&= \frac{1}{\sqrt{2}} \psi^\dagger \left(1 + i \gamma_5 \theta^j \frac{\tau^j}{2} \right) \gamma_0 \gamma_\mu \tau^i \left(1 - i \gamma_5 \theta^j \frac{\tau^j}{2} \right) \psi \\
&= \frac{1}{\sqrt{2}} \left[\bar{\psi} \gamma_\mu \tau^i \psi + \psi^\dagger \left(i \frac{1}{2} \tau^j \theta^j \tau^i \gamma_0 \gamma_\mu \gamma_5 - i \frac{1}{2} \gamma_0 \gamma_\mu \gamma_5 \tau^i \tau^j \theta^j \right) \psi \right] \quad (1.21) \\
&= \vec{\rho}_\mu + \frac{i}{\sqrt{2}} \bar{\psi} \gamma_\mu \gamma_5 \theta^j \frac{1}{2} (\tau^j \tau^i - \tau^i \tau^j) \psi = \vec{\rho}_\mu + \frac{i}{\sqrt{2}} \theta^j (-i \varepsilon_{ijk}) \bar{\psi} \gamma_\mu \gamma_5 \tau^k \psi \\
&= \vec{\rho}_\mu + \vec{\theta} \times \vec{a}_{1\mu},
\end{aligned}$$

the ρ no longer rotates into itself, but the axial rotation causes the ρ to rotate into the a_1 . Similar transformations can be performed on $\vec{a}_{1\mu}$ and the a_1 will rotate into the ρ , too. This relationship (*i.e.*, symmetry) between the ρ and a_1 also implies that the two mesons should share the same eigenvalues, or mass values. This is also referred to as degeneracy. However, the ρ and a_1 have not been observed to have the same mass. This example has shown that the $\rho(770)$ and $a_1(1260)$ are indeed chiral partners and, yet, exhibit different masses than the symmetry suggests. This mass difference (*i.e.*, no degeneracy) is a result of the spontaneous breaking of the chiral symmetry. For more information about the axial and vector operators with respect to chiral symmetry, see [3].

Spontaneous Symmetry Breaking

Spontaneous symmetry breaking occurs when a symmetry is not realized in the ground state of the Hamiltonian, but in an excited state. This symmetry when broken is also referred to as hidden symmetry and, with respect to $SU(3)_A$, is responsible for the non-degenerate chiral partners (*e.g.*, ρ & $a_1(1260)$ and the mesons σ & π) and creation of the π , K , and η mesons. The creation of π , K , and η are a result of the

phenomena called Goldstone modes. Goldstone modes are the massless states in an excited spectrum when a continuous symmetry spontaneously breaks. This is the Goldstone theorem. An example of this theorem can be shown with a Lagrangian (\mathcal{L}) [1]

$$\begin{aligned}\mathcal{L} = T - V &= \frac{1}{2} (\partial_\mu \phi)^2 - V(x), \\ V(x) &= \frac{1}{2} \mu^2 \phi^2 + \frac{1}{4} \lambda \phi^4,\end{aligned}\tag{1.22}$$

that describes scalar fields (ϕ), where T is the kinetic term, V is the potential term, and $\lambda > 0$. The Lagrangian is invariant under the transformation $\phi \rightarrow -\phi$. The μ^2 term can either be > 0 or < 0 , where μ is the mass term. Both cases affect the potential differently as shown in Fig. 1.4, where the potential on the left represent the $\mu^2 > 0$ case and the potential on the right represents the $\mu^2 < 0$ case. While the

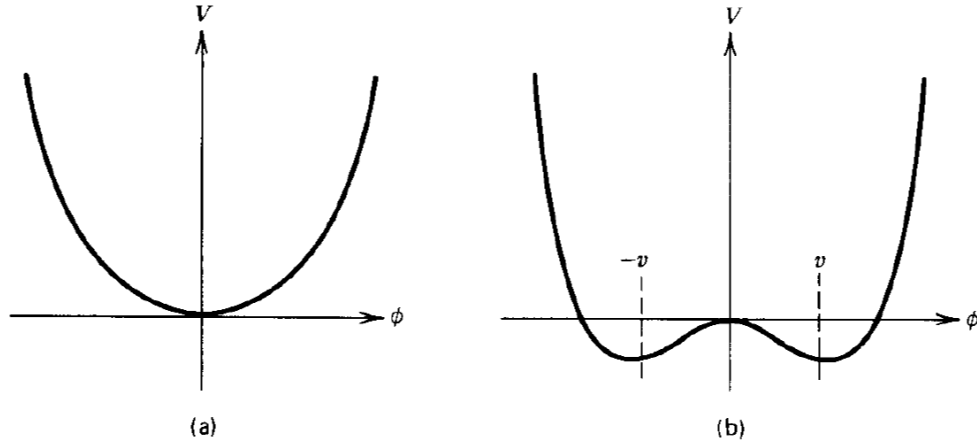


Figure 1.4 : The different potentials (V) based on the sign of μ^2 . The potential on the left represents the $\mu^2 > 0$ case and the potential on the right represents the $\mu^2 < 0$ case, where $\nu = \sqrt{\frac{-\mu^2}{\lambda}}$. This figure was taken from [1].

$\mu^2 > 0$ case has a minimum at $\phi = 0$, this does not correspond to an energy minimum (*i.e.*, ground state/vacuum). The $\mu^2 < 0$ case has minima at $\phi = \pm \sqrt{\frac{-\mu^2}{\lambda}}$ and both

are ground states. However, by selecting one of the minima, or ground states, one would break the symmetry even though V would remain symmetric. It should also be noted that a mass term < 0 is not physical.

To obtain a physical mass term, expand ϕ at $\sqrt{\frac{-\mu^2}{\lambda}}$ with a $\chi(x)$ field, which represents quantum fluctuations around the minimum, and gives

$$\phi(x) = \sqrt{\frac{-\mu^2}{\lambda}} + \chi(x). \quad (1.23)$$

Plugging the ϕ back into \mathcal{L} (Eq. 1.22) gives

$$\mathcal{L}' = \frac{1}{2}(\partial_\mu\chi)^2 - \lambda \left(\sqrt{\frac{-\mu^2}{\lambda}} \right)^2 \chi^2 - \lambda \sqrt{\frac{-\mu^2}{\lambda}} \chi^3 - \frac{1}{4}\lambda\chi^4 + \frac{1}{4}\frac{\mu^4}{\lambda}. \quad (1.24)$$

Now, the χ field has a physical mass term

$$m = \sqrt{-2\mu^2}, \quad (1.25)$$

which allows the χ^2 term to have the form

$$-\frac{1}{2}m^2\chi^2. \quad (1.26)$$

The higher-ordered χ terms represent self-interacting terms, like how gluons are able to self-interact.

By expanding around the minimum, a physical mass term was generated—this revealing of a physical mass term is spontaneous symmetry breaking. To rephrase and relate to the original Lagrangian, μ^2 is a broken symmetry phase that has mass, but for the mass to be physical, it is necessary to expand around the minimum (*i.e.*, undergo spontaneous symmetry breaking).

Building on the scalar field example, we can make ϕ a complex scalar field

$$\phi = (\phi_1 + i\phi_2) / \sqrt{2}. \quad (1.27)$$

The Lagrangian from Eq. 1.22 becomes [1]

$$\mathcal{L} = \frac{1}{2} (\partial_\mu \phi_1)^2 + \frac{1}{2} (\partial_\mu \phi_2)^2 - \frac{1}{2} \mu^2 (\phi_1^2 + \phi_2^2) - \frac{1}{4} \lambda (\phi_1^2 + \phi_2^2)^2, \quad (1.28)$$

which has a similar form and solutions as before (Eq. 1.22). The minima of interest are at

$$\phi_1^2 + \phi_2^2 = -\frac{\mu^2}{\lambda}, \quad (1.29)$$

a circle. Again, expand the ϕ around one of the minima, $(\phi_1, \phi_2) = (\sqrt{-\frac{\mu^2}{\lambda}}, 0)$, with $\chi(x)$ for the real component and $\xi(x)$ for the imaginary component. The complex scalar field then becomes

$$\phi(x) = \sqrt{\frac{1}{2}} \left(\sqrt{-\frac{\mu^2}{\lambda}} + \chi(x) + i\xi(x) \right). \quad (1.30)$$

Substituting in the expanded field into the Lagrangian (Eq. 1.28) results in

$$\mathcal{L}' = \frac{1}{2} (\partial_\mu \xi)^2 + \frac{1}{2} (\partial_\mu \chi)^2 + \mu^2 \chi^2 + \text{constant} + \text{quartic terms in } \chi \text{ and } \xi. \quad (1.31)$$

Again, a physical mass term pops out for the χ field. New in this Lagrangian is a ξ field with a kinetic term $(\frac{1}{2} (\partial_\mu \xi)^2)$, but no associated mass term. This is referred to as a massless scalar field, or a Goldstone mode/boson. The spontaneous symmetry breaking of the $SU(3)_A$ generates these Goldstone modes, too. The modes are π , η , and K . However, these mesons are not observed to be massless. Instead, the mesons are observed to have mass. The mass is a result of the light flavored quarks (*i.e.*, u , d , and s) being massive and explicitly breaking the $SU(3)_A$ symmetry. This is OK and the spontaneous breaking of the symmetry still functions as a viable model since the quark masses are relatively small, much like how a wheel with a small dent in it still rotates.

As noted in Sec. 1.1, the mass difference between the chiral partners is a result of a spontaneous breaking of the symmetry. Assuming that the interaction (potential)

between the chiral partners σ and π is similar to the potential in Eq. 1.28, the potential would take the form shown in Fig. 1.5 with the σ field on the x-axis and π field on the y-axis. The ball in the circular valley is able to rotate from one field into another.

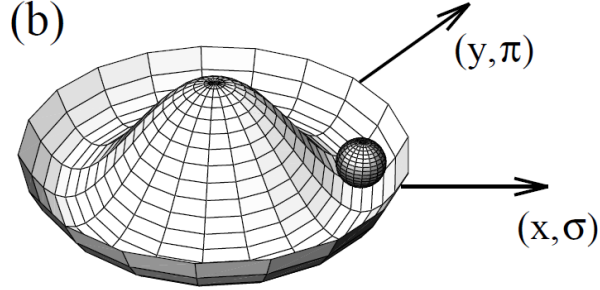


Figure 1.5 : A ball sitting in a potential that is rotationally symmetric. This figure was taken from [3].

This rotation is similar to the axial transformation performed in Sec. 1.1, where the axial transformation rotates one chiral partner into the other partner. The ball has spontaneously settled in a minima that corresponds to the previous example's minima at $(\phi_1, \phi_2) = (-\sqrt{\frac{\mu^2}{\lambda}}, 0)$ with the χ and ξ fields mapping to the σ and π fields. This position has been chosen because the σ field has the same characteristics as a quark-antiquark wave function $(\bar{\psi}\psi)$ and that is the same characteristic as the vacuum, or ground state, while the π does not possess the same characteristics as the vacuum. The expectation value of the quark-antiquark wave function $(\langle\bar{\psi}\psi\rangle)$ is also known as the quark condensate or chiral condensate. Similar to μ^2 , $\langle\bar{\psi}\psi\rangle$ becomes an order parameter of the symmetry breaking. This order parameter has a finite value because the σ field is some distance away from the center. It also means that the π field, which corresponds to the ξ field in our previous example, is massless. This explains the mass difference between the chiral partners, and when we also consider

the finite quark masses, it explains why the π mass is relatively low and not quite massless.

At high temperatures and/or densities, $\langle\bar{\psi}\psi\rangle$ is expected to vanish [3]. In our example potential, which looks like a sombrero, a vanishing $\langle\bar{\psi}\psi\rangle$ would result in the center of the potential to drop and turn the potential into a bowl-like shape. The ball sitting in the valley in Fig. 1.5 would roll into the minimum at the center and would signify the σ and π fields becoming degenerate. This example of spontaneous symmetry breaking between π and σ extends well for the chiral partners ρ and $a_1(1260)$, where their mass difference can be explained by the spontaneous breaking of the $SU(3)_A$ symmetry. If one was to change to a phase of QCD matter, where the temperature and/or density was higher, it would be interesting to see if the mass difference between the chiral partners disappears and the symmetry is restored. This is one of the reasons why people are interested in studying QCD under different conditions.

1.1.1 Phase Diagram

Enrico Fermi stated that matter in unusual conditions could be represented by a phase diagram [50]. Similar to the phase diagram for water, in which the phases for water (*i.e.*, gas, liquid, and solid) are mapped, the phase diagram for QCD matter allows for gas, plasma, and solid phases. These three phases are formally known as the Quark-Gluon Plasma (QGP), Hadron Gas, and Color Superconductor [51]. The Quark-Gluon Plasma is best described as a plasma with freely interacting quarks and gluons, the Hadron Gas phase is a medium of freely interacting hadrons (a bound state of quarks; mesons and baryons), the Color Superconductor phase is a medium of quark Cooper pairs. When QCD matter is in a state of local thermal equilibrium,

it can be described by an equation of state with the external variables temperature and baryonic chemical potential (μ_B) (*i.e.*, the change in free energy as a result of adding a baryon into the system with temperature (T) and volume (V) constant). The μ_B is related to the net baryon density (n_B) is the difference in number of baryons (N_B) and the number of anti-baryons ($N_{\bar{B}}$) per unit volume ($n_B = \frac{N_B - N_{\bar{B}}}{V}$) of the system. In a grand canonical ensemble, the quark chemical potential (μ_q) may be associated with μ_B as $\mu_q = \frac{1}{3}\mu_B$. It follows that the net quark density (n_q) is the difference in number of quarks (N_q) and the number of anti-quarks ($N_{\bar{q}}$) per unit volume ($n_q = \frac{N_q - N_{\bar{q}}}{V}$), and then $3n_B = n_q$. The relationship between quark and baryon numbers enables mapping baryon dominated and quark dominated phases on the same plane. The phases of QCD matter are typically shown on a $T - \mu_B$ plane. The current understanding of the QCD phase diagram is shown in Fig. 1.6 [4].

In Fig. 1.6, the label *Nuclear Matter* is matter at the room-temperature environment. Along the right side of the baryon chemical potential axis, this region represents the conditions in a neutron star, which has a high neutron density at low temperatures; along the left side, this region represents a Hadron Gas phase. The upper left corner represents the early universe (a few microseconds after the Big Bang [52]) where it is hot (order of 0.3 GeV [53]) and there exists an equal balance of baryons and anti-baryons ($\mu_B \sim 0$). Heavy ion (*e.g.*, Au, Pb, or U) collisions are capable of generating QCD matter that starts in the Quark-Gluon Plasma phase (represented as an explosion symbol in the plot) and then, as the hot, dense medium cools down, it begins to traverse the phase diagram into the hadron gas phase (the transition is represented by the colored arrow in the plot).

Figure 1.7 illustrates the evolution of a heavy ion collision through different stages of the collision's life. The depicted collision evolution is broken down into 5 stages

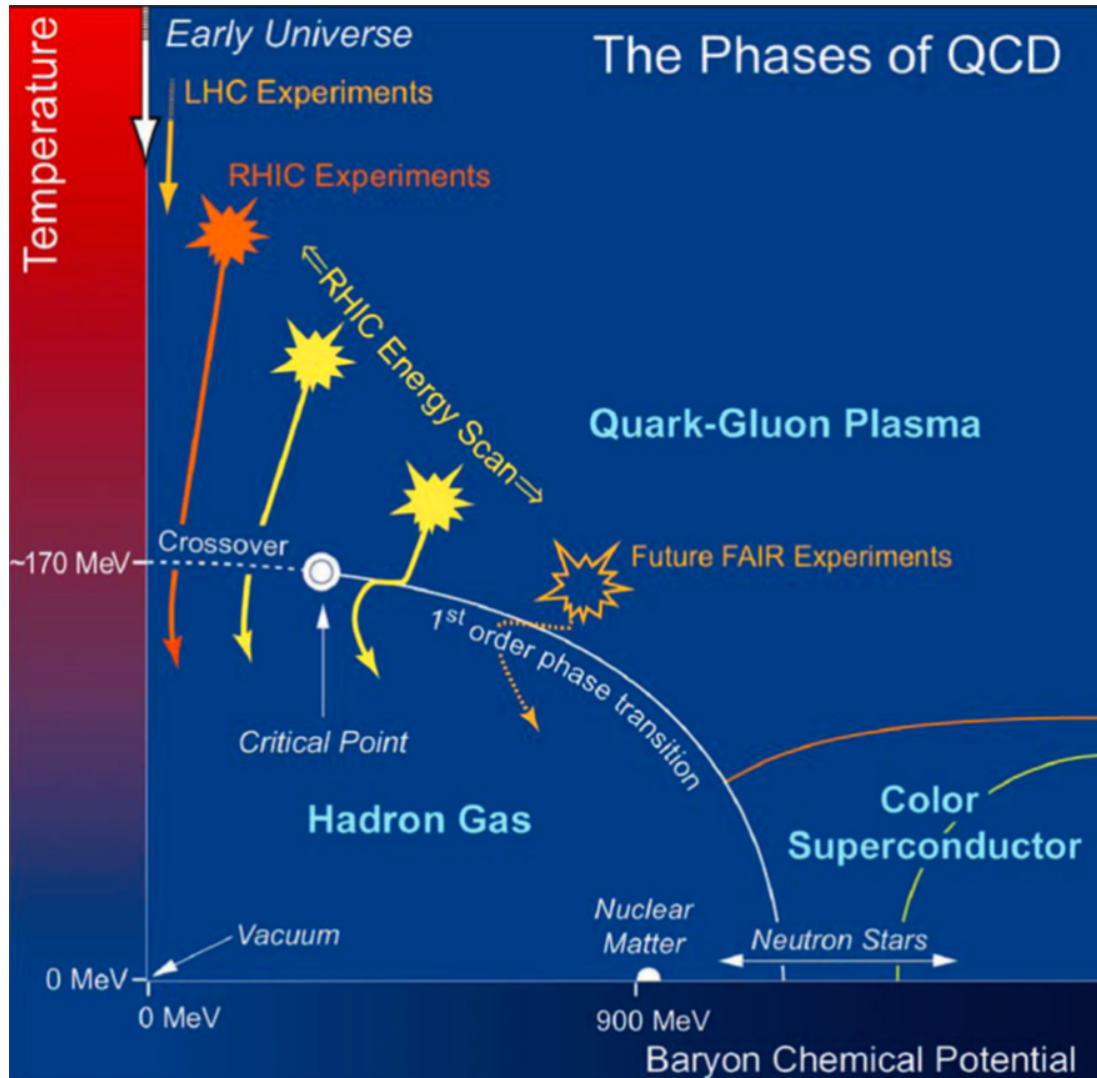


Figure 1.6 : A conjectured phase diagram for QCD matter. This figure was taken from [4].

(i.e., (1)Before colliding, (2)Pre-equilibrium, (3)Expansion, (4)Hadronization, and (5)Freeze-out). (1) Before the collision, the ions are traveling at relativistic speeds toward one another. At relativistic speeds, there is Lorentz contraction, which is why the spherical ions resemble pancakes in Fig. 1.7. (2) At the start of the collision, quarks and gluons that make up the nucleons of the colliding ions will begin to

scatter off each other. The collision system begins to rapidly increase in pressure and temperature. This leads to a hot, dense collection of quarks and gluons with a low μ_B and high temperature. (3) The quarks and gluons thermally equilibrate and form a state of matter (*i.e.*, medium) described by freely interacting quarks and gluons, or a QGP. The collision system will undergo collective expansion causing a decrease in temperature. (4) Once cold enough, the quarks and gluons will coalesce to form hadrons. This process is called hadronization and the collision system is now best described by thermally equilibrated hadrons. A state of matter called hadron gas. (5) The expansion continues and cools to the temperature where hadrons no longer inelastically collide, and this is known as chemical freeze-out. Still expanding and cooling, the collision continues until the hadrons no longer maintain thermal equilibrium, and this is referred to as kinetic freeze-out. At this point, the remaining hadrons will (hopefully) be detected by equipment setup around the collision. The collision process during thermal equilibrium is called a fireball as it can be described by relativistic hydrodynamics [54].

1.1.2 Quark-Gluon Plasma

The Quark-Gluon Plasma is a phase of QCD matter consisting of freely interacting quarks and gluons, where enough energy density is present to negate the bounds between quarks and gluons and make them asymptotically free [55, 56]. When the baryon chemical potential is close to zero and temperatures are high ($T \sim 0.3$ GeV [53]), the QGP resembles conditions similar to the Universe microseconds after the Big Bang as illustrated in Fig. 1.8 [6]. These temperatures and baryon chemical potentials are reachable by the collision of heavy ions near the speed of light, where a fireball is created with lower μ_B and higher T as the center-of-mass collision energy

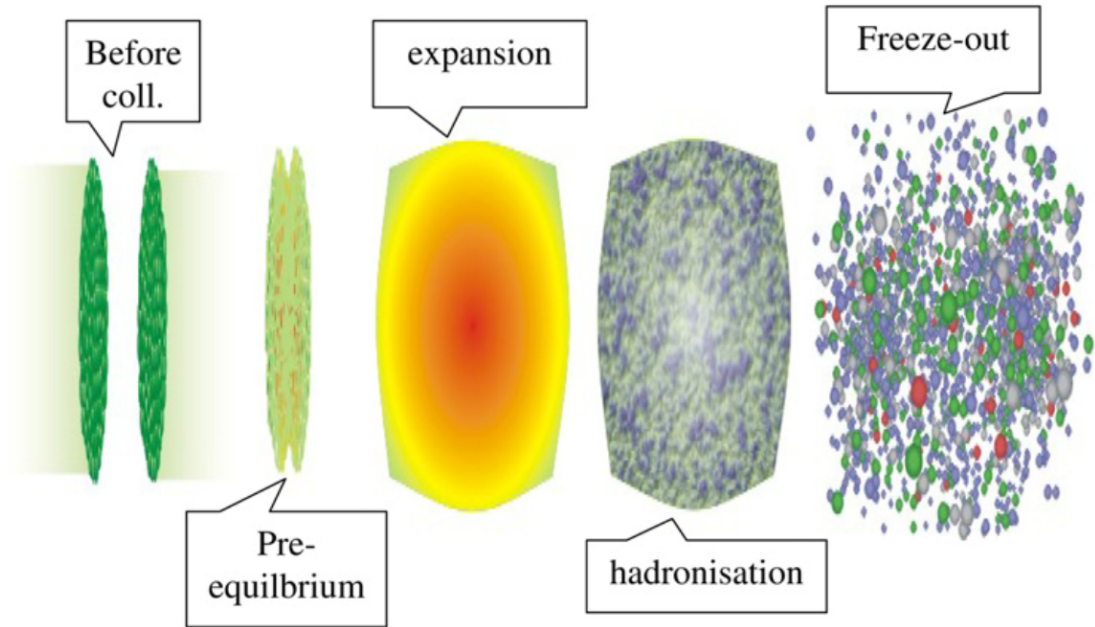


Figure 1.7 : The evolution of a heavy ion collision. This figure was taken from [5].

is increased [57], as indicated by the explosion symbols in Fig. 1.6.

1.2 Evidence of the Quark-Gluon Plasma

Heavy ion collision experiments have provided evidence for the formation of the QGP [9]. Detectors for these experiments are either situated around a target at the terminus of a beam line branching off an accelerator complex or along an interaction point at a circular collider. One of these circular colliders is the Relativistic Heavy Ion Collider (RHIC) at Brookhaven National Laboratory, Upton, NY, which houses the detector known as the Solenoidal Tracker at RHIC (STAR). At the RHIC, $A + A$ collisions are provided with collision energies between a center-of-mass energy per nucleon-nucleon pair ($\sqrt{s_{NN}} = 5$ and $\sqrt{s_{NN}} = 200$ GeV). This thesis presents data that has been produced at STAR. Previous key STAR measurements [9] that support the formation

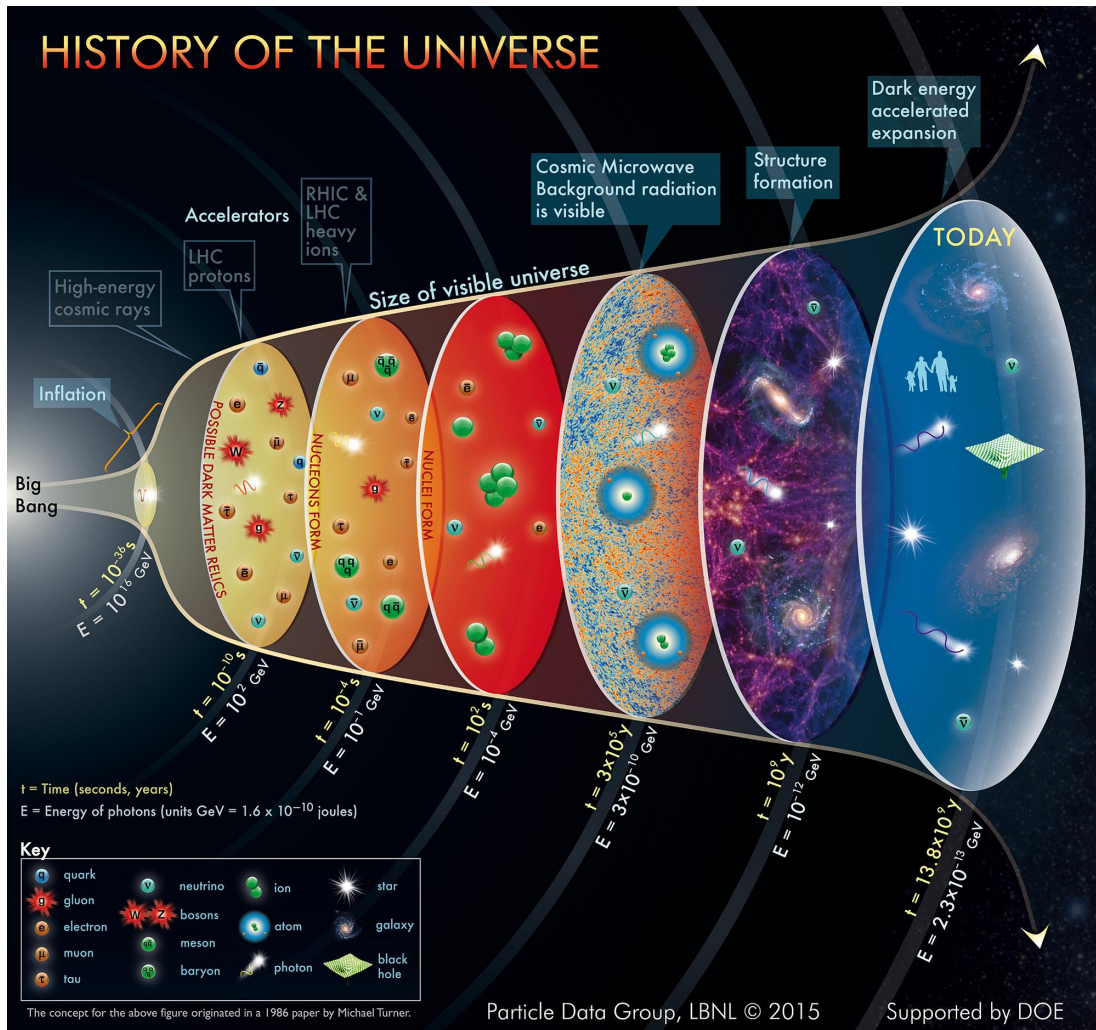


Figure 1.8 : History of the Universe from the Big Bang to present day. This figure was taken from [6].

of the QGP include jet suppression, quark scaling of elliptic flow, and freeze-out temperatures consistent with theoretical calculations that predict the phase transition temperature. The measurements performed by STAR follow the coordinate system defined in Fig. 1.9. The z -axis is along the beam line, and the x - and y -axes define the plane transverse to the z -axis. The polar angle (θ) is the angle between the z -axis and momentum (\vec{p}) in \hat{z} (p_z), and the azimuthal angle (ϕ) is the angle between the

x -axis and the momentum in the transverse plane (*i.e.*, transverse momentum (p_T)).

The rapidity,

$$y = \frac{1}{2} \ln \left[\frac{E + p_z}{E - p_z} \right], \quad (1.32)$$

where E is the energy of the particle, is another variable used to describe the kinematics of a particle. For convenience, the variable pseudo-rapidity ($\eta = -\ln[\tan(\theta)/(2)]$) is defined as the angle of particle emission with respect to the beam axis and is the rapidity (y) in the limit where mass (m) is ignored ($p \gg m$). The pseudo-rapidity is helpful when dealing with multiple particle species or particles that have not been identified (*i.e.*, mass is unknown). The transverse distance between the centers of two colliding nuclei is the impact parameter (b) and is a measure of centrality. Centrality is the amount of overlap between the colliding ions and is scaled from 0-100%, where the lowest percentage (*i.e.*, smallest b) is the most central collision. A 0% centrality corresponds to the scenario where the ions collide head-on and there is a complete overlap between the colliding transverse surfaces. A 100% centrality corresponds to the scenario where the ions pass-by each other without overlapping. Centrality can be related to the number of particles created in the collision, where more central collisions lead to more particles [58].

Jet suppression [59] refers to the observation that the jets produced in heavy ion collisions lose energy as they traverse the QGP. One way to observe the suppression is the comparison of di-hadron azimuthal correlations ($\Delta\phi$) between different collision systems, where $\Delta\phi$ is the difference between the azimuthal angles of the high- p_T triggered hadron and another high- p_T hadron within the collision. Trigger hadrons are hadrons that the detector recognized as having a high- p_T and led to the collision information being saved. The correlations in central gold-on-gold (Au+Au) collisions, deuteron-on-gold ($d+Au$) collisions, and proton-on-proton ($p+p$) collisions are shown

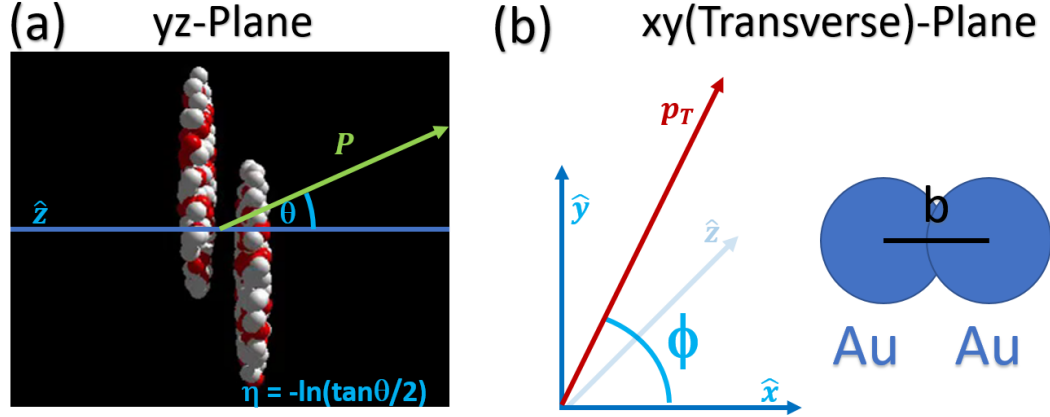


Figure 1.9 : The coordinate system used for making measurements at the STAR experiment. (a) Two heavy ions the moment before they collide. The momentum vector (P) is used to illustrate the coordinates with respect to the z -axis. (b) The transverse momentum vector is used to illustrate the coordinates with respect to the transverse plane. Also shown is a transverse view of two gold atoms colliding. The transverse distance between the centers of the nuclei is known as the impact parameter (b).

in Fig. 1.10 [7]. Two peaks at $\Delta\phi \approx 0$ (near-side) and $\Delta\phi \approx \pi$ (away-side) in $d + Au$ and $p + p$ collisions correspond to dijet production, where the near side peak is the trigger hadron being paired with other high- p_T hadrons from the same jet and the away-side peak is from the trigger hadron being paired with high- p_T hadrons from the other jet (dijets are produced back-to-back). However, central Au+Au collisions exhibit one peak at the near side. The missing away-side peak is an observation of jet suppression. The disappearance of the peak is explained as the triggered hadron belonging to a jet that has been emitted near the edge of the QGP, while its partner must traverse across the QGP to be detected. The partner jet loses energy during the traverse because the medium is dense with quarks and gluons and those quarks and gluons interact strongly with the jet. These interactions cause the jet to fragment

and radiate away energy to the extent that the jet becomes indistinguishable from the medium. Hence, the suppression of the jet is evidence for a strongly interacting medium.

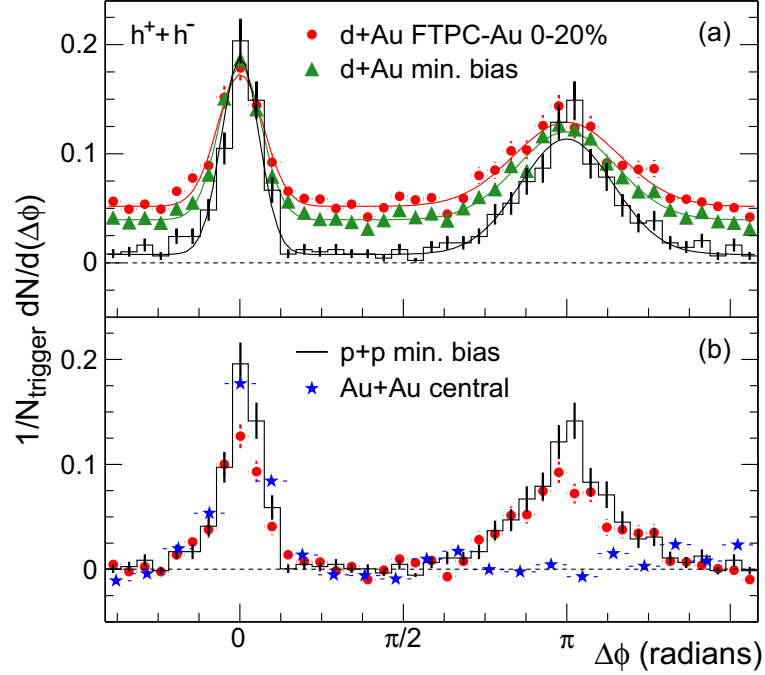


Figure 1.10 : The dihadron azimuthal distributions of h^+h^- for $p + p$ collisions (bar graph), minimum bias $d+\text{Au}$ collisions (red points), $d+\text{Au}$ collisions of the top 20% centrality (green triangles), and central (0-5%) $\text{Au}+\text{Au}$ collisions (blue stars). This figure was taken from [7].

Quark scaling of elliptic flow refers to the scenario where the elliptic flow (v_2) of hadrons, when divided by the number of constituent quarks (n_q), overlap with one another. Quark scaling of v_2 is indicative of the collective expansion of the medium at the quark level as opposed to the hadron level. Elliptic flow is the second component of the Fourier expansion of the particle azimuthal distribution ($\frac{dN}{d\Delta\phi} \propto 1 + \sum_n 2v_n \cos(n\Delta\phi)$ or $v_2 = \langle \cos(n\Delta\phi) \rangle$). The v_2 and v_2/n_q for the hadrons π , K_S^0 , p , and Λ are shown in Fig. 1.11 [8]. Each of the hadrons' elliptic flow overlap

after normalizing for the number of constituent quarks, except for π . For π , one explanation for the deviation of v_2/n_q from the other hadron distributions is that these π are not only direct products of the medium, but from secondary π (*i.e.*, decay products) too. Secondary π , which originate from hadrons simulated to follow the number of constituent quark scaling, exhibit a v_2/n_q similar to the measured values [8]. The secondary π simulation agreement with data and the other hadrons following quark scaling suggest a phase of QCD matter consisting of partons (*i.e.*, quarks and gluons), a QGP, or at least that partonic degrees of freedom matter exists.

Chemical freeze-out temperatures have been determined from a statistical model, which is based on the grand canonical ensemble description [60], fit to the hadron yield ratios. The fit of the hadron yield ratios are shown in Fig. 1.12 [9]. The resulting temperature and baryon chemical potential are 163 ± 4 MeV and 24 ± 4 MeV, respectively [9]. They have been found to be consistent with lattice QCD calculations [61] and are used as evidence of a phase transition between the QGP and hadron gas phases. Lattice QCD is the use of lattice gauge theory [62, 63, 64, 65, 66] to calculate properties of QCD matter in the nonperturbative regime on a set (lattice) of space-time points.

1.3 Beam Energy Scan Program

The Beam Energy Scan Program at RHIC set out to scan the QCD phase diagram by colliding Au with Au at a large range of collision energies. By varying the collision energy, the initial temperature and baryon chemical potential are changed while maintaining the collision species. In the phase diagram shown in Fig. 1.6, the conjectured region of the mapping by the Beam Energy Scan Program is illustrated with the yellow symbols and the label, *RHIC Energy Scan*. By mapping out the

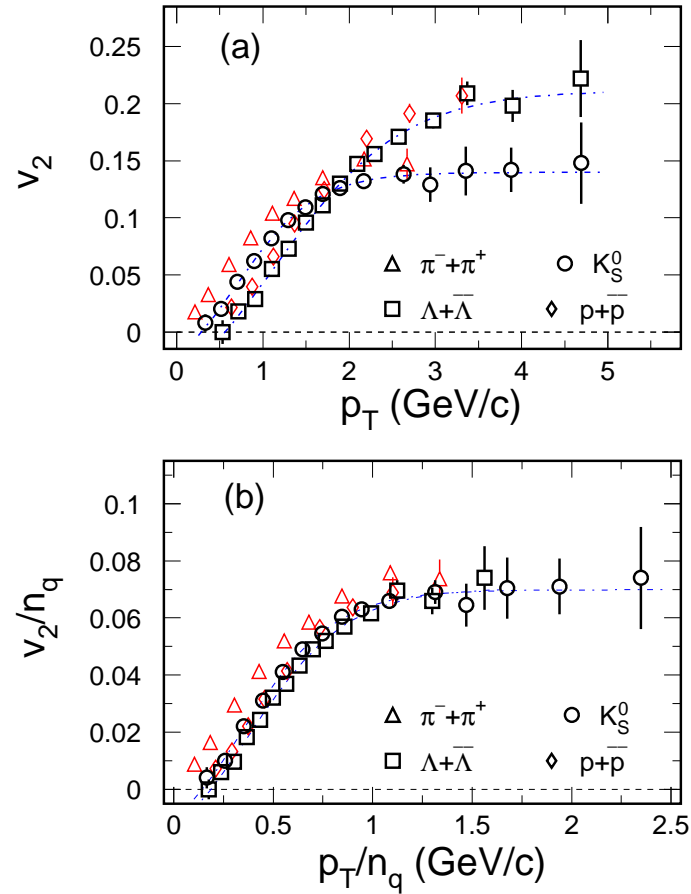


Figure 1.11 : (a) The elliptic flow v_2 for π , K_S^0 , p , and Λ as a function of p_T . (b) v_2 normalized by the number of quarks (n_q) for π , K_S^0 , p , and Λ as a function of p_T/n_q . This figure was taken from [8].

phase diagram, the program set out to: (1) confirm and build upon the evidence of the aforementioned QGP and the early signs of the QGP in measurements from the Alternating Gradient Synchrotron and Super Proton Synchrotron, (2) search for evidence of a first-order phase transition, and (3) search for a critical point in the QCD phase diagram [4]. A key tool used to study the properties of the collisions are electromagnetic probes, which are particles that interact via the electromagnetic

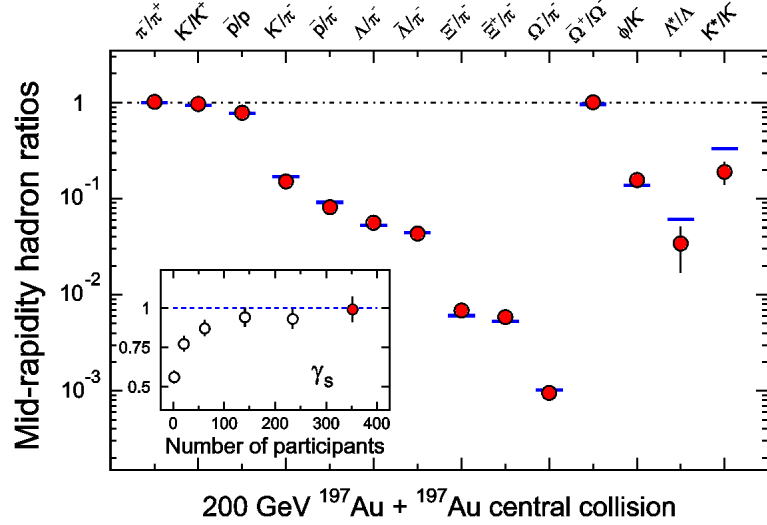


Figure 1.12 : The ratio of hadron yields in Au+Au collisions at $\sqrt{s_{NN}} = 200$ GeV from STAR. The horizontal bars represent the statistical model fit to the ratios of hadron yields. This figure was taken from [9].

force and not the strong force.

1.4 Electromagnetic Probes

1.4.1 Introduction

Electromagnetic probes are particles that interact electromagnetically and their properties can be used to study the collision. Photons γ and virtual photons γ^* (where γ^* decay into lepton pairs l^+l^- and $l = e, \mu$) are produced throughout the evolution of a collision. These products do not interact via the strong force, but rather, interact electromagnetically. Hence, the particles are able to traverse the strongly interacting medium with minimal final state effects as the electromagnetic coupling constant (α_{em}) is much less than the strong coupling constant (α_s). Or in other words, these particles are able to carry information from the time of their genesis to

the detector, which provides valuable insight into the conditions during various stages of the collision. The kinematic properties of the probes can be used to distinguish at which stage of the collision the probe was produced. Hence, with the minimal final state effects and the ability to discriminate which stage of the collision the probes originated, the probes are excellent tools to study the medium.

1.4.2 Uses

By separating the electromagnetic probes based on their kinematic properties, one can differentiate and study the various stages of the collision. For photons, the kinematic variable of choice is their transverse momentum, or transverse energy. The transverse momentum spectrum can be chronologically divided where photons from the earliest stages of the collision dominate the higher momentum regions and photons from the later stages dominate the lower momentum end of the spectrum, as illustrated in Fig. 1.13 [10]. In Fig. 1.13, the earliest dominant contributions are prompt photons from hard scatterings (green line), then the photons from jet interactions in the medium (purple line), followed by contributions from the medium before thermal equilibrium is established (gray line), then photons from the QGP (red line), and finally, photons from the Hadron Gas phase (blue line). Not shown are the photons from the hadron decays, which occur much later in the collision lifetime.

For γ^* ($\gamma^* \rightarrow l^+l^-$), there is an additional kinematic property that real photons do not have and that is mass. The invariant mass of l^+l^- (M_{ll}) can be used to study the various stages of each collision, where earlier times dominate the higher invariant masses, but also contribute to lower invariant masses. The stages are illustrated as the e^+e^- invariant mass in Fig. 1.14. In Fig. 1.14, the High-Mass Region (HMR, $M_{ll} \gtrsim M_{J/\psi}$) corresponds to < 1 fm/c [11] after the start of the collision and is dominated

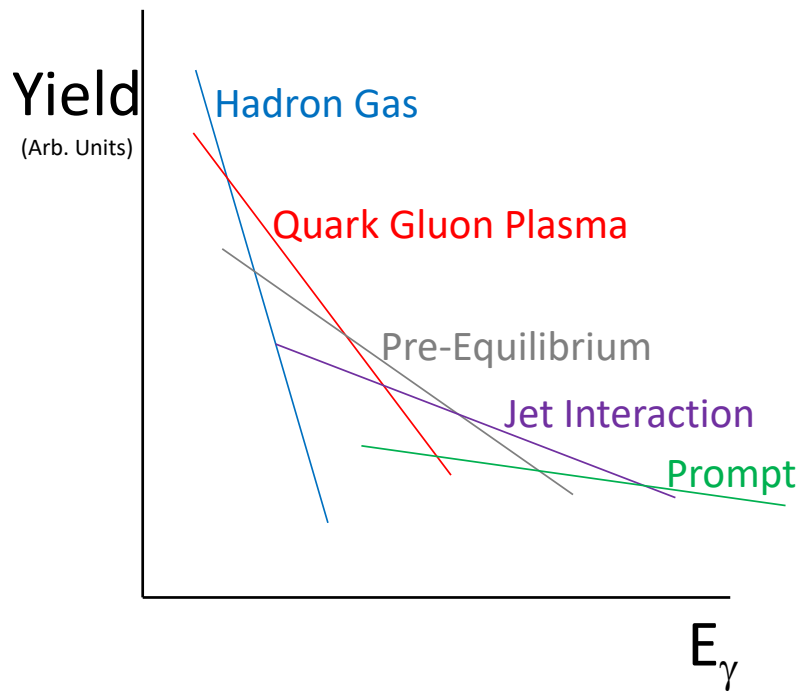


Figure 1.13 : The relative yields to the photon transverse momentum/energy spectrum from different stages of the collision. This figure was created based on [10].

by contributions from the Ψ -family and Drell-Yan, the Intermediate-Mass Region (IMR, $M_\phi \lesssim M_{ll} \lesssim M_{J/\Psi}$) corresponds to $\sim 1 - 10$ fm/c [11] and is dominated by contributions from open-heavy flavor decays, and the Low-Mass Region (LMR, $M_{ll} \lesssim M_\phi$) corresponds to the latest stages of the collision at ~ 10 fm/c [11] and is dominated by meson decays.

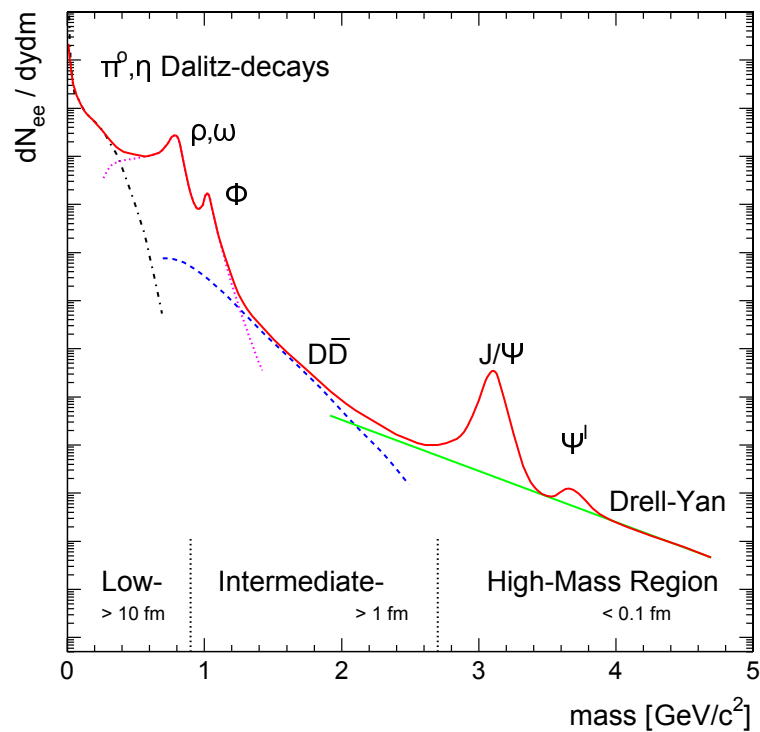


Figure 1.14 : The chronological divisions of the e^+e^- invariant mass spectrum, where x fm/c represents the typical time ($c = 1$) after the start of the collision. This figure was taken from [11].

1.4.3 Popular Topics

Various physics topics may be studied by selecting electromagnetic probes based on their kinematic properties. Popular topics include the effective temperature (T_{Eff}) of the medium, the collective expansion of the medium (size and momentum anisotropy—*e.g.*, v_2), the suppression of hadronic production by the medium, and the modification of vector mesons in the medium and the vector meson modification's possible link to chiral symmetry restoration. This will be further discussed in Ch. 2.

To study T_{Eff} of the medium with photons, an exponential fit to the photon yield as a function of energy can be used [10]. In order to do this, the photon yield must only contain photons thermally produced by the medium. Initially, all photons are measured and contribute to the yield. Hence, non-thermal photon contributions need to be removed, and non-thermal contributions are primarily the prompt photons from hard scatterings (very early in the collision) and the photons from hadron decays (late after the collision). Prompt photons come from quark gluon Compton scattering ($qg \rightarrow \gamma q$), quark anti-quark annihilation ($q\bar{q} \rightarrow \gamma g$), and quark fragmentation (*e.g.*, $qq \rightarrow qq\gamma$) as illustrated in Fig. 1.15. The prompt photon energy yield as a function of energy is approximated by theoretical calculations and is subtracted from the total yield. Since these mechanisms are also found in $p + p$ collisions, the calculations are typically Next-to-Leading Order (NLO) perturbative QCD prompt photon cross-sections for $p + p$ collisions, which have been scaled up by the number of nucleon collisions modeled to occur in the ion-on-ion ($A + A$) collision system [10]. The calculations account for effects such as nuclear shadowing, energy loss, and iso-spin conservation. Photons from hadron decays are predominately from π^0 , then η , and to a lesser extent ω , η' , and ϕ . One method in removing hadron decayed photons is by determining if there is an invariant mass after reconstructing a pair of photons

together, and if there is a mass, their spectrum is subtracted from the total photon spectrum, like the prompt photon contributions. Another technique used to identify photons from hadron decay is the measurement of virtual photons via l^-l^+ pairs. By selecting the transverse momentum of the l^-l^+ pair (p_T^ll) to be much greater than the invariant mass of the pair ($p_T^ll \gg M_{ll}$), the virtual photons are effectively real photons. This phenomenon is called internal conversion, where the source of real photons are also the source of low-mass virtual photons, and is being studied by both STAR [67] and PHENIX [68].

With the prompt and decay photons subtracted from the spectrum, all that should be left in the spectrum are photon contributions from the medium. Jets in the medium produce photons via the quenching of the partonic jets, in which the parton may undergo quark-gluon Compton scattering, quark-antiquark scattering, or bremsstrahlung within the medium to produce photons. The QGP contribution to the spectrum comes from quark-gluon Compton scattering and quark-antiquark annihilation in the QGP. The hadron gas contribution is predominately from $\pi\rho$ interactions, but there are contributions from other hadrons (*e.g.*, $\omega \rightarrow \gamma\pi$ [69, 70]), but the leading order contribution is from $\pi\rho$ interactions—due to the Hadron Gas temperature being on the same order as the π mass.[10]. Traditionally, an exponential ($e^{-E_\gamma/T_{Eff}}$) fit is made to the spectrum to derive the temperature. Because photons are thermally produced over the entire evolution of the collision, the temperature is not the initial temperature at a specific time, but rather an effective temperature of the medium. Note that theoretical models and additional kinematic measurements, such as momentum anisotropy and system size, are necessary to give a more precise temperature and make other observations of the medium [71].

Like photons, l^-l^+ pairs may be used to study a variety of aspects of the collision.

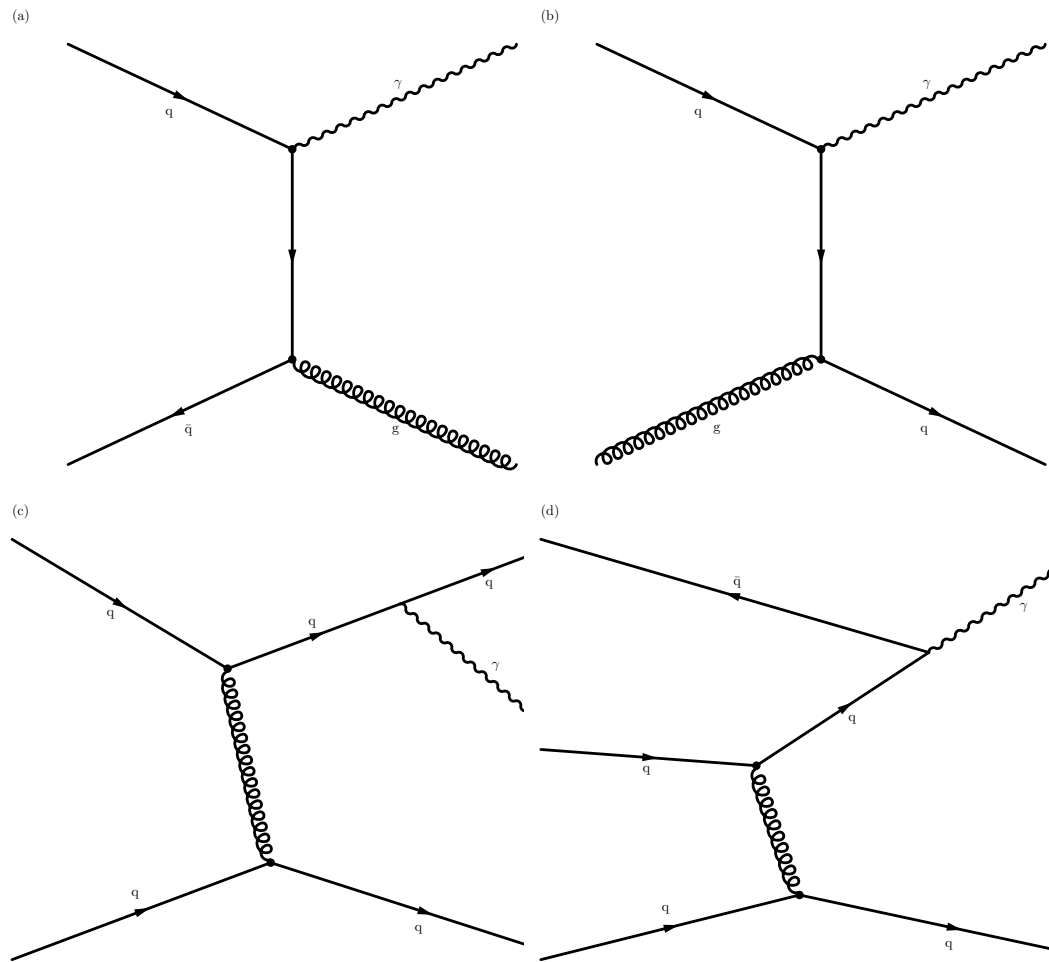


Figure 1.15 : Sources of prompt photons: (a) quark anti-quark annihilation (b) quark gluon Compton scattering, and (c + d) quark fragmentation.

The suppression of hadron production, such as the Ψ family (J/Ψ , $\Psi(2S)$), is studied through the reconstruction of their l^-l^+ daughters (*i.e.*, decay products), as these daughters are able to traverse the medium while carrying information about their parent (*i.e.*, J/Ψ , $\Psi(2S)$) at the time of their genesis. As shown in Fig. 1.14, the Ψ family is produced in the earliest stages of the collision of ions, where the energy density is high enough to generate more massive hadrons such as J/Ψ , and their l^-l^+ daughters will carry information about the QGP. As the QGP is a plasma of freely

interacting quarks and gluons, J/Ψ and other $c\bar{c}$ mesons in the QGP are thought to be created, melted, and recreated. Theoretically in the hot, dense medium, the $c\bar{c}$ has a bond that can be easily broken. Once broken, the partner quarks can easily be screened from one another by a color field from neighboring quarks and gluons [72]. This is akin to Debye screening, but with the strong force instead of the electromagnetic force. To evaluate the amount of suppression for J/Ψ , the distribution of J/Ψ as a function of p_T (*i.e.*, transverse momentum spectrum) from $A + A$ collisions is compared to a reference transverse momentum spectrum that is expected to have no medium effects. The reference spectrum is taken to be the $p + p$ transverse momentum distribution of J/Ψ that has been scaled by the number of nucleon-on-nucleon collisions (N_{coll}) in a $A + A$ collision, as if an $A + A$ collision is a collection of $p + p$ collisions. The comparison of the spectra is referred to as the nuclear modification factor (R_{AA}),

$$R_{AA} = \frac{dN/dp_T^{AA}}{N_{coll}dN/dp_T^{pp}}, \quad (1.33)$$

where dN/dp_T^{AA} is the transverse momentum spectrum from $A + A$ collisions with N being the number of particles in a given p_T bin and dN/dp_T^{pp} is the transverse momentum spectrum from $p + p$ collisions. In Eq. 1.33, an $R_{AA} < 1$ is suppression and > 1 is enhancement. The R_{AA} measurement (of the electromagnetic production from the earliest stages of the collision, such as prompt photons from jets) is used to verify that the electromagnetic probes traverse the medium with minimal final state effects. The production from prompt photons have been shown to have a $R_{AA} \sim 1$ [73]. Hence, electromagnetic probes do traverse the medium with minimal affects on their final state, and the suppression or enhancement (*i.e.*, R_{AA}) measured for J/Ψ would be related to the J/Ψ itself and not the decay products of J/Ψ .

In the IMR of the l^-l^+ invariant mass spectrum, the contributions are dominated

by open heavy flavor decays (*e.g.*, $c\bar{c} \rightarrow D^0\bar{D}^0 \rightarrow e^+K^-\nu_e e^-K^+\bar{\nu}_e$), Drell-Yan contributions ($q + \bar{q} \rightarrow e^+e^-$), and the QGP ($q\bar{q} \rightarrow \gamma^* \rightarrow e^+e^-$). One topic of interest in this IMR is the temperature of the QGP. By removing contributions from the open heavy flavor and Drell-Yan, the remaining invariant mass spectrum would have originated from the QGP. Then to measure the effective temperature, the invariant mass spectrum is fitted with an exponential ($A \cdot e^{M_{ee}/T_{Eff}}$). Like photons, the lepton pairs are produced throughout the evolution of the system and T_{Eff} is an integral of the collision temperatures. However, unlike thermal photons, the invariant mass spectrum does not change due to radial flow, and hence, no blue shift and a more ideal T_{Eff} measurement [74]. If statistics or uncertainty on the contributions in this region are insufficient to remove the contributions, studying the effective temperature, or inverse slope, could also be illustrative of the properties of the medium. The effective temperature has been studied by the CERN experiment NA60 with $\mu^+\mu^-$ from In+In collisions at $\sqrt{s_{NN}} = 17.3$ GeV [16].

In the LMR of the l^-l^+ invariant mass spectrum, contributions are primarily from the decay of light flavored mesons (*e.g.*, π^0 , η , ω , and ρ). Light flavored mesons are of interest because they are made up of light flavored constituent quarks and the mass of a light quark is primarily generated by the spontaneous breaking of chiral symmetry, as shown in Fig. 1.16 [12]. However, most light mesons are not formed until later in the collision when chiral symmetry has already been broken. On the other hand, the ρ has a short lifetime, ~ 1.3 fm/c, and may decay at a time when chiral symmetry is at least partially restored. The ρ decaying during this temporal period is an excellent opportunity because the ρ and its chiral axial-vector partner, $a_1(1260)$, are candidates for exhibiting chiral symmetry breaking, which is demonstrated in Sec. 1.1. By measuring and studying the ρ , one may gain insight into chiral symmetry

restoration, or at the very least, information about the hot, dense matter.

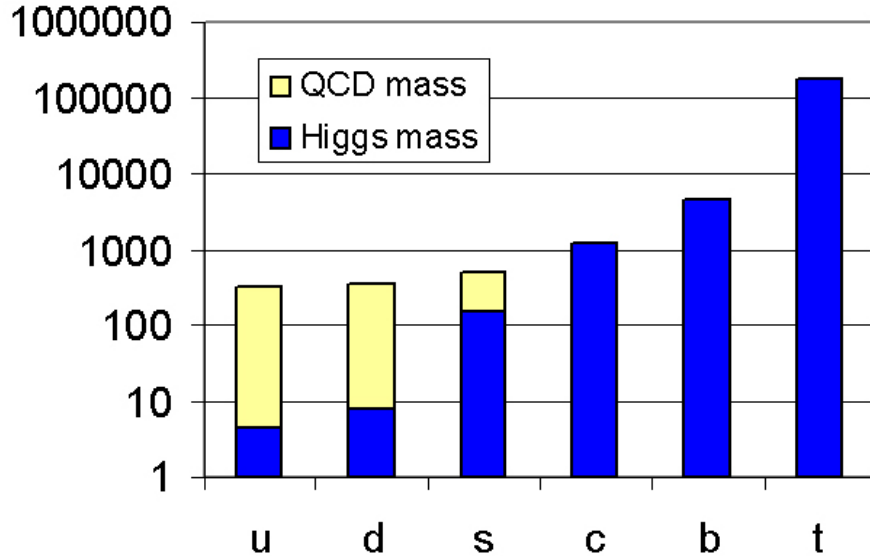


Figure 1.16 : The estimated masses for the up, down, charm, strange, truth, and beauty quarks and the relative contribution to each mass from different mechanisms. The yellow bar represents the contribution to the mass from the breaking of chiral symmetry and the blue bar represents the contributions to the mass from the breaking of electroweak symmetry (Higgs mechanism). This figure was taken from [12].

The mass difference between these chiral partners and other chiral partners are an excellent example of spontaneous chiral symmetry breaking. The $a_1(1260)$ does not decay into products that are easily reconstructed in the heavy-ion collisions environment (there has not been an a_1 measurement made by a heavy-ion experiment with $A + A$ collisions at $\sqrt{s_{NN}} > 20$ GeV, yet). The a_1 has a short-lifetime, is a wide resonance, and decays into products that interact via the strong force, which make measuring the a_1 experimentally challenging [75]. However, the ρ has a decay channel to e^+e^- with a branching ratio of 0.00472% [45]. While it is not frequent, it is possible to measure. The reason for selecting the e^+e^- channel rather than the

$\pi\pi$ channel, which has a branching ratio of $> 99\%$, is that the electrons are able to traverse the hot, dense medium with minimal effects and retain information about their parent, or in this case, the ρ at the time of the decay while the π s are modified by the medium.

For my thesis, I have set out to measure the invariant mass spectrum of e^+e^- pairs in the collision of $Au + Au$ at $\sqrt{s_{NN}} = 27$ GeV. The goal of the measurement is to extract the e^+e^- pairs that have been produced by the ρ and QGP. The ρ is especially interesting because when it decays, the medium is still hot and dense. Recall our sombrero example, increasing the temperature and density of the medium may lead to the chiral symmetry being restored, at least partially. While it would be very challenging to measure the a_1 and search for degeneracy, comparing the e^+e^- pairs to theoretical calculations may be an alternative approach to say something about the restoration of chiral symmetry, or at least, describe the behavior of the ρ in a hot, dense medium. In the next chapter, I will discuss the different models pertaining to the ρ and QGP production of e^+e^- pairs.

Chapter 2

Theoretical Models

2.1 Introduction

As previously mentioned in Sec. 1.4.1, electrons traverse the strongly interacting collision system with minimal effect on the final state of the electrons and retain kinematic information about their source(s). In the low mass region of the e^+e^- invariant mass spectrum, the invariant mass spectrum from ρ and the QGP are of particular interest. Theoretical models are used to predict the phenomena that occur in this low mass region of the e^+e^- invariant mass spectrum for the ρ and QGP contributions to the e^+e^- invariant mass spectrum (*e.g.*, mass dropping versus broadening of the ρ spectral function). These theoretical models include those models by Rho-Brown [76, 77], Rapp *et al.* [78, 79, 80, 81, 35], and Parton-Hadron-String Dynamics [82, 83, 84, 85], which describe a shift in the ρ mass, broadening of the ρ spectral function & QGP contributions, and broadening of the ρ spectral function & QGP contributions, respectively, as discussed in further detail in the following sections (Sec. 2.2, 2.3, and 2.4).

2.2 Rho-Brown

The density-induced scaling of the ρ mass results in a shift of its pole (*i.e.*, ground state) mass toward 0 as density increases and was first hypothesized by G.E. Brown and M. Rho [76, 77]. The density-induced scaling of the ρ mass is performed by

introducing a medium-dependent scalar field to break the scale invariance of the Skyrme Lagrangian [86] (\mathcal{L}_0)— an effective chiral $SU(2) \times SU(2)$ Lagrangian. An effective chiral Lagrangian should describe the kinematics of QCD in the low-energy limit, and in particular, it should exhibit similar properties as QCD [49]. The Skyrme Lagrangian with chiral fields (U) is

$$\mathcal{L}_0 = \frac{f_\pi^2}{4} \text{Tr} (\partial_\mu U \partial^\mu U^\dagger) + \frac{\eta^2}{4} \text{Tr} [U^\dagger \partial_\mu U, U^\dagger \partial_\nu U]^2 + c \text{Tr} (MU + H.c.), \quad (2.1)$$

where the chiral field (U) is defined as $e^{i\pi/f_\pi}$ with $\pi = \vec{\pi} \cdot \vec{\tau}$, $\vec{\pi}$ being a pion field, τ being the Pauli matrices, and the f_π is the pion decay constant. The η term is a coefficient that is directly related to the axial-vector coupling constant (g_A), c is a constant, M is the quark mass matrix and explicitly breaks the symmetry, and $H.c.$ is the hermitian conjugate. However, the Skyrme Lagrangian does not follow the scaling behavior of the QCD Lagrangian (Eq. 1.1 in Sec. 1.1)—the Skyrme Lagrangian does not contain a trace anomaly. To incorporate in the Skyrme Lagrangian a behavior similar to that of a trace anomaly, Ellis [87] introduced a scalar glueball field (χ) into the Skyrme Lagrangian and transformed Eq. 2.1 into

$$\begin{aligned} \mathcal{L} = & \frac{f_\pi^2}{4} \left(\frac{\chi}{\chi_0} \right)^2 \text{Tr} (\partial_\mu U \partial^\mu U^\dagger) + \frac{\eta^2}{4} \text{Tr} [U^\dagger \partial_\mu U, U^\dagger \partial_\nu U]^2 \\ & + c \left(\frac{\chi}{\chi_0} \right)^3 \text{Tr} (MU + H.c.) + \frac{1}{2} \partial_\mu \chi \partial^\mu \chi + V(\chi), \end{aligned} \quad (2.2)$$

where the potential ($V(\chi)$) reproduces the trace anomaly and minimizing $V(\chi)$ leads to a finite vacuum expectation value ($\chi_0 \equiv \langle 0 | \chi | 0 \rangle$, where $|0\rangle$ is the vacuum at zero density). The χ_0 is the order parameter associated to the introduced behavior that mimics the spontaneous breaking of scale invariance. In QCD, the order parameter associated to trace anomaly is the gluon condensate, and so the χ_0 is analogous to the gluon condensate.

Rho and Brown then took Eq. 2.2 one step further [76] and subdivided the glueball field (χ) into

$$\chi = \chi_* + \chi', \quad (2.3)$$

where χ_* represents the minimum of the field as density increases and scales the quark condensate in a dense medium, and χ' represents a fluctuating glueball field and scales the gluon condensate in a dense medium. The quark condensate (*i.e.*, $\langle 0|\bar{q}q|0\rangle$ or $\langle\bar{\psi}\psi\rangle$ as given in Sec. 1.1) scaling is given by

$$\frac{\langle 0^*|\bar{q}q|0^*\rangle}{\langle 0|\bar{q}q|0\rangle} = \left(\frac{\chi_*}{\chi_0}\right)^3, \quad (2.4)$$

where $\chi_* \equiv \langle 0^*|\chi|0^*\rangle$ and $|0^*\rangle$ is the vacuum at non-zero density (*i.e.*, ground state). Scaling of the quark condensate leads to the following definition of the effective pion decay constant (f_π^*):

$$f_\pi^* = f_\pi \chi^*/\chi_0, \quad (2.5)$$

which is used to establish a relationship between the scaling of the quark condensate and the vector meson mass scaling via the Kawarabayashi-Suzuki-Riazuddin-Fayyazuddin (KSRF) relation [88, 89], $m_V^2 = 2g^2 f_\pi^2$, where m_V is the mass of the vector meson, g^2 is the gauge coupling constant, and f_π is the pion decay constant. Brown and Rho [76] then extended Eq. 2.5, which is only applicable in the vacuum, to be applicable in the presence of a medium such that the effective mass of the vector mass follows $m_V^{*2} = 2g^{*2} f_\pi^{*2}$. Since g is a gauge coupling constant, g is scale invariant and no χ field is applied to g ; therefore, when the non-zero density is introduced, g does not depend on χ^* and gives $g^* = g$. With $g^* = g$, the KSRF relation leads to $m_V^*/m_V \approx f_\pi^*/f_\pi$ with the introduction of non-zero density (a medium).

To provide a means of quantifying m_V^*/m_V , a connection between the scaling of the vector meson mass and the scaling of the nucleon mass (m_N^*/m_N) needs to be made,

where m_N^* is the effective mass of a nucleon. The connection is made by introducing the subdivided χ field (refer to Eq. 2.3) and the effective pion decay constant (refer to Eq. 2.5) to the Skyrme Lagrangian with a glueball field (refer to Eq. 2.2) and rewriting the equation as:

$$\begin{aligned} \mathcal{L} = & \frac{f_\pi^{*2}}{4} Tr(\partial_\mu U \partial^\mu U^\dagger) + \frac{\eta^2}{4} Tr[U^\dagger \partial_\mu U, U^\dagger \partial_\nu U]^2 \\ & + c \left(\frac{f_\pi^*}{f_\pi} \right)^3 Tr(MU + H.c.) + \dots, \end{aligned} \quad (2.6)$$

where $U(x) = e^{i\pi^*/f_\pi^*}$, $\pi^* \equiv \pi\chi^*/\chi_0$, $H.c.$ is the Hermitian conjugate, and the ellipsis represents the additional terms with the χ' field. A relationship between the effective pion decay constant and the effective mass of a nucleon can be formed by using the baryon mass (M_B) relationship ($M_B \sim g_A^{\frac{1}{2}} f_\pi$) from the Skyrme Lagrangian (refer to Eq. 2.1) [90, 91], the dense medium equivalent of the baryon mass ($M_B^*(\rho) \sim g_A^*(\rho)^{\frac{1}{2}} f_\pi^*(\rho)$), and the Lagrangian in Eq. 2.6. The effective nucleon (*i.e.*, baryon) mass follows $m_N^*/m_N \approx (g_A^*/g_A)^{\frac{1}{2}} f_\pi^*/f_\pi$, where m_N is the nucleon mass. Again, since the axial-vector coupling constant, g_A , is scale invariant, $m_N^*/m_N \approx f_\pi^*/f_\pi$ and $m_V^*/m_V \approx f_\pi^*/f_\pi \approx m_N^*/m_N$. Given that the effective nuclear mass at nuclear matter density (ρ_0) is less than the nuclear mass in the vacuum (*e.g.*, $m_N^*(\rho_0)/m_N \approx 0.8$), the mass of the vector meson (*e.g.*, ρ -meson) will drop in the presence of a dense medium. Comparisons between predictions of the density induced mass scaling (*i.e.*, dropping mass) model and the measurements from the CERN experiments CERES [15] and NA60 [16] have been made (as shown in Sec. 2.5). For more information on Brown-Rho scaling, refer to this review [92].

2.3 Effective Many-body Theory by Rapp *et al.*

Rapp, van Hess, Wambach, and others [78, 79, 80, 81, 35] have worked together to create an effective many-body model that describes the production of e^+e^- in the presence of a dense medium. In the many-body model, the e^+e^- production rates are propagated through the space-time evolution of a thermal fireball (*i.e.*, the $A + A$ collision), resulting in the production of e^+e^- pairs. In this thesis, the e^+e^- pair production of the many-body model and experimental data are compared.

2.3.1 Thermal e^+e^- Production Rate

The thermal rate of e^+e^- pair production (N_{ee}) per unit four-volume (d^4x) and unit four-momentum (d^4q) is [93, 94]

$$\frac{dN_{ee}}{d^4x d^4q} = -\frac{\alpha^2}{3\pi^2} \frac{L(M)}{M^2} \text{Im}\Pi_{EM}(M, \vec{q}) f_B(q_0; T), \quad (2.7)$$

where α is the electromagnetic coupling constant ($\frac{e^2}{4\pi} \simeq \frac{1}{137}$), M is the e^+e^- invariant mass, $L(M)$ is the final-state phase-space factor, f_B is the thermal Bose function with q_0 being the e^+e^- energy and T being the temperature, and $\text{Im}\Pi_{EM}(M, \vec{q})$ is the imaginary component of the electromagnetic spectral function with \vec{q} representing the three-momentum of a e^+e^- pair in the local rest frame of the medium (*i.e.*, QGP or hadron gas). In the vacuum, the electromagnetic spectral function ($\text{Im}\Pi_{EM}^{vac}$) can be split into two scenarios. One scenario is in the low mass region ($M < 1.5 \text{ GeV}^{-2}$) and the other scenario is the high mass region ($M > 1.5 \text{ GeVc}^{-2}$). The $\text{Im}\Pi_{EM}^{vac}$ in the low mass region follows the Vector Meson Dominance (VDM) model [95] as given by

$$\text{Im}\Pi_{EM}^{vac} = \left(\frac{m_\omega^2}{g_\omega}\right)^2 \text{Im}D_\omega(M) + \left(\frac{m_\rho^2}{g_\rho}\right)^2 \text{Im}D_\rho(M) + \left(\frac{m_\phi^2}{g_\phi}\right)^2 \text{Im}D_\phi(M), \quad (2.8)$$

where $D_V = \frac{1}{M^2 - m_V^2 - \Sigma_V}$ is the vector meson propagators, Σ_V is the self-energy, V is the type of vector meson (*i.e.*, ρ , ω , ϕ), m_V is the mass of the vector meson, and g_V is the coupling constant of the vector meson in the VDM. In the high mass region, the $\text{Im}\Pi_{EM}^{vac}$ is the rate of the annihilation of $q\bar{q}$ into e^+e^- or the reverse ($e^+e^- \rightarrow q\bar{q}$),

$$\text{Im}\Pi_{EM}^{vac} = \frac{-M^2}{12\pi} \left(1 + \frac{\alpha_s(M)}{\pi} + \dots \right) N_c \sum_{q=u,d,s} (e_q)^2, \quad (2.9)$$

where N_c is the number of quark colors ($N_c = 3$), e_q is the electric quark charge for the light flavored quarks (u , d , s), α_s is the strong coupling constant, and the $\frac{\alpha_s(M)}{\pi} + \dots$ terms represent higher-order corrections where the quark and/or anti-quark may radiate gluons.

In the medium, the ρ , ω , and ϕ vector meson propagator functions (D_ρ , D_ω , and D_ϕ) need to include the effects of the medium in their self-energies, which broaden the electromagnetic spectral functions closer to the phase-transition region between the QGP and hadron gas phases (*i.e.*, broadens more at higher temperatures). At the top $Au + Au$ collision energies produced at RHIC, the ω is expected to contribute $< 10\%$ to the thermal dielectron rate and the ϕ is assumed not to contribute to the thermal rate of e^+e^- pair production since the phase change temperature is high enough for the quark-antiquark pair that forms the ϕ to decouple in the medium [13].

The ρ propagator, with transverse (T) and longitudinal (L) modes, is:

$$D_\rho^{L,T} = \frac{1}{M^2 - (m_\rho^0)^2 - \sum_{\rho\pi\pi}^{L,T} - \sum_{\rho M}^{L,T} - \sum_{\rho B}^{L,T}}, \quad (2.10)$$

where $\sum_{\rho\pi\pi}$ represents the self-energy of the ρ and the pion cloud, $\sum_{\rho M}$ represents the self-energy of the ρ interacting with other mesons (π , K , \bar{K} , ρ ...), and $\sum_{\rho B}$ represents the self-energy of the ρ interacting with baryons (N , Δ , $N(1440)$, $N(1520)$...). The values of the self-energies of the ρ have been parameterized using resonance decay and vacuum scattering data [96, 79, 80]. Diagrams of the self-energies are shown

in Fig. 2.1. Note that in the vacuum, the baryon and meson self-energies vanish while

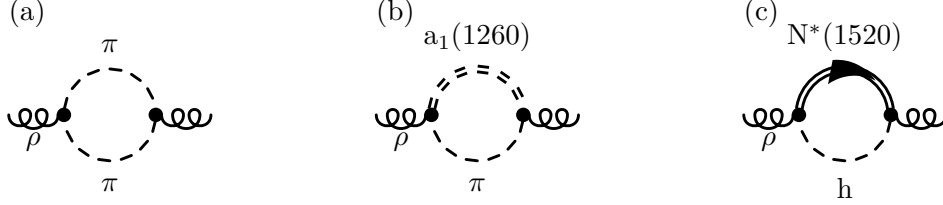


Figure 2.1 : Example self-energy diagrams that are considered a part of the in-medium ρ propagator. (a) The self-energy of the ρ and its pion cloud. (b) The self-energy of the ρ interacting with mesons, in this case, $a_1(1260)$. (c) The self-energy of the ρ interacting with baryons, in this case, $N^*(1520)$.

the pion cloud self-energy still contributes to ρ propagator and is responsible for the wide resonance of the ρ . Also, in a low baryonic chemical potential environment, the anti-baryons are about as abundant as baryons. Since ρ^0 is its own anti-particle, the self-energy of ρ interacting with baryons is almost doubled in relativistic heavy-ion collisions, where the collisions can produce a dense baryonic environment (a small μ_B is associated to a small net baryon density $((B - \bar{B})/V)$, and if dense, a high total baryon density $((B + \bar{B})/V)$), and is responsible for most of the ρ propagator contribution in relativistic heavy ion collisions.

The ω propagator follows:

$$D_\omega = \frac{1}{M^2 - im_\omega^2 (\Gamma_{3\pi} + \Gamma_{\rho\pi} + \Gamma_{\omega\pi \rightarrow \pi\pi}) - \Sigma_{\omega\pi b_1} - \Sigma_{\omega B}}, \quad (2.11)$$

where the decay width ($\Gamma_{\rho\pi}$) accounts for the direct $\omega \rightarrow \rho\pi$ decay, $\Gamma_{3\pi}$ accounts for the direct $\omega \rightarrow \pi\pi\pi$ decay, $\Gamma_{\omega\pi \rightarrow \pi\pi}$ accounts for the ω absorption in the inelastic decay $\omega\pi \rightarrow \pi\pi$, $\Sigma_{\omega\pi b_1}$ is the self-energy of ω scattering off π and generating a b_1 meson, and $\Sigma_{\omega B}$ is the self-energy of ω interacting with baryons. The self energies of ω have also been parameterized [96, 79, 80]. The ϕ propagator (D_ϕ) will not be discussed

in this thesis since D_ϕ is not expected to contribute to the thermal distribution of e^+e^- pairs. For e^+e^- invariant masses $\geq 1 \text{ GeV}c^{-2}$, the annihilation of $\pi\pi\pi\pi$ are added to the thermal distribution of e^+e^- pairs and have been parameterized using measurements on the decay τ in a vacuum [97].

Contribution of the QGP to the thermal distribution of e^+e^- pairs is modeled using an electromagnetic spectral function that has been parameterized by thermal lattice QCD rates (with a q dependence that has been convoluted from leading-order perturbative QCD photon rates) [35]. The thermal lattice QCD rates are derived by relating the Euclidean-time correlation function (Π_V) to the electromagnetic spectral function [98]. The Euclidean-time correlation function is

$$\Pi_V(\tau, q; T) = \int_0^\infty \frac{dq_0}{2\pi} (-2\text{Im}\Pi_i^i(q_0, \vec{q}; T)) \frac{\cosh[q_0(\tau - 1/(2T))]}{\sinh[q_0/(2T)]}, \quad (2.12)$$

where T is the temperature.

The Euclidean-time correlation function is then taken to be in the limit where the temperature is greater than the QGP to Hadron Gas phase change temperature and $\vec{q} = 0$ (such that $M = q_0$). The behavior of Π_V , when normalized to the non-interacting perturbative QCD limit, is approximated by splitting the function into a low-energy Breit-Wigner (BW) term and a perturbative continuum ($p.c.$) term [98],

$$-2\text{Im}\Pi_V^{ii}(q_0) = BW + p.c., \quad (2.13)$$

where the Breit-Wigner term is given as

$$BW = S_{BW} \frac{q_0 \Gamma / 2}{q_0^2 + \Gamma^2 / 4}, \quad (2.14)$$

with the strength (S_{BW}) and width (Γ) of the Breit-Wigner peak, and the perturbative continuum term is given as

$$p.c. = \frac{C_{EM} N_c}{2\pi} (1 + \kappa) q_0^2 \tanh\left(\frac{q_0}{4T}\right), \quad (2.15)$$

with $C_{EM} \equiv \sum_q e_q^2$ for light quark flavors (u, d, s) and κ representing the deviation from the limit of $T \rightarrow \infty$ and large q_0 —in this limit, $\kappa \approx \frac{\alpha_s}{\pi}$. To give $-2\text{Im}\Pi_V^i(q_0)$ a dependence on three-momentum, the Breit-Wigner term is replaced with the leading order perturbative QCD photon rate as a function of three-momentum. Ultimately, the electromagnetic spectral function for QGP emission has the following form:

$$- \text{Im}\Pi_T = \frac{C_{EM}N_c}{12\pi} M^2 \left(\hat{f}_2(q_0, \vec{q}; T) + 2\pi\alpha_s \frac{T^2}{M^2} KF(M^2) \ln \left(1 + \frac{2.912 q_0}{4\pi\alpha_s T} \right) \right),$$

$$\Pi_L = (M^2/q_0^2)\Pi_T, \quad (2.16)$$

where $K = 2$ is a factor selected to improve the function's description of lattice QCD results, $F(M^2) = \frac{4T^2}{4T^2+M^2}$ is a form factor selected to improve the function's behavior at higher energies, and

$$\hat{f}_2(q_0, \vec{q}; T) = \left(1 + \frac{2T}{q} \ln \left[\frac{1 + e^{-(q_0+q)/2T}}{1 + e^{-(q_0-q)/2T}} \right] \right). \quad (2.17)$$

The e^+e^- pair yields ($dN_{ee}/dMdy$, the number of e^+e^- pairs (N_{ee}) per invariant mass (M) and rapidity (y) bins) are found by integrating the e^+e^- pair production rates over the evolution of the medium (*i.e.*, from the time of the QGP formation until kinetic freeze-out) [81], using the following equation:

$$\frac{dN_{ee}}{dMdy} = \frac{M}{\Delta y} \int_0^{\tau_{fo}} d\tau \int_{V_{FB}} d^3x \int \frac{d^3}{q_0} \frac{dN_{ee}}{d^4x d^4q} A(M, q_t, y). \quad (2.18)$$

Here, Δy represents the rapidity gap set by the user, $A()$ is a function describing the detector acceptance of the experiment (*i.e.*, the measurable phase space of the experiment), V_{FB} is the time-dependent volume of the fireball, τ is the time from the start of the fireball, and $\frac{dN_{ee}}{d^4x d^4q}$ is the rate of the e^+e^- production. The fireball volume is an isotropically expanding cylindrical volume described by [97]

$$V_{FB}(t) = \pi \left(r_{\perp,0} + \frac{1}{2}a_{\perp}t^2 \right)^2 \left(z_0 + v_{z,0}t + \frac{1}{2}a_z t^2 \right), \quad (2.19)$$

where z_0 is the initial longitudinal size, $v_{z,0}$ is the initial longitudinal expansion velocity of the edges, a_z is the longitudinal expansion acceleration, $r_{\perp,0}$ is the initial transverse overlap of the colliding ions, and a_{\perp} is the transverse acceleration of the fireball. The thermodynamics of this cylindrical fireball model is used to determine the temperature and baryonic chemical potential of the system, both of which influence the e^+e^- production rates.

By asserting that the total entropy (S_{total}) for each collision is constant, the volume of the fireball is related to the entropy density (s) of the fireball by $S_{total} = V_{FB}(\tau) \cdot s(\tau)$. By substituting the entropy density into an equation-of-state, the chemical potential and temperature of the fireball are determined. The equation-of-state used is derived from [99], which is based on the default AZHYDRO code [100, 101]. The equation-of-state for the QGP ($T > 170 MeV$ [35]) is given by lattice QCD calculations, which are matched to an equation-of-state for a hadron gas at the phase change temperature. After chemical freeze-out, the equation-of-state for a hadron gas is used for the lower temperatures until kinetic freeze-out.

With an effective many-body model, Rapp and van Hees [13] show that the thermal e^+e^- yield has a trend similar to the trend in the fireball lifetime (*i.e.*, the total e^+e^- emission time of the fireball) in the low invariant mass region ($0.3 \text{ GeVc}^{-2} < M_{ee} < 0.7 \text{ GeVc}^{-2}$) (as shown in Fig. 2.2). Lifetime is the total e^+e^- emission time of the fireball.

A review of predictions of the production of $\mu^+\mu^-$ and e^+e^- pairs with the effective many body model by Rapp *et al.* and the comparisons with experimental measurements are presented in Sec. 2.5. In this thesis, the e^+e^- pair production from the effective many-body model by Rapp *et al.* is compared to e^+e^- pair measurements presented and is used to study the possible connection between the measured

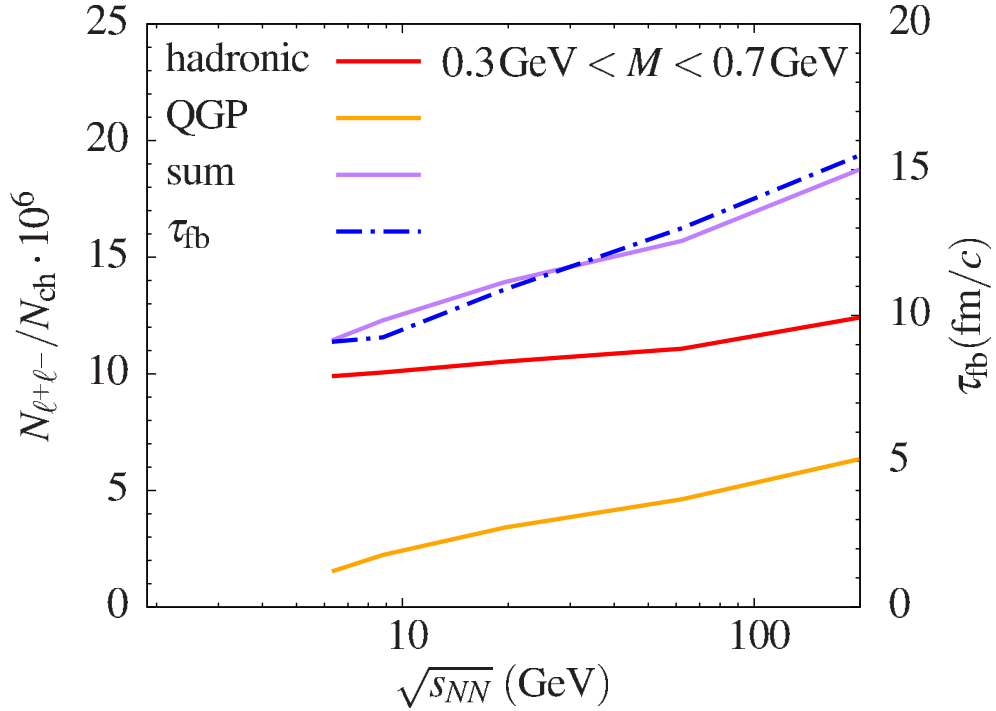


Figure 2.2 : The comparison of the e^+e^- yield normalized by the number of charged particles in the collision and the lifetime of the fireball as a function of $\sqrt{s_{NN}}$. The solid purple line represents the normalized total yield from the hadronic component (red short-dashed line) and the QGP component (yellow dashed line) with the quantity indicated by the left y-axis. The blue dot-dashed line is the fireball lifetime and the duration is indicated on the right y-axis. This figure was taken from [13].

e^+e^- pairs to the lifetime of the collision.

2.3.2 Chiral Symmetry Restoration Observable

Rapp *et al.*'s effective many-body theory only describes the ρ spectral function modification through collisional broadening. To make a link between the ρ spectral function and chiral symmetry restoration, Hohler and Rapp [14] have been working on an $a_1(1260)$ spectral function ansatz for comparison with the ρ spectral function (refer to Eqs. 2.8 and 2.10) with the Weinberg sum rules, the QCD rules, and lattice

QCD parameterizations. The Weinberg sum rules are used to relate the difference between the ρ spectral function and a_1 spectral function to chiral order parameters. The QCD sum rules are used to relate each spectral function with the quark and gluon condensates. The chiral order parameters, which include the quark and gluon condensates, have been parameterized to help constrain the rules. The results of the ansatz a_1 spectral function and ρ spectral function at different temperatures are shown in Fig. 2.3, where the ρ spectral function is the black curve and the a_1 spectral function is the red curve. In Fig. 2.3 from left to right, notice how both spectral functions begin to modify. The ρ spectral function decreases in amplitude and broadens as the temperature increases, while the a_1 spectral peak shifts toward the ρ spectral function peak position as temperatures increase. The shifting of the a_1 spectral function is mostly controlled by the Weinberg sum rules, while the shape of the spectral functions at higher temperatures is mostly controlled by the QCD sum rules. Once the temperature reaches 170 MeV, the two spectral functions begin to overlap, or rather, to become degenerate, which is an observable of chiral symmetry restoration. This observation means that the ρ spectral function, which has had success describing experimental measurements, is compatible with chiral symmetry restoration.

2.4 Parton-Hadron-String Dynamics

Parton-Hadron-String Dynamics (PHSD) is a model by Linnyk, Bratkovskaya, Cassing, *et al.* [82]. The model is “a microscopic covariant transport model that incorporates effective partonic, as well as hadronic degrees of freedom, and involves a dynamic description of the hadronization process from partonic to hadronic matter,” as defined by [83]. The model has been extended to study the production of e^+e^- [85]

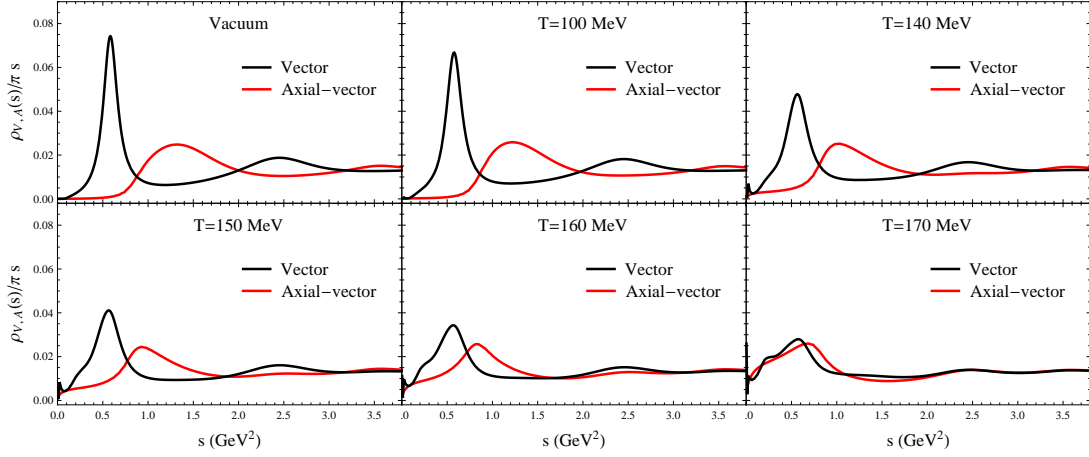


Figure 2.3 : The a_1 (red) and ρ (black) spectral functions at different temperatures. This figure was taken from [14].

and can be broken down into five chronological stages starting from the beginning to the end of the collision: (1) Initial Collisions and Conditions, (2) Formation of a Quark-Gluon Plasma, (3) Partonic Stage – Quark-Gluon Plasma, (4) Hadronization, and (5) Hadronic Stage.

2.4.1 Initial Collisions/Conditions

The collision of heavy ions are setup by having the ions travel toward each other with a normalized velocity ($\beta = \frac{v}{c}$) corresponding to the center-of-mass energy per nucleon pair ($\sqrt{s_{NN}}$) of interest. The heavy ions are represented as a group of nucleons that undergo binary nucleon-nucleon collisions. The distribution of the nucleons and the number of binary collisions follow similar prescription as the Ultrarelativistic Quantum Molecular Dynamics (UrQMD) model [102, 83]. UrQMD is a microscopic transport model that simulates heavy-ion collisions on an event-by-event basis. Each collision follows the LUND string model [103] as setup in PYTHIA5.7/JETSET [104]

to form strings that represent pre-hadrons. The pre-hadrons either form hadrons or melt into the QGP depending upon the energy density with respect to the critical energy density.

2.4.2 Formation of a Quark-Gluon Plasma

If the energy density of the medium is greater than the critical energy density of the medium, the pre-hadrons are melted into quarks (q) and gluons (g) that are massive (*i.e.*, quasiparticles). The same approach is taken in the A Multi-Phase Transport Model for Relativistic Heavy Ion Collisions (AMPT) [105]. The pre-mesons melt into $q\bar{q}$ pairs and the pre-baryons melt into a $q + qq$ pair, and then the qq decays into $q + q$. These quasiparticles are then handled by the Dynamical QuasiParticle Model [106].

2.4.3 Partonic Stage – Quark-Gluon Plasma

In the situation where the energy density is high enough and the partons have not been hadronized, the Dynamical QuasiParticle Model (DQM) is used to propagate the partonic stage. The DQM gives the quarks and gluons mass and width that depend on the temperature of the medium and have been parameterized to lattice QCD calculations [84]. This finite width does not vanish, which is different than other quasiparticle models. In DQM, the quarks and gluons interact in elastic and inelastic collisions—the elastic collisions modeled are $q + q \rightarrow q + q$, $q + \bar{q} \rightarrow q + \bar{q}$, $\bar{q}\bar{q} \rightarrow \bar{q}\bar{q}$, $g + q \rightarrow g + q$, $g + \bar{q} \rightarrow g + \bar{q}$, and $g + g \rightarrow g + g$, and the inelastic collisions modeled are $q + \bar{q} \rightarrow g$, $g \rightarrow q + \bar{q}$, $q + \bar{q} \rightarrow g + g$, and $g \rightarrow g + g$.

2.4.4 Hadronization

As the partons travel outward from the start of the collision (in time and direction) and the energy density decreases, the Dynamical QuasiParticle Model begins to evaluate whether the partons will hadronize or not. Hadronization occurs when the energy density drops below the critical energy density, and the partons hadronize by grouping together within their local phase-spaces to form the pre-hadrons of mesons and baryons, where $q + \bar{q} \rightarrow \text{meson}$, $q + q + q \rightarrow \text{baryons}$, and $g \rightarrow q + \bar{q}$, which can then combine with neighboring partons.

2.4.5 Hadronic Stage

The pre-hadrons, produced either at the initial collision in regions of low energy density or by partons that have been hadronized via DQM, then follow the off-shell transport model, Hadron-String-Dynamics [107], as a many-body approach limited to two-body correlations. The Hadron-String-Dynamics model operates as a coupled set of transport equations for a hadron that has the phase distribution ($f_h(x, p)$);

$$\begin{aligned}
& \{(\Pi_\mu - \Pi_\nu \partial_\mu^p U_h^\nu - M_h^* \partial_\mu^p U_h^S) \partial_x^\mu + (\Pi_\nu \partial_\mu^x U_h^\nu + M_h^* \partial_\mu^x U_h^S) \partial_p^\mu\} f_h(x, p) \\
&= \sum_{h_2 h_3 h_4 \dots} \int d_2 d_3 d_4 \dots [G^\dagger G]_{12 \rightarrow 34 \dots} \delta_\Gamma^4 (\Pi + \Pi_2 - \Pi_3 - \Pi_4 \dots) \\
&\times \{f_{h_3}(x, p_3) f_{h_4}(x, p_4) \bar{f}_h(x, p) \bar{f}_{h_2}(x, p_2) - f_h(x, p) f_{h_2}(x, p_2) \bar{f}_{h_3}(x, p_3) \bar{f}_{h_4}(x, p_4)\} \dots,
\end{aligned} \tag{2.20}$$

where Π represents an effective four-momentum, $U_h^S(x, p)$ represents the vector hadron self-energy, U_h^μ represents the axial hadron self-energy, M^* represents the effective mass, $\bar{f}_h(x, p) = 1 \pm f_h(x, p)$, and “ $G^\dagger G \delta^4 \dots$ ” represents the transition rates in the collision and the “ \dots ” represents additional terms to the collisions if more than two hadrons are involved in the final and/or initial channels.

2.4.6 e^+e^- Production

The e^+e^- pairs are modeled in PHSD by incorporating e^+e^- production from partonic and hadronic sources. The partonic sources are $q + \bar{q} \rightarrow \gamma^*$, $q + \bar{q} \rightarrow g + \gamma^*$, $q + g \rightarrow q + \gamma^*$, and $\bar{q} + g \rightarrow \bar{q} + \gamma^*$, where $\gamma^* \rightarrow e^+e^-$. The cross-sections of these e^+e^- sources are parameterized through the use of the Dynamical QuasiParticle Model [108, 109]. The hadronic sources are the following: (1) the direct decay of the vector mesons, ω , ρ , ϕ , J/Ψ , and Ψ' ; (2) the Dalitz decays of mesons and baryons, π^0 , η , η' , a_1 , Δ , and ω ; (3) Drell-Yan decays, $q + \bar{q} \rightarrow e^+e^-$; (4) the radiation from secondary meson interactions, $\pi + \pi$, $\pi + \rho$, $\pi + \omega$, $\rho + \rho$, and $\pi + a_1$; and (5) the correlated semi-leptonic decays of D-mesons and B-mesons.

The vector mesons are effectively modified in the medium by collisional broadening of the spectral function and, if the option is enabled, a dropping mass shift induced by a dense medium like the aforementioned Rho-Brown scaling in Sec. 2.2. The collisional broadening is incorporated in the definition of the modified vector meson width (Γ_V^*) by summing linearly an additional term:

$$\Gamma_V^*(M, |\vec{p}|, \rho_N) = \Gamma_V(M) + \Gamma_{coll}(M, |\vec{p}|, \rho_N), \quad (2.21)$$

where $\Gamma_V(M)$ is the vacuum vector meson width, $\Gamma_{coll}(M, |\vec{p}|, \rho_N)$ is the collisional width, and ρ_N is the baryon density. The incorporation of collision broadening causes the vector meson spectral function to broaden as the density increases and is proportional to $\frac{\rho_N}{\rho_0}$. The dropping mass is given as:

$$M_0^*(\rho_N) = \frac{M_0}{(1 + \alpha \frac{\rho_N}{\rho_0})}, \quad (2.22)$$

where M_0^* is the dropping pole mass, M_0 is the vacuum pole mass, and α is a vector meson dependent parameter.

Since the production of e^+e^- by $A + A$ collisions is infrequent, the transport calculation (refer to Eq. 2.20) uses a perturbative method to increase the production of e^+e^- . The perturbation of the transport calculation is referred to as a time integration method where e^+e^- are allowed to be emitted up until the time that the resonance is either absorbed by the medium or decayed strongly. An example of the time integration method is provided in [82] and shown as follows:

$$\frac{dN^{\rho \rightarrow e^+e^-}}{dM} = \sum_{t=0}^{t_F} \Gamma^{\rho \rightarrow e^+e^-}(M) \cdot \frac{\Delta t}{\gamma(\hbar c)} \cdot \frac{1}{\Delta M}, \quad (2.23)$$

where ΔM represents the mass bin, Δt represents the length of a time step in fm/c, γ is the ρ 's Lorentz factor with respect to the frame of the medium, and $\Gamma^{\rho \rightarrow e^+e^-}(M)$ represents the electromagnetic decay width, as follows:

$$\Gamma^{\rho \rightarrow e^+e^-}(M) = \frac{\Gamma^{\rho \rightarrow e^+e^-}(M_0)}{M_0} \frac{M_0^{*4}}{M^3}, \quad (2.24)$$

where M_0 is the vacuum pole mass and M_0^* is the medium modified mass. If the dropping mass option is disabled, the medium modified mass is the vacuum pole mass; otherwise, the medium-modified mass follows Eq. 2.22.

2.5 Past Results

The Rho-Brown scaling theory, the effective many-body model by Rapp *et al.*, and the PHSD model have been evaluated against data to determine whether a dropping mass or broadening of the spectral function best describes the production of e^+e^- pairs. One of the first evaluations of the theoretical models against data was with e^+e^- pairs produced in Pb+Au collisions at 158 AGeV collected by the CERES Collaboration at the CERN Super Proton Synchrotron [44, 15]. The CERES Collaboration reported a deviation of the measured e^+e^- yield from the expected hadronic cocktail at freeze-out as is shown in Fig. 2.4. On the right panel in Fig. 2.4, model calculations from the

dropping mass of the ρ (the dashed blue line) and the broadening of the ρ spectral function (the long-dashed red line) have been added to hadronic cocktail. Neither model calculation could be ruled out with this data sample. One might be able to argue that the cocktail with the broadened ρ spectral function describes the data better than the cocktail with the dropping ρ mass in between ω and ϕ masses while there are points below the ω mass that tend to agree better with the cocktail with the dropping mass scenario.

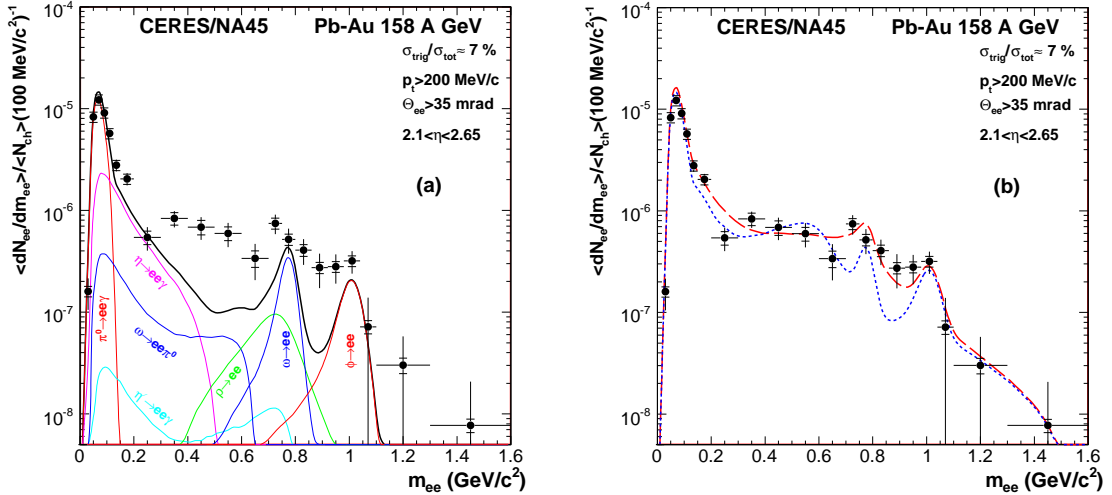


Figure 2.4 : (Left) The black solid points represent the e^+e^- invariant mass spectrum. The black solid line represents the hadronic cocktail (the summation of simulated known contributions to the e^+e^- continuum) with its components represented by the colored lines. (Right) The same invariant mass data are shown as black solid points with a dashed blue line representing hadronic cocktail calculations with a dropping ρ mass and a long-dashed red line representing hadronic cocktail calculations with a broadened ρ -spectral function. This figure was taken from [15].

Another CERN Super Proton Synchrotron experiment, NA60, measured the $\mu^+\mu^-$ continuum in In+In collisions at 158 AGeV in the low-mass region with greater precision than CERES, as shown in Fig. 2.5 [16]. In Fig. 2.5, comparisons between the

NA60 data and models that include the dropping mass scenario and the broadening of the ρ spectral function are shown. These comparisons effectively ruled out the mass dropping scenario as the only cause for the modification of the ρ as shown in the right panel of Fig. 2.5 where the broadening of the ρ spectral function (the blue line) agrees with the data while the mass dropping scenario (the dashed green line) does not describe the data. However, some models still consider the dropping mass scenario in conjunction with other medium effects (*e.g.*, PHSD has the option to include the dropping mass scenario along with collisional broadening).

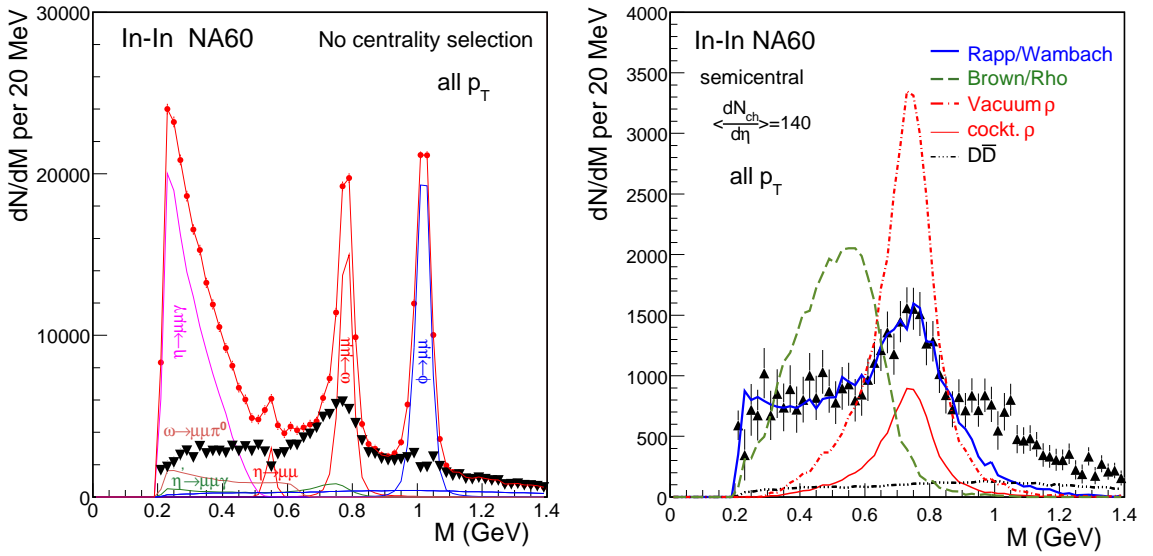


Figure 2.5 : (Left) The solid red points represent the invariant mass measurement, while the solid red line connects the points. The other solid colored curves represent expected hadronic contributions to the $\mu^+\mu^-$ mass spectrum. The solid black triangles represent the difference between the data (red points) and the expected contributions (colored curves). (Right) The $\mu^+\mu^-$ invariant mass difference (solid black triangles) between the hadronic contributions and data points similar to (Left), but a different centrality selection. The curves show model predictions when using a broadened spectral function (Rapp/Wambach, solid blue curve), an unmodified spectral function (Vacuum ρ , dot-dashed red curve), a cocktail ρ based on the ratio $\rho/\omega = 1.2$ (cockt. ρ , solid red curve), and $D\bar{D} \rightarrow \mu^+\mu^- X$. This figure was taken from [16].

At RHIC, both STAR and PHENIX have measured the e^+e^- invariant mass spectrum in Au+Au collisions at $\sqrt{s_{NN}} = 200$ GeV and measurements agree with the effects of the medium on the ρ spectral function [17, 18]; the measurements are shown in Fig. 2.6. In Fig. 2.6, the STAR experiment presented the results of both the PHSD model (the dot-dashed blue curve) and the effective many-body theory by Rapp *et al.* (the solid red curve) in comparison with the excess data (where excess data is defined as the difference between the e^+e^- measurement and the hadronic cocktail, which does not contain contributions from ρ and partonic emission). In Fig. 2.6, the PHENIX experiment presented results of the effective many-body theory by Rapp *et al.*'s ρ (the dashed red curve) and partonic emission (the dashed blue curve). The contributions by Rapp *et al.* have been added to the hadronic cocktail (the dashed green curve) to form the total expected e^+e^- emission (the solid black line). In both cases, the models are in agreement with the measured excess. Given the uncertainties on the STAR data points, it is difficult to distinguish which model agrees better with data, although PHSD might perform better in the lowest and intermediate mass regions as seen in the lower left panel of Fig. 2.6. In any case, these measurements demonstrate a modification of the ρ meson, which can be described by models that incorporate a broadening of the ρ spectral function. However, at an order of magnitude higher in $\sqrt{s_{NN}}$ at the Large Hadron Collider, the ALICE collaboration shows preliminary e^+e^- pair production in Pb+Pb at $\sqrt{s_{NN}} = 2.76$ TeV. The e^+e^- pair measurements by ALICE are consistent with the hadronic cocktail and no sensitivity for a measured excess yield in the low-mass region [110], which is different than what has been observed at RHIC.

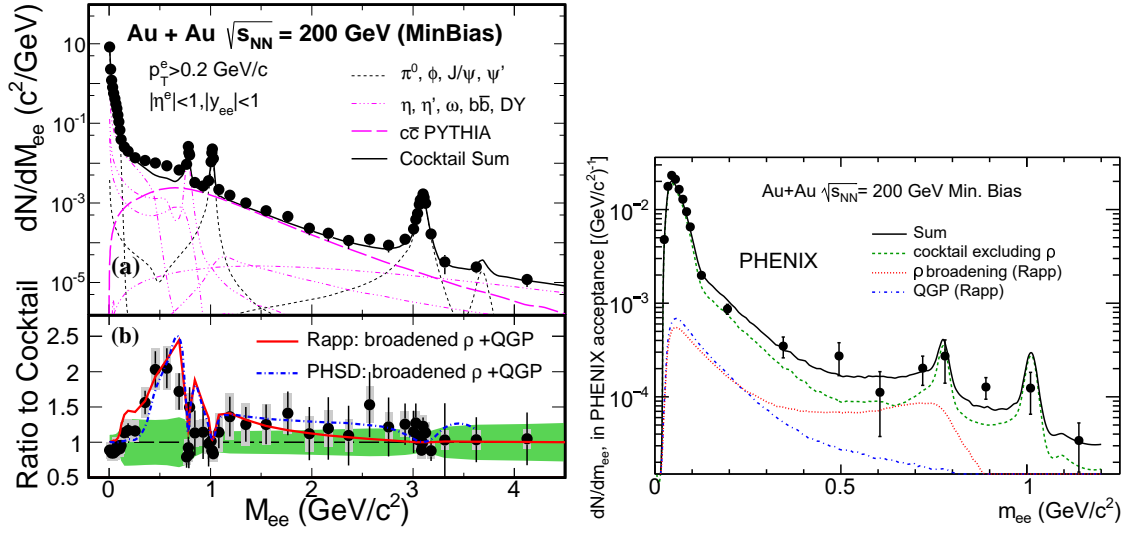


Figure 2.6 : (Left a) STAR's e^+e^- invariant mass spectrum produced from 0-80% centrality Au+Au minimum-bias collisions at $\sqrt{s_{NN}} = 200$ GeV shown as the solid black points. The solid black curve represent the hadronic cocktail and the sum of the known hadronic sources (perforated multicolored curves) excluding ρ . (Left b) The solid black points represents the ratio of data to the hadronic cocktail. The solid red curve represents the ratio of the effective many-body theory plus the hadronic cocktail to the cocktail. The dashed blue curve represents the ratio of Parton-Hadron-String Dynamics (PHSD) plus the hadronic cocktail to the hadronic cocktail. (Right) PHENIX's e^+e^- invariant mass spectrum produced from 0-92% centrality Au+Au minimum-bias collisions at $\sqrt{s_{NN}} = 200$ GeV shown as the solid black points. The hadronic cocktail without ρ contributions is represented by the dashed green curve. The contributions, ρ and QGP, from the effective many-body theory are shown as the dashed red and dashed blue lines, respectively. The solid black line represents the total expected contribution to the e^+e^- invariant mass spectrum. The left and right figures were taken from [17, 18], respectively.

2.6 Goal for the Beam Energy Scan Program

The Beam Energy Scan Program at RHIC collided Au on Au from $\sqrt{s_{NN}} = 7.7$ to 62.4 GeV and was able to produce e^+e^- pairs from collisions at energies as high ($Pb+Au$ at $\sqrt{s_{NN}} = 17.3$ GeV) as those produced at the Super Proton Synchrotron (SPS) and at energies an order of magnitude higher than SPS at the top energy at RHIC ($Au + Au$

at $\sqrt{s_{NN}} = 200$ GeV). This provides an excellent opportunity to create an excitation function of e^+e^- production for the following reasons: (1) the program spans across the collision energy gap in-between the previous measurements at SPS ($\sqrt{s_{NN}} = 17.3$ GeV) and RHIC ($\sqrt{s_{NN}} = 200$ GeV), (2) the program uses the same colliding species (*e.g.*, Au), and (3) the program enables the same detector to make measurements at each collision energy (STAR). The Beam Energy Scan Program collected enough data to produce statistically significant e^+e^- measurements of the invariant mass spectrum for minimum-bias Au+Au collisions with a 0-80% centrality at $\sqrt{s_{NN}} = 19.6, 27, 39, \text{ and } 62.4$ GeV. At these collision energies, the average chemical freeze-out temperature (T_{ch}) is approximately constant [19] and is shown in Fig. 2.7. Also, the total baryon density is near constant from $\sqrt{s_{NN}} = 20$ GeV to 200 GeV as shown in Fig. 2.8, where the ratio of protons to π is presented as a function of $\sqrt{s_{NN}}$. Since both the effective many-body model by Rapp *et al.* and the PHSD model incorporate a broadening of the ρ spectral function that depends on the total baryon density and temperature of the medium, the two models can be explored while keeping both the total baryon density and temperature near constant and varying the collision energy. In addition, a constant total baryon density and temperature suggests that the emission of e^+e^- pairs may be dependent on the lifetime of the collision. If the variables remain constant, then the lifetime of the collision should be apparent in the total emission of the measured e^+e^- pairs.

To test ρ models, or more importantly, to study ρ production, the difference between the l^+l^- measurements and the sum of l^+l^- from known sources (*i.e.*, hadronic cocktail), not including contributions from the medium and the ρ , is used. The difference, also known as the excess, should contain contributions from the ρ and medium, which models can be compared to. This excess, when corrected for acceptance of the

detector, can also be used to measure the average lifetime of the system [13]. The collection of the data from Au+Au collisions at $\sqrt{s_{NN}} = 27$ GeV will be discussed further in the following Chapter 3.

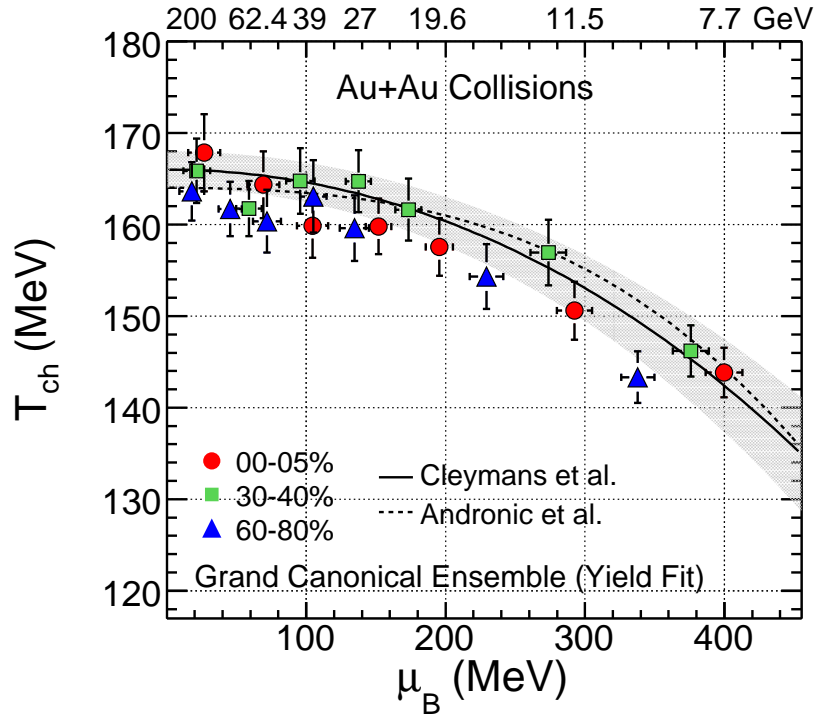


Figure 2.7 : The average chemical freeze-out temperature versus baryon chemical potential (bottom) and collision energy (top). The temperature is extracted from grand canonical ensemble fits to the ratio of particle yields. This figure was taken from [19].

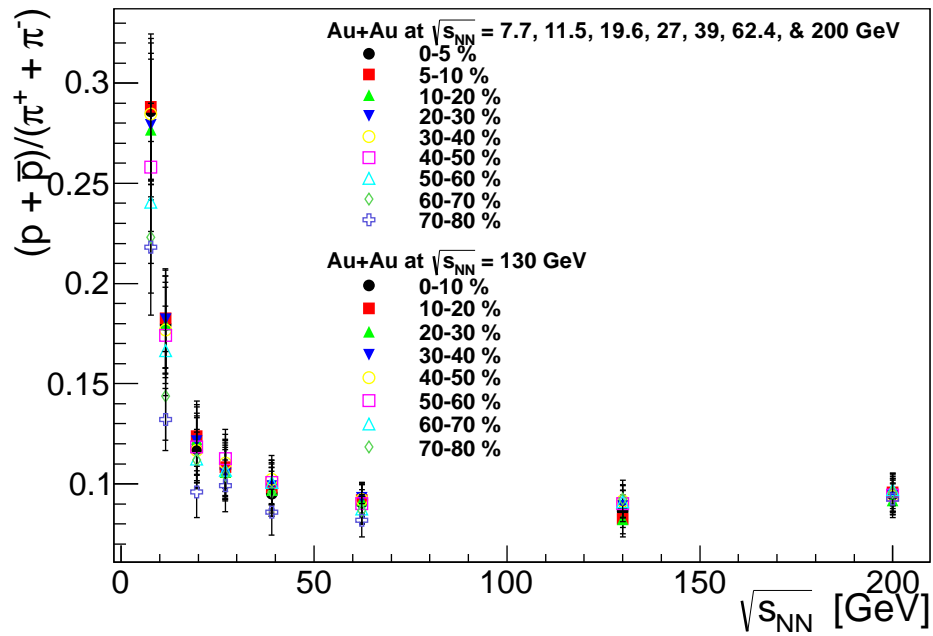


Figure 2.8 : The ratio of protons and anti-protons to π^+ and π^- yields as a function of $\sqrt{s_{NN}}$ for different centralities. These ratios serve as an approximation of the total baryon density. The yields were taken from [19, 20].

Chapter 3

Data Collection

The data analyzed in this thesis is a subset of data collected by the Beam Energy Scan Program (Sec. 1.3), which is a collection of data produced in the years 2010, 2011, and 2014 when RHIC collided Au on Au with a $\sqrt{s_{NN}} = 7.7, 11.5, 14.5, 19.6, 27, 39,$ and 62.4 GeV at the STAR collaboration’s interaction point. The STAR detector was built around their interaction point and used to record data from collisions selected with a minimum-bias towards the type of collision. Each collision recorded is referred to as an “event”. The number of events recorded at each collision energy is listed in Table 3.1. This chapter discusses the facilities and detector used in the collection of the data analyzed and presented in this thesis.

Table 3.1 : The data samples collected by the STAR experiment for the Beam Energy Scan Program.

Species	$\sqrt{s_{NN}}$ (GeV)	Number of Events ($\times 10^6$)
Au+Au	7.7	4
Au+Au	11.5	12
Au+Au	14.5	20
Au+Au	19.6	36
Au+Au	27	70
Au+Au	39	130
Au+Au	62.4	67

3.1 RHIC

The Relativistic Heavy Ion Collider (RHIC) is located at Brookhaven National Laboratory in Upton, New York (shown in Fig. 3.1 as the blue and yellow rings). In order for the gold atoms to reach the RHIC rings and collide, the gold ions must first traverse the accelerator complex (shown in Fig. 3.1). The accelerator complex starts at the Tandem Van de Graaffs where gold ions are produced and transferred (shown as the gold line) at 1 MeV/nucleon over to the Booster synchrotron (shown as the cyan line). The Booster synchrotron then accelerates the ions and transfers the ions at 100 MeV/nucleon to the Alternating Gradient Synchrotron (AGS) (shown as the green line). The AGS accelerates and transfers the ions at 8.9 GeV/nucleon to the RHIC where half of the ions are passed along in the “yellow ring” and the other half travel in the opposite direction in the “blue ring”. Here, the ions are accelerated (or decelerated) to the desired beam energy and then steered to collide at the interaction points. For the Beam Energy Scan Program, the delivery of these collisions proved to be challenging compared to the delivery of Au+Au collisions at $\sqrt{s_{NN}} = 200$ GeV, which the RHIC was initially designed to collide. To overcome this challenge, the collisions were delivered over a 2 meter range along the beam direction at the interaction point. The data and results presented in this thesis were produced in collisions of Au+Au at $\sqrt{s_{NN}} = 27$ GeV, which took place between Tuesday, June 21, 2011 to Tuesday, June 28, 2011.

3.2 STAR

The Solenoidal Tracker At RHIC (STAR) is centered at the 6 o’clock interaction point of the RHIC. The 2011 detector configuration of STAR is shown in Fig. 3.2. STAR is

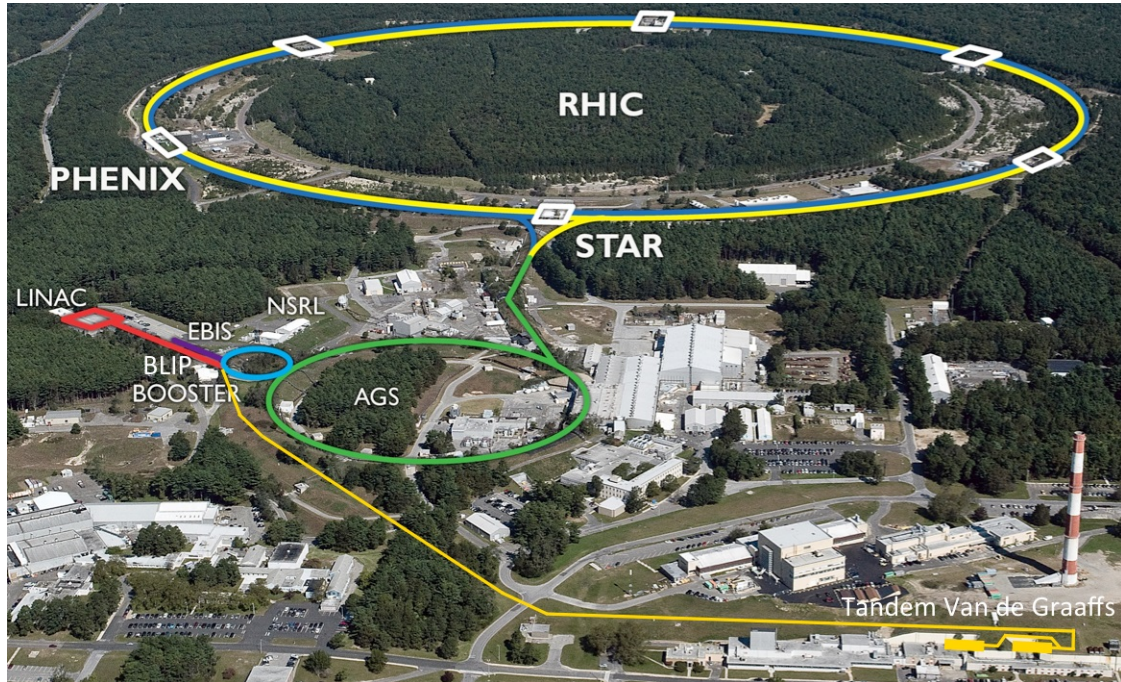


Figure 3.1 : An aerial view of the Relativistic Heavy Ion Collider and the accelerator complex that supplies the gold ions to the RHIC. This figure was taken from [21].

comprised of several subsystems used to record and monitor information during the collisions. STAR has several subsystems used to select (*i.e.*, trigger) which collisions to save. In this analysis, events of interest were triggered with a minimum-bias on the type of event, which was accomplished by requiring a coincidence of signals in the $-z$ and $+z$ components (where \hat{z} is the direction along the beam path) in at least one of the following detectors: the Beam-Beam Counter (BBC), the Vertex Position Detector (VPD), or the Zero Degree Calorimeter (ZDC). For triggered events,

information from the Time Projection Chamber (TPC) and Time of Flight (TOF) subsystems is used to identify the particles.

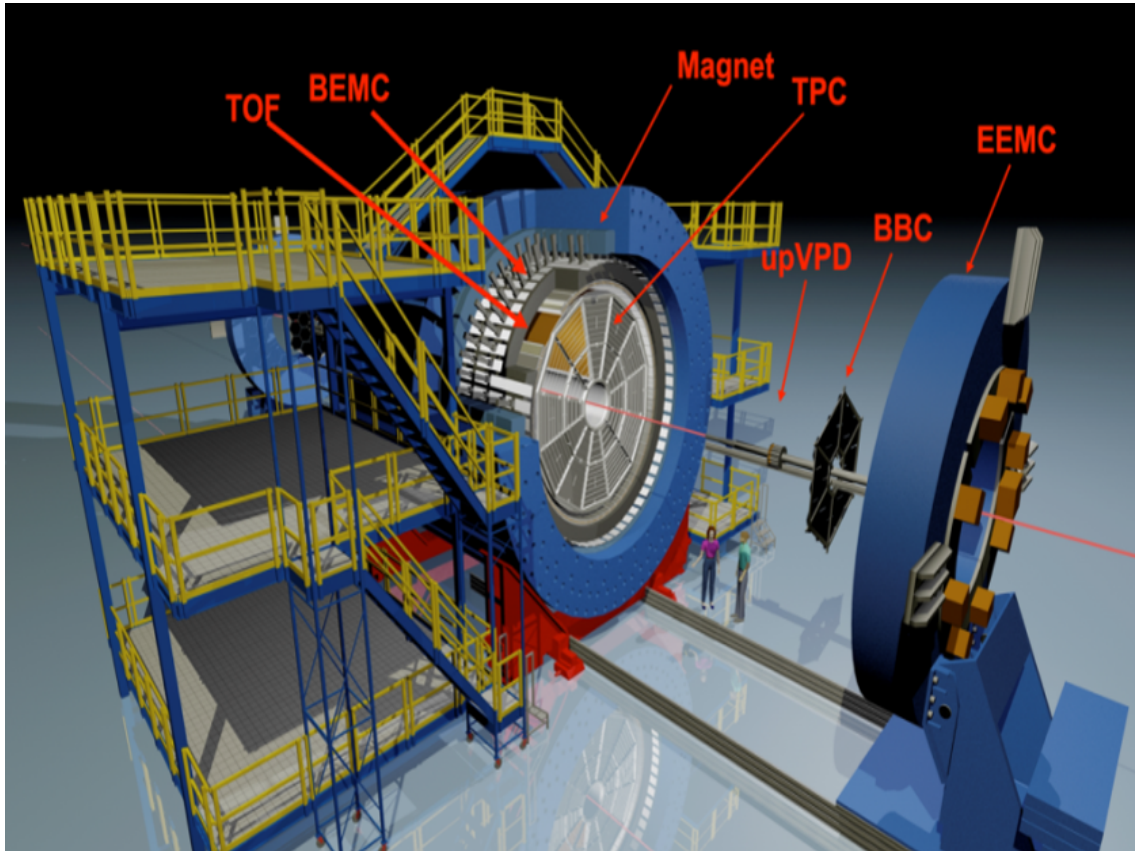


Figure 3.2 : An exploded view of the Solenoidal Tracker At RHIC (STAR), where sections of the detector are missing to illustrate different subsystems such as TOF. When taking data, the BBC and the end-cap electromagnetic calorimeter (EEMC) to the BBC's right are actually positioned directly against the barrel of STAR. This figure was taken from [22].

3.2.1 Trigger Systems

Two Beam-Beam Counters (BBCs) surround the beam pipe, with one situated on the $+z$ side and the other situated on the $-z$ side of STAR, such that the subsystem covers an absolute pseudo-rapidity ($|\eta|$) from 2.1 to 5. The BBC on each side is

comprised of 36 light-tight scintillator panels (the 18 large panels on the outer rings cover $2.1 < |\eta| < 3.3$ and the 18 small panels on the inner rings cover $3.3 < |\eta| < 5$). Each panel is connected to a photomultiplier tube via optical fibers. The panel-to-photomultiplier-tube mapping is shown in Fig. 3.3. A signal is generated in a BBC when a minimum-ionizing particle crosses a scintillator panel producing a scintillation which is then amplified by the photomultiplier tube.

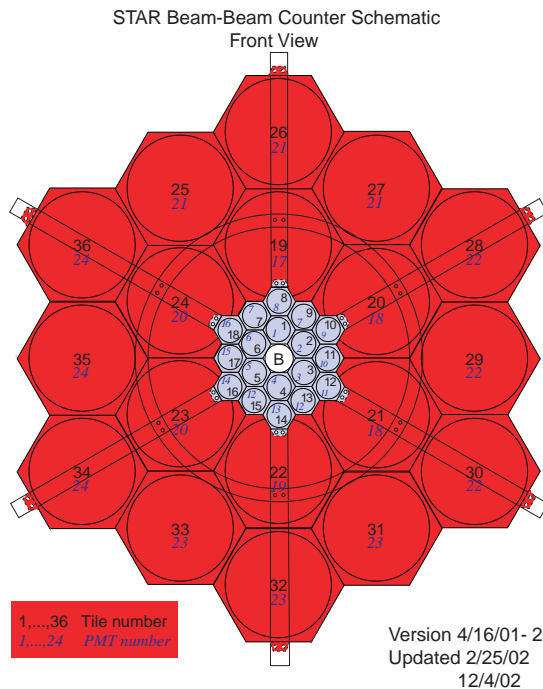


Figure 3.3 : A schematic view of one of the BBCs. This figure was taken from [23].

The Vertex Position Detector (VPD) consists of two components, with one situated on the $+z$ side and the other situated on the $-z$ side of the STAR center (referred to as the “East” and “West” components), such that the subsystem covers an $|\eta|$ -range from 4.24 to 5.1 [24] (the assemblies are shown in Fig. 3.4a). Each com-

ponent of the VPD is an array of 19 individual tubes that surround the beam pipe in two concentric rings as shown in Fig. 3.4b. Each tube consists of a Pb converter, a scintillator, and a close-proximity photomultiplier tube to detect photons from π^0 s. For the data presented in this thesis, the VPD is used only as a detector to aide in the decision if a collision should be saved for analysis (*i.e.*, triggered); however, in other studies and calibrations of the Time of Flight (TOF) system (the TOF system is described in Sec. 3.2.3), the VPD is used as alternative method to verify the z -position of the collision, as determined by the TPC, and to provide a reference time for when the collision started.

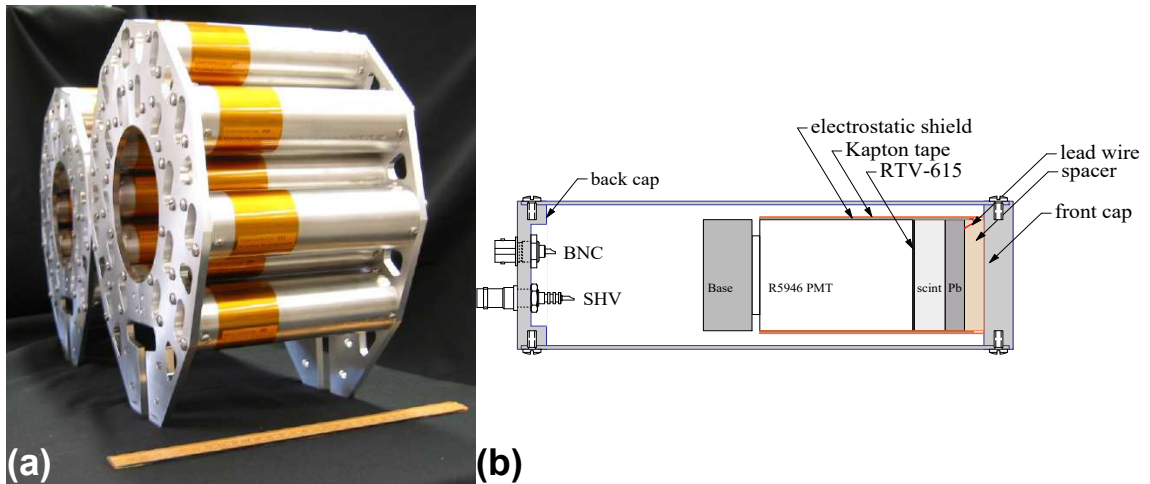


Figure 3.4 : The VPD subsystem. (a) The VPD assemblies. Each assembly is mounted with the beam pipe going through the center. (b) The hollow cylinder of each VPD assembly contains a photomultiplier tube (PMT) with a lead converter in front. This figure was taken from [24].

The Zero Degree Calorimeter (ZDC) [25] is comprised of two components, with one situated on the $+z$ side and the other situated on the $-z$ side of STAR, at about 18 m from the center in each direction. The purpose of the ZDC is to detect neutral beam fragments, which can be used in the minimum-bias selection of events. The

ZDC is located outside of the detector hall, as a consequence, the ZDC is not shown in Fig. 3.2. The calorimeter is designed to stop, and measure the energy deposition of, hadrons. Coming from the interaction point, the ZDC components are located downstream of the dipole steering (DX) magnets in-between the collider rings (shown as the red boxes in Fig. 3.5a). As the charged particles (*i.e.*, protons) first pass through the DX steering magnets, the charged particles are steered away from the ZDC while the neutrons continue forward and are deposited in the ZDC. The energy deposited from stopping the neutron(s) is then translated into a count of how many neutrons have been detected. During ion-on-ion collisions, nucleons (*i.e.*, neutrons and protons) that do not interact inelastically usually continue to travel past the interaction point and down the beam pipe (the DX magnets will steer the protons outside the beam pipe, while the ions that were not collided will be steered to remain inside the beam pipe). So in more peripheral collisions, there are a greater number of neutrons traveling down the beam pipe. This leads to the ZDC having a larger signal, which is why the ZDC is associated with detecting peripheral collisions.

3.2.2 Time Projection Chamber

The Time Projection Chamber (TPC) is the heart of STAR, as shown in Fig. 3.2. Nestled inside of STAR's solenoidal magnet, the TPC tracks the charged particles, measures the momentum of the charged particles, and measures the energy loss (dE/dx) of the charged particles. The TPC consists of a chamber filled with a P10 gas (*i.e.*, 10% methane and 90% argon). A uniform electric field is applied across each half of the chamber and it runs along the beam pipe direction (*i.e.*, the z -axis) from the grounded end caps pointing toward the High Voltage Membrane (a cathode) in the center. The Multi-Wire Proportional Chambers (MWPCs) [111], and readout pads

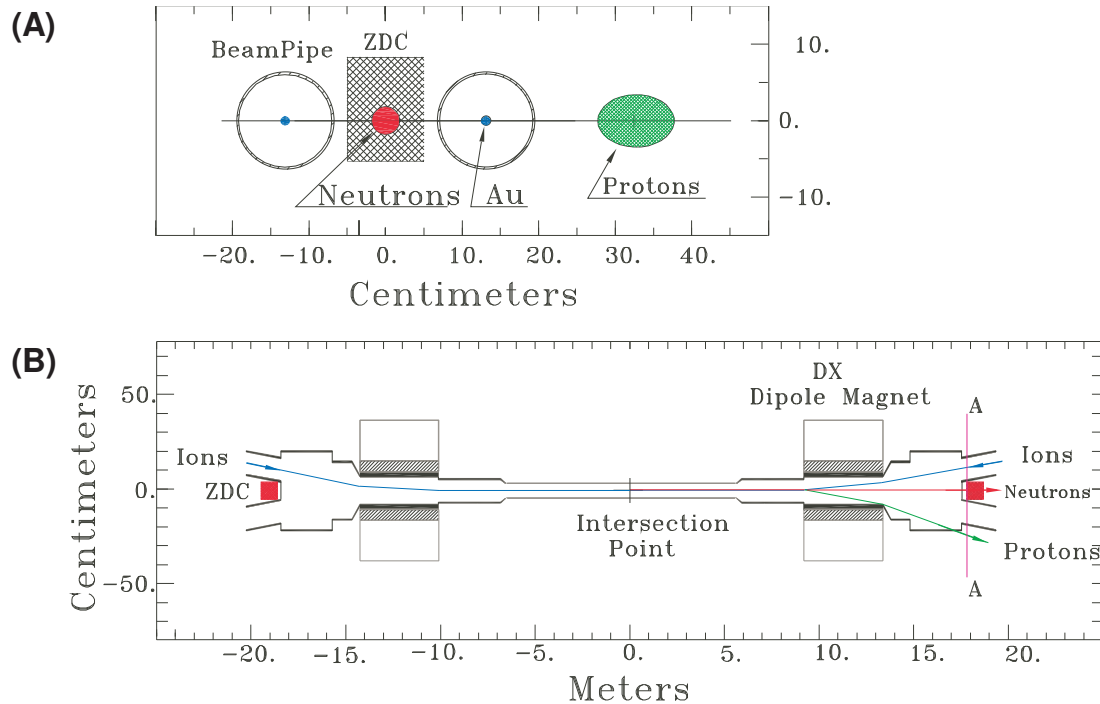


Figure 3.5 : The physical location of the ZDC (the cross-hatched area in (a) and the red box in (b)) with respect to the beam pipes and interaction point (labeled “Intersection Point” in (b)). In this figure, ions are being collided. (a) The $x-y$ plane showing the beam pipes going into/out of the page. (b) The $z-x$ plane showing the beam pipes moving along the width of the page. This figure was taken from [25].

associated with the MWPCs, are located at the end caps of the TPC. The P10 gas is ionized by the charged particles as the particles pass through the gas. Since the electric field in the chamber is uniform, the cations travel toward the center while the anions travel toward the MWPCs. The MWPCs amplify the signal and induce an image charge on the readout pads, which are measured. A plane of readout pads is shown in Fig. 3.7, where the inner plane (closest to the beam pipe) has fewer readout pads than the outer plane.

Particle tracking (*i.e.*, the determination of the path a particle traveled) is performed in two parts. The first part is the reconstruction of where the particle ionized

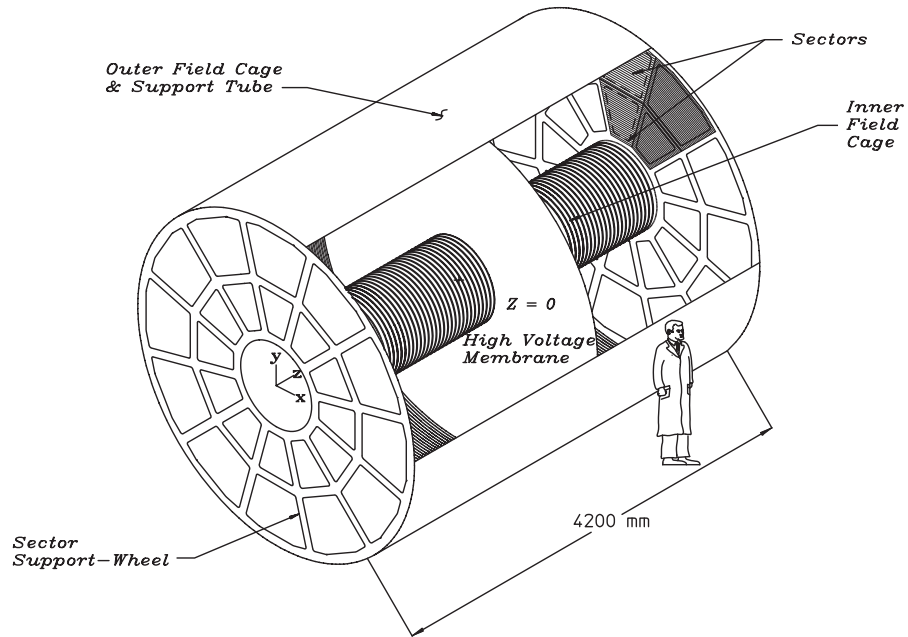


Figure 3.6 : A schematic view of the Time Projection Chamber. This figure was taken from [26].

the gas. The second part is fitting the collection of coordinates (*i.e.*, TPC points or hits) with a helix to form a track. Reconstructing coordinates of the ionized gas is performed in the transverse plane ($x - y$) and in the \hat{z} -direction, separately. Because the electric field and magnetic field in the STAR detector are in-parallel and uniform along the z -axis of the TPC, the transverse position of a particle is approximated by measuring the x - y position of the signal generated on the readout pads. With a uniform electric field, the z -position of the particle is found by dividing the “time taken for the anions (*i.e.*, electrons) to reach the outer membrane” by the “average drift velocity”. After finding the coordinates, the momentum of the particle is determined. The momentum of the particle is calculated via the use of the 0.5 T magnetic

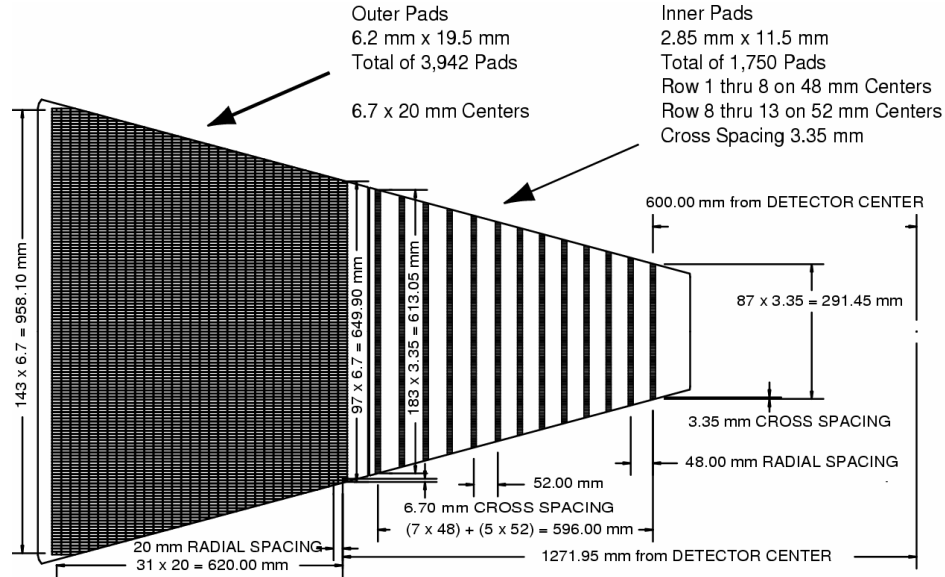


Figure 3.7 : One sector of twelve that make up a TPC endcap. There are two endcaps, so the TPC consists of twenty-four sectors in total. This figure was taken from [26].

field of STAR's solenoidal magnet surrounding the outside of the TPC. The magnetic field runs parallel with the electric field such that the charged particles bend in the transverse plane. In order to determine the transverse momentum (p_T) of a particle, a circle is fitted to the coordinates of the transverse plane to produce a radius, which is used to calculate the p_T . The total momentum of the particle is then found by taking the radius of curvature of the particle and the angle between the particle track and the z -axis. All together, this information gives a helix, or a particle track.

Particle identification is performed by measuring the dE/dx and momentum of each track and comparing them to Bichsel curves [112, 113]. Bichsel curves are the most probable dE/dx for a given particle species in the gas. For more detail on the particle identification used in this analysis refer to Ch. 4.

3.2.3 Time of Flight

The Time of Flight (TOF) system [27] is a collection of multi-resistive plate chambers (MRPCs) positioned around the TPC. The TOF is designed to measure the arrival of charged particles with a precision ≤ 100 ps. These MRPCs are sandwiches constructed of phenolic-impregnated Kraft paper honey comb, PC board, pick-up pads, mylar, electrodes, glass, and fishing line (used to keep the glass plates at a uniform distance) with the physical dimensions of 9.4 cm (w) x 1.95 cm (h) x 21 cm (l), as shown in Fig. 3.8. The TPC is enveloped by 120 MRPC filled trays where 60 of the trays layover like slats on a deck from the middle of the TPC to the endcap and the other 60 trays layover on the other half of the TPC. A single tray is shown in Fig. 3.9 to illustrate their positioning outside the TPC. Each tray is filled with thirty-two MRPCs facing the interaction point (except for four trays, where in each tray, four MRPCs have been removed to accommodate a Gas Electron Multiplier(GEM)-based chamber used to monitor calibrations in the STAR TPC). The orientation of the MRPCs inside a TOF tray are shown in Fig. 3.9.

When the TOF is in operation, a high potential difference is applied across the glass plates of a MRPC with +7000 V through one electrode and -7000 V through the other. This produces a strong electric field in each gas gap between the plates, causing the plates to electrically float. Charged particles traversing through the MRPC ionize the gas (a mixture of 95% Freon R134a and 5% isobutane). Ionization of the gas in the MRPC leads to a series of avalanches that quickly cumulate and generate an electric signal.

The TOF measures the arrival time of the particle (t_f), which is compared to the start time of the collision (t_0), to calculate the particle's time of flight, $\Delta t = t_f - t_0$. The normalized velocity (β) of the particle can be found with the particle's time of

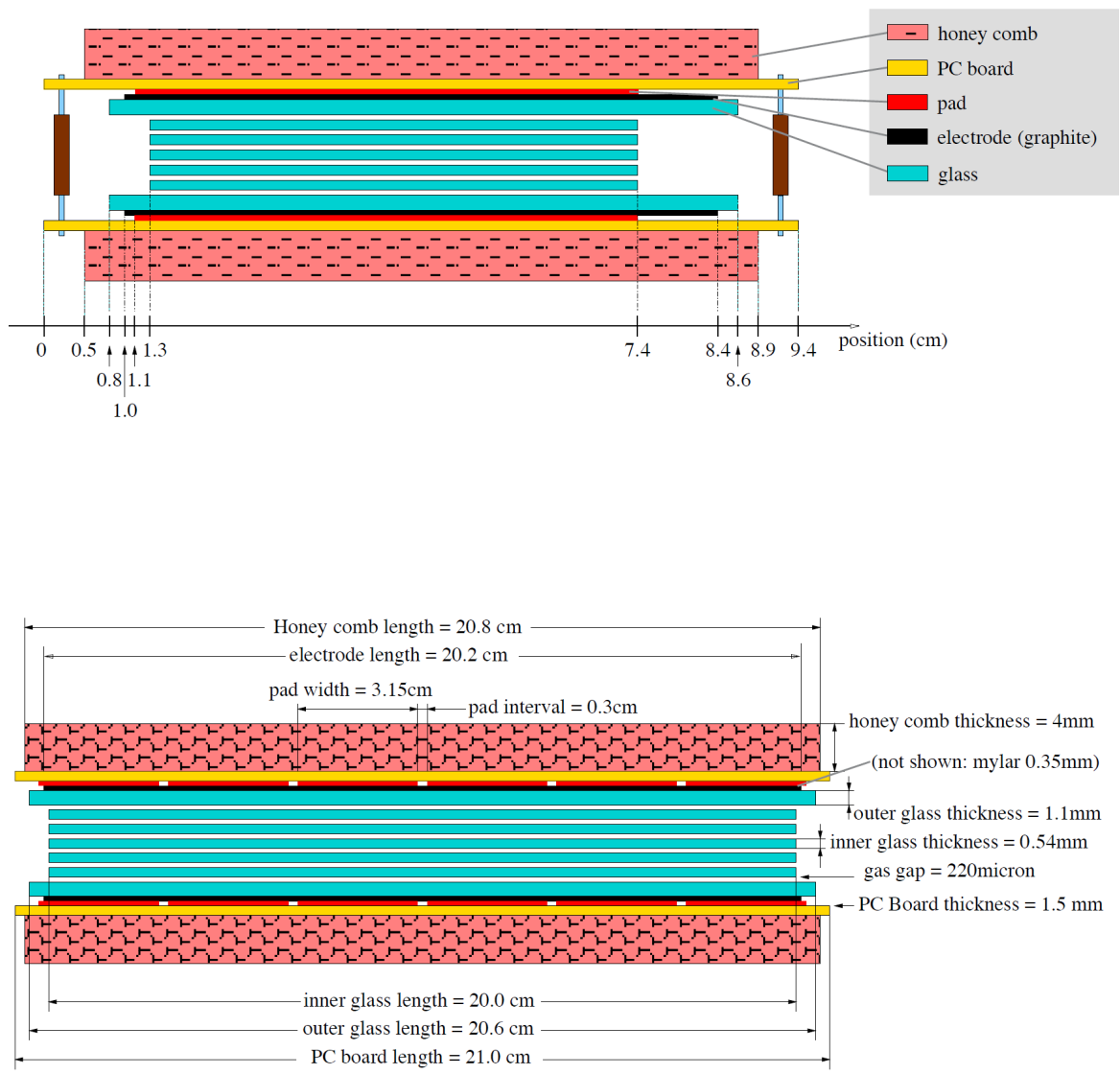


Figure 3.8 : Side views of a TOF multi-resistive plate chamber. (Top) The short edge of an MRPC. The face of this side runs parallel with the beam pipe. (Bottom) The long side. The face of this side runs perpendicular to the beam pipe. This figure was taken from [27].

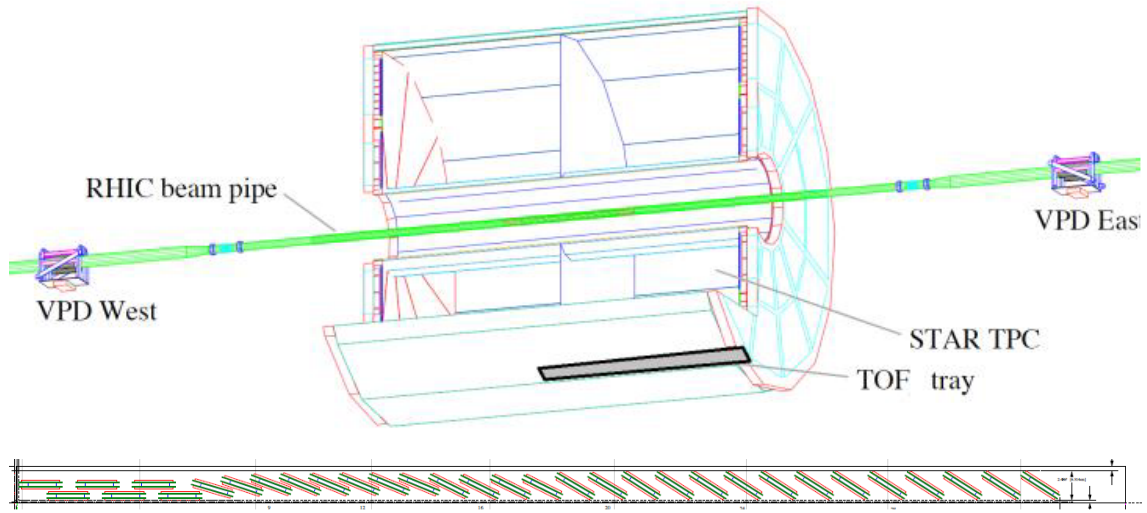


Figure 3.9 : (Top) The positioning of a TOF tray on the outside of the TPC. (Bottom) The orientation of the MRPCs inside of a TOF tray, where the left side is positioned over the center of the TPC. This figure was taken from [28].

flight, which we have with the TOF, and the path length (s) as follows:

$$\beta = v/c = \frac{s}{c\Delta t}, \quad (3.1)$$

where v is velocity and c is the speed of light. The path length is found by associating the signal position (*i.e.*, hit) in the TOF with an extrapolated track from the TPC. In addition to the path length of the particle, the TPC provides the momentum of the particle. When using the inverse normalized velocity (β^{-1}) and momentum of the particle together, the TOF system enables the identification of the particle by its mass. By using the TOF and TPC subsystems together, the kinematic reach of pure electron identification is extended beyond the capabilities of the TPC alone, and this makes an analysis of electrons with low/intermediate momentum possible. The extended identification reach is demonstrated in Ch. 4's Electron Identification section. An example of the β^{-1} as a function of momentum for Au+Au collisions

at $\sqrt{s_{NN}} = 27$ GeV is shown in Fig. 3.10. In this figure, the separation of charged particle species is evident and the dashed lines represent the expected β^{-1} distribution for a given species. The expected β^{-1} is given as

$$\beta^{-1} = \frac{\sqrt{p^2 + m^2}}{p}, \quad (3.2)$$

where p is the momentum and m is particle species mass.

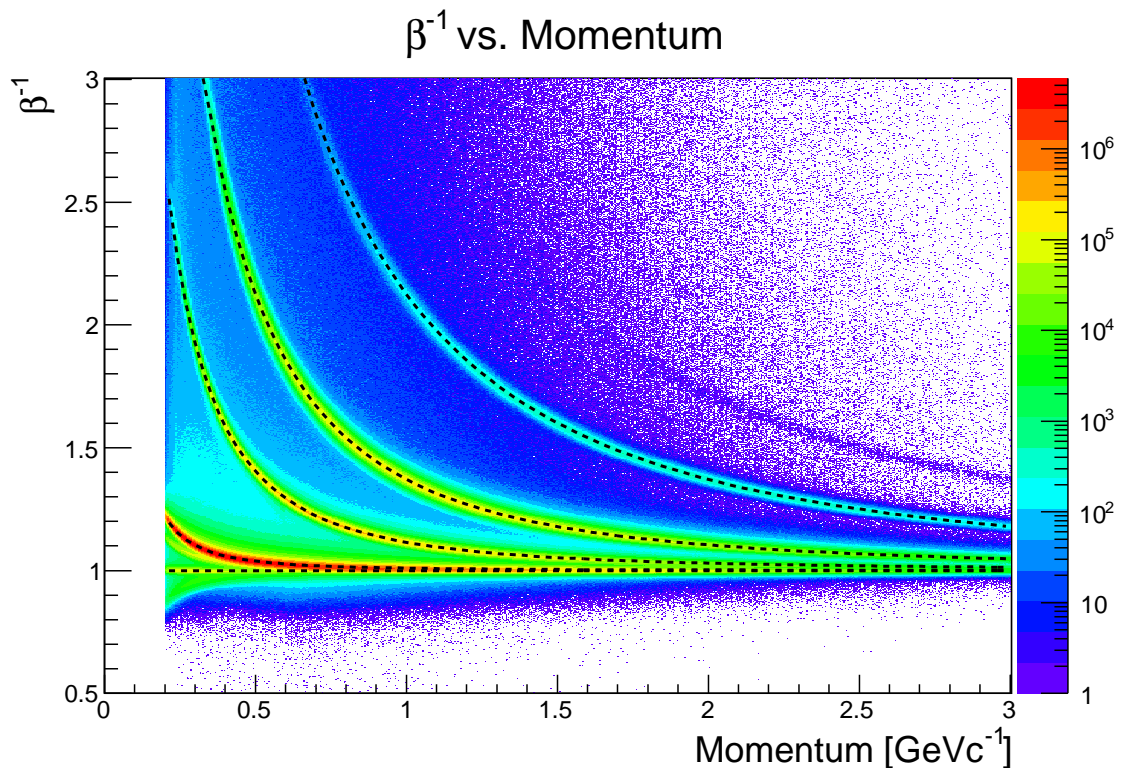


Figure 3.10 : The β^{-1} as a function of momentum for particles from Au+Au collisions at $\sqrt{s_{NN}} = 27$ GeV. The dashed lines represent the expected β^{-1} for a given species. The corresponding species from bottom left to top right: e , π , K, p, and d.

In this thesis, we analyzed the data using a start time that has been determined by the TOF system. The option to determine the start time with the TOF system is referred to as *startless* mode. Typically, the start time is determined through the use

of the VPD; however, for Au+Au collisions at the beam collision energies of $\sqrt{s_{NN}} = 19.6$ and 27, the rapidity distribution of π^0 is narrow compared to π^0 produced in larger collision energies. This leads to an insufficient amount of π^0 with a large enough rapidity to reach the VPD and, thus, to determine the start time efficiently. The *startless* mode takes the average difference between the arrival times of a π sample to determine the start time. The TOF *startless* timing resolution is 60 ps and one π track is required to determine a start time.

As an aside, the TOF, VPD, and Muon Telescope Detector (MTD) (the MTD is not discussed in this thesis) subsystems and other studies that use these subsystems have been supported by my work in various ways. For example, I expanded the TOF calibration corrections from being applied to groupings of 8 pickup pads to a single pickup pad (a pad is shown in Fig. 3.8), determined the offline timing windows used to save raw TOF data with respect to the timing of the collision, calibrated the VPD and TOF systems for the STAR Collaboration's official data production sample at $\sqrt{s_{NN}} = 27$ GeV, and acted as the TOF and VPD slow controls expert during the Au+Au collisions at $\sqrt{s_{NN}} = 27$ GeV. Additionally, a significant amount of my time has been spent on monitoring and repairing EPICS-based slow controls systems for the TOF, VPD, and MTD, and assisting in decoupling the VPD calibrations from the TOF calibrations such that the TOF calibrations may be reused for different beam systems.

Chapter 4

Analysis

This chapter discusses the analysis of the e^+e^- continuum from Au+Au collisions at $\sqrt{s_{NN}} = 27$ GeV. The analysis may be broken up into several parts. These parts are the quality assurance in the selection of good events (Sec. 4.1) and tracks (Sec. 4.2), the particle identification (Sec. 4.3), the generation of an e^+e^- continuum (Sec. 4.4), the determination of the efficiencies in the data selection (Sec. 4.5), and the systematic uncertainties in the analysis' methods (Sec. 4.6). The results corrected for the inefficiencies in data selection are presented in Ch. 6.

4.1 Event Selection

The data analyzed in this thesis was produced in Run 11's Au+Au minimum-bias collisions at $\sqrt{s_{NN}} = 27$ GeV and recorded by STAR on days 172 through 179 with the trigger: "mb1-fast". The mb1-fast is a minimum-bias trigger and the "mb1-fast" version used in this analysis had the trigger ID = 360001. Collisions saved under the mb1-fast trigger were required to have coincidental hits in the $-z$ and $+z$ components of either the VPD, BBC, or ZDC. In this study, to be registered as a viable event, an event must have occurred within the STAR detector while the subsystems were performing well. For an event to have occurred within STAR, an event must have a primary vertex within ± 70 cm of the TPC center along the z -axis and within the beam pipe. The beam pipe has a radius of 2 cm, and hence, the event must have a

primary vertex that has x and y components that satisfy the relation

$$\sqrt{x^2 + y^2} < 2\text{cm}, \quad (4.1)$$

where the transverse plane ($x - y$) is centered at the beam pipe center. An event must also be from a collision with a 0-80% centrality. To select the top 80% most central collisions (*i.e.*, 0-80% centrality), a corrected reference multiplicity of at least 6 has been required. A corrected reference multiplicity refers to the number of good tracks from the collision (*i.e.*, reference multiplicity) that has been corrected for losses from the detector and trigger due to the z -position of the collision. The centrality and corrected reference multiplicity has been provided by the StRefMultCorr package [114]. The StRefMultCorr package is a software package that provides the centrality and corrected reference multiplicity for an event when given the data taking period, z -position of the collision, and the reference multiplicity as input. Each event is also required to have at least one track that satisfies all of the following properties: (1) at least 15 TPC points (a point is a reconstructed position of ionized gas in the TPC) are fitted to form the particle track (out of a possible 45 points), (2) a ratio of fitted TPC points to possible TPC points > 0.52 , (3) a pseudo-rapidity (η) within ± 1 , and (4) $0.2 \leq$ transverse momentum (p_T) $\leq 2.0 \text{ GeV}c^{-1}$. These requirements for a track are imposed to ensure that the event plane for each collision can be calculated, where an event plane is defined by the total momentum of the event in the x and y directions.

In addition, the following events have been excluded from the data sample: events taken during Vernier scans (run numbers: 12174077, 12174085, and 12174086), events with an incorrectly set voltage for one of the TPC inner sectors (run numbers: 12173053-12173057), events recorded when the TOF system was off (run number: 12174096), events when the Barrel ElectroMagnetic Calorimeter (BEMC) was not

included in the data collection (run number: 12177097, the BEMC omission affects the collision centrality definition), and events recorded during time periods that the StRefMultCorr package indicates as bad. The StRefMultCorr evaluation of “good” and “bad” time periods is the result of quality assurance performed by a member(s) of the STAR collaboration during the generation of look-up tables used to correct the reference multiplicity. After satisfying the listed event requirements, 68 million out of 133 million were included in this analysis.

4.2 Track Selection

To ensure that tracks of good quality have been used in this analysis, a track must meet the following requirements:

- At least 15 TPC points are fitted to form a track; This limits the amount of track splitting in the sample. Track splitting is the scenario where small tracks are misidentified and should have been identified as one larger track, but were split into smaller segments instead. By requiring more points in the track, the number of split tracks is reduced.
- A ratio of fitted TPC points to possible TPC points > 0.52 . This limits the amount of track splitting.
- A global Distance of Closest Approach (gDCA) < 1 cm; This limits the amount of particle tracks that originate from photon conversion. gDCA is the distance between the collision vertex and the closest point along a track.
- At least 15 TPC points used in the dE/dx calculation.
- An absolute pseudo-rapidity ($|\eta|$) < 1 ; This is a requirement because the TOF is

used in the particle identification, and the TOF coverage over the TPC extends to $|\eta| < 0.9$ for collisions at the center of the TPC ($z = 0$). A requirement that is imposed based on the kinematic reach of the detector is referred to an acceptance requirement.

- A transverse momentum (p_T) $> 0.2 \text{ GeV}c^{-1}$; This is an acceptance requirement such that charged tracks have enough momentum to reach the TOF subsystem.
- The normalized velocity (β) > 0 ; This requires a TOF signal to be associated with a track in the TPC. (*I.e.*, a particle has left a track in the TPC and a hit in the TOF. The hit has been associated/matched to the TPC track.) There are instances where $\beta = -999$ is used as a flag in the data to indicate an error.
- A TOF signal occurring within $\pm 1.8 \text{ cm}$ of the y coordinate system of a TOF readout pad ($|y_{TOF}| < 1.8 \text{ cm}$); A readout pad is $\sim 3.6 \text{ cm}$ wide as shown in Fig. 3.8.

4.3 Electron Identification

The TPC and TOF systems are used to identify electrons (and positrons) in each event. For a given charged particle, the TPC measures the energy loss (dE/dx), momentum, and electric charge-sign. The measurements can be transformed into a Gaussian quantification of the likelihood that a particle belongs to a specific particle species (*e.g.*, π , K, p, e , ...). The Gaussian quantification ($n\sigma$ or the number of standard deviations from the expected value) is conducted by normalizing the measured dE/dx by the expected dE/dx of the Bichsel function [113, 112] for a given particle

species as follows:

$$n\sigma_{\text{species}} = (R_{dE/dx})^{-1} \log \frac{dE/dx_{\text{Measured}}}{dE/dx_{\text{Bichsel}}}, \quad (4.2)$$

where $(R_{dE/dx})^{-1}$ is the dE/dx resolution.

To improve $n\sigma$ as a particle identifier for electrons, the TOF system is used to remove hadronic contributions in the $n\sigma_e$ measurements. Slow hadrons (*i.e.*, hadrons with $|\beta^{-1} - 1| < 0.03$) are removed in this study to improve the electron purity in the $n\sigma_e$ measurements. To illustrate the improvement, the $n\sigma_e$ as a function of momentum, before and after removing slow hadrons, are shown in Fig. 4.1. On the left, the $n\sigma_e$ distribution is shown for all quality tracks (before the slow hadron rejection). At $n\sigma_e \sim 0$, there are hints of an electron band. On the right, slower hadrons have been removed and the $n\sigma_e$ distribution shows an electron band at $n\sigma_e \sim 0$. *

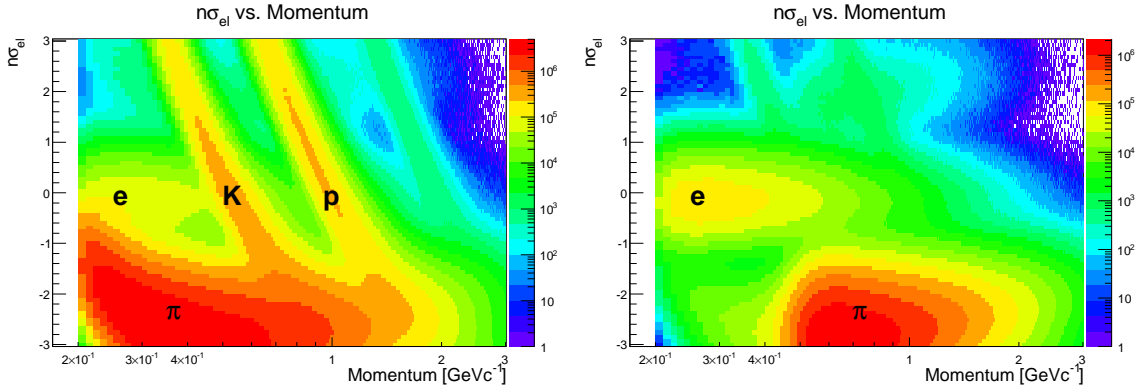


Figure 4.1 : (Left) The $n\sigma_e$ vs. momentum distribution for all quality tracks. (Right) The $n\sigma_e$ vs. momentum distribution for all quality tracks after rejecting the slow hadrons using the TOF system.

*The $n\sigma$ calculation for the official P11id production of the Au+Au collisions at $\sqrt{s_{NN}} = 27$ GeV data sample were $\sim \frac{1}{2}$ the actual $n\sigma$ value.

To select a sample consisting of $>99\%$ electrons (*i.e.*, a “pure electron sample”), the following requirements are imposed on the tracks:

$$\begin{aligned} n\sigma_e &< -0.687342 \times p + 2.1, \\ n\sigma_e &> -0.663252, \text{ when } p \geq 0.637 \text{ GeVc}^{-1}, \\ n\sigma_e &> 1.604 \times p - 1.685, \text{ when } p < 0.637 \text{ GeVc}^{-1}, \end{aligned}$$

where p is momentum and has units of GeVc^{-1} .

4.3.1 Purity

To estimate the purity of the electron (and positron) sample, a multi-Gaussian fit is performed on $n\sigma_e$ for different momentum ranges, where each Gaussian curve represents a different particle species (*i.e.*, e , π , p , K , and $\pi\pi$ — $\pi\pi$ is not actually a particle species, but rather a symbol to explain that a single track is the result of two π that have been merged together by the tracking algorithm). The area under each Gaussian curve is used to count the number of each species (N_x) and together with the sum of each species, the electron purity (P_e) is given by

$$P_e = \frac{N_e}{N_e + N_\pi + N_p + N_K + N_{\pi\pi}}. \quad (4.3)$$

Very pure samples of each species are fitted with Gaussian curves to fix the mean and width of their respective Gaussian curve in the multi-Gaussian fit on $n\sigma_e$. The pure samples of π , K , and p are made by using the same quality track requirements outlined in Sec. 4.2 with a particle identification criteria of $|n\sigma_x| < 0.5$, where $x = \pi$, K , or p , and $|\beta^{-1} - \beta_{expected}^{-1}| < 0.03$, where $\beta_{expected}$ is the expected velocity for a given species. Since there is no $\pi\pi$, the $\pi\pi$ Gaussian mean and width in each momentum

range are constrained by fitting the $\pi\pi$ contamination around $n\sigma_e = 2$ for tracks with $|n\sigma_\pi| > 3$ as shown in Fig. 4.2.

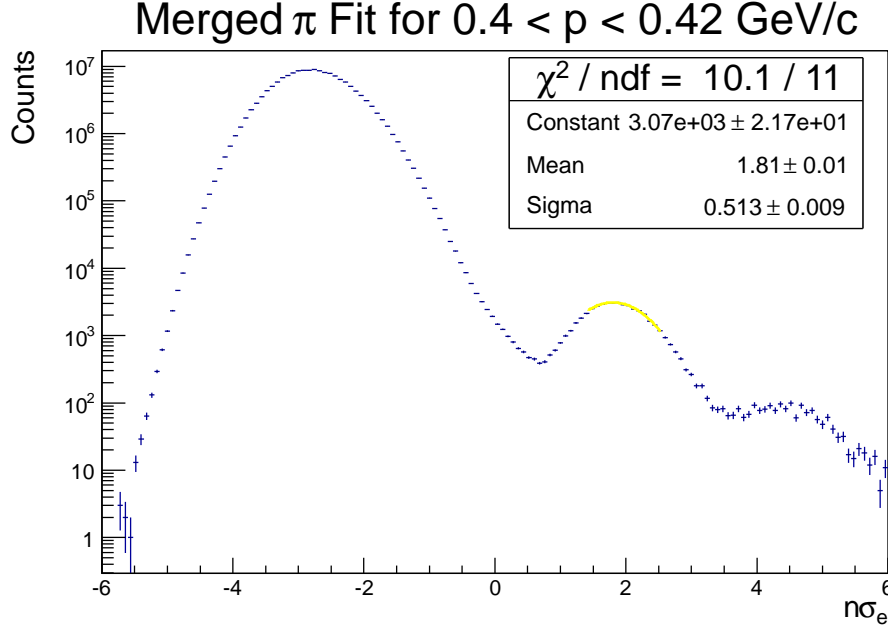


Figure 4.2 : The $n\sigma_e$ distribution for quality tracks with a $n\sigma_\pi > 3$ in momentum (p) slice of 0.4 to 0.42 GeVc^{-1} . The yellow curve at $n\sigma_e \sim 2$ is the fit to the $\pi\pi$ peak, where the mean and width are used in the multi-Gaussian fit for the corresponding $\pi\pi$ Gaussian.

The electrons in the very pure electron sample are selected from photon conversions and π^0 decays. To select the electrons, e^+e^- pairs are reconstructed from a list of electron candidates in each event that follow the same quality track requirements (refer to Sec. 4.2) and have a $|n\sigma_e| < 0.5$. A e^+e^- pair is formed when the two electrons have a distance of closest approach between each other ≤ 0.5 cm, and each e^+e^- pair must have an opening angle $\leq 0.1 \pi$, an invariant mass $\leq 5 \text{ MeVc}^{-2}$, and a $\phi_v < 0.5$, where ϕ_v is the angle between the reconstructed opening angle orientation of the e^+e^- pair (\hat{w}) and the orientation of the opening angle if the e^+e^- pair originated

from photon conversion (\hat{w}_c), as given by

$$\phi_v = a \cos(\hat{w} \cdot \hat{w}_c). \quad (4.4)$$

The orientation of the opening angle of the e^+e^- pair is

$$\hat{w} = \hat{u} \times \hat{v}, \quad (4.5)$$

where \hat{u} is a unit vector in the e^+e^- pair's direction and \hat{v} is a unit vector in the direction perpendicular to the pair's plane, given by

$$\begin{aligned} \hat{u} &= \frac{\vec{p}_+ + \vec{p}_-}{|\vec{p}_+ + \vec{p}_-|}, \\ \hat{v} &= \vec{p}_+ \times \vec{p}_-, \end{aligned} \quad (4.6)$$

where \vec{p}_+ and \vec{p}_- represent the three-momentum vector of the positron and electron, respectively. The orientation of the opening angle if the e^+e^- pair originated from photon conversion is

$$\hat{w}_c = \hat{u} \times \hat{z}, \quad (4.7)$$

where \hat{z} is the magnetic field direction. Pairs originating from photon conversion have an opening angle of 0, such that the pairs will only bend azimuthally (*i.e.*, bend in the transverse plane) by the magnetic field. Pairs from hadrons (*e.g.*, π^0) do have a finite opening angle and hence will not have a preferred orientation of their decay plane. This characteristic allows us to select (or reject) electrons originating from photonic conversions.

In the cases where there is an overlap between particle species as a function of $n\sigma$ for a given momentum range, an exponential extrapolation of the yields ($e^{A \cdot p+B}$) as a function of momentum is used to constrain the amplitude. This is motivated by studying the bands of yield to the sides of the overlap region. The extrapolations

used for e , K , and p are shown in Figs. 4.3 and 4.4. Alternative extrapolations were performed by fitting different momentum ranges and these alternative extrapolations were compared to the extrapolations presented in Figs. 4.3 and 4.4 for the assessment of systematic uncertainty. Please refer to Sec. 4.6.3 for a discussion on the systematic uncertainty.

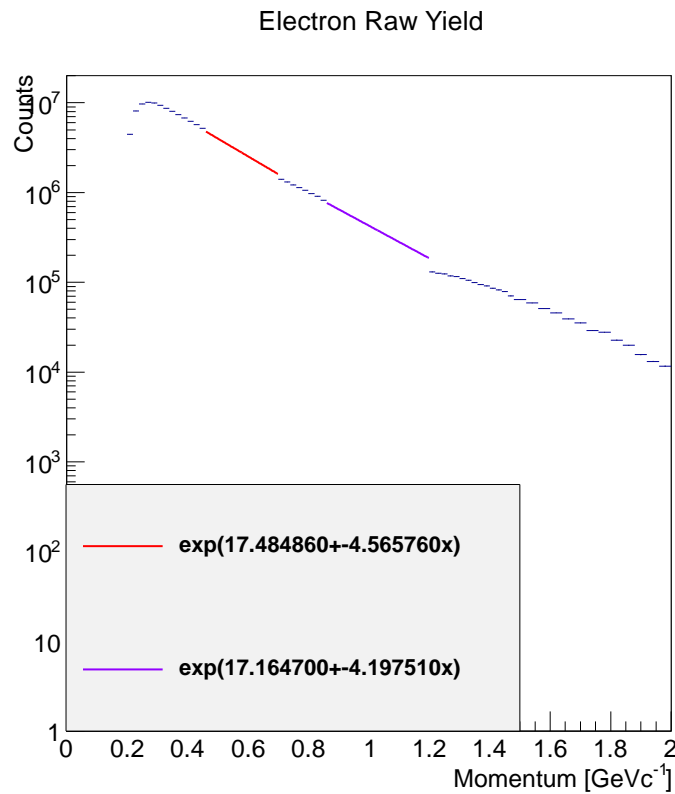


Figure 4.3 : The raw yield counts for electrons as a function of momentum. The red and blue lines are the exponential extrapolations used to estimate the yield.

The electron purity as a function of momentum is shown in Fig. 4.5. The average purity of the electron sample for electrons with a momentum in the range of 0.2 to 2.0 GeVc⁻¹ is $94.5 \pm 0.02 \pm 0.7\%$, where the uncertainty is the statistical and systematic uncertainty, respectively.

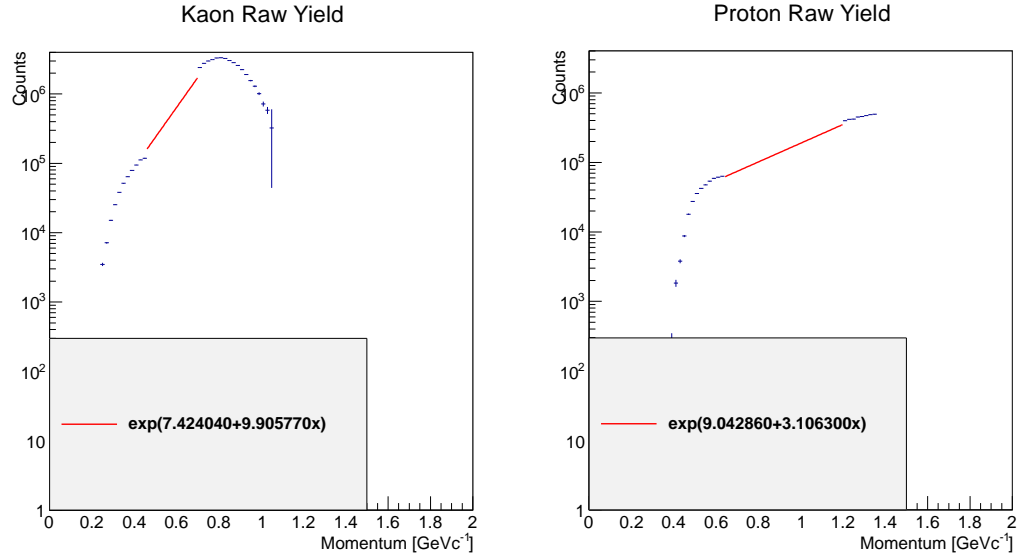


Figure 4.4 : (Left) The raw yield counts for kaons as a function of momentum. The red line is the exponential extrapolation used to estimate the yield. (Right) The raw yield counts for protons as a function of momentum. The red line is the exponential extrapolation used to estimate the yield.

4.4 e^+e^- Continuum

From the sample of identified electrons, e^+e^- pairs are formed. The reconstructed e^+e^- pairs contain pairs from both physical and unphysical sources. The unphysical sources are all considered background and include combinatorial pairs, pairs with hadron contamination, and correlated pairs. Combinatorial pairs are formed by pairing electrons and positrons from uncorrelated sources such as an electron from the decay $\gamma \rightarrow e^-e^+$ and a positron from the decay $\pi^0 \rightarrow \gamma e^-e^+$. Pairs with hadron contamination are formed by pairing together a hadron misidentified as an electron (positron) with either a positron (electron) or another misidentified hadron of opposite electric charge. Correlated pairs are electron pairs formed from the same sources, but not the same signal. Examples of correlated pairs include pairs from double-Dalitz decays

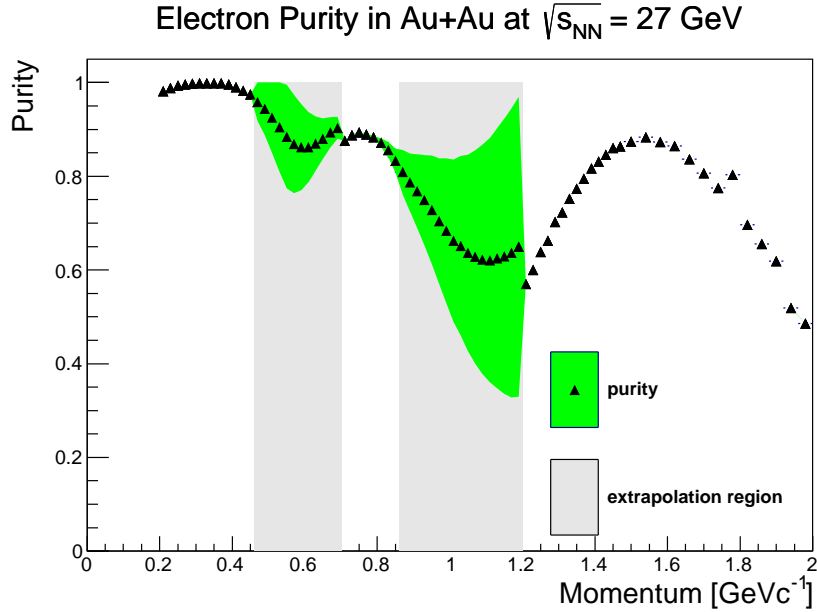


Figure 4.5 : The electron purity as a function of momentum. The green region represents the systematic uncertainty of the purity derived from varying yield extrapolations. The gray shaded region represents the region where the yield totals have been extrapolated by exponential functions.

($\pi^0 \rightarrow \gamma\gamma \rightarrow e^+e^-e^+e^-$) and jets, where in a double-Dalitz decay the paired electrons are from separate γ s. The physical sources include electron pairs produced in the Au+Au collision (*i.e.*, our signal) and electron pairs originating from γ -conversion within detector materials (*i.e.*, γ -conversion electron pairs). The γ -conversion electron pairs are considered background and have a very low invariant mass because the electron pair is produced on detector material, but are reconstructed such that the origin of the electron pair is the collision vertex instead of the detector material. The displacement of the electron pair origin results in an increased opening angle (from 0), which increases its effective invariant mass from approximately 0 $\text{GeV}c^{-2}$.

To remove γ -conversion electron pairs, low invariant mass pairs are selected such

that:

$$\begin{aligned}
 M_{ee} &> -0.2199 \cdot \phi_v + 0.1132, \\
 M_{ee} &> -0.0324 \cdot \phi_v + 0.0357.
 \end{aligned}
 \tag{4.8}$$

Figure 4.6 shows the invariant mass of an electron pair as a function of ϕ_v , where the selection criteria imposed in Eq. 4.8 is the red line and conversion pairs from the beam pipe and inner field cage of the TPC are pointed out in the lower left-hand corner.

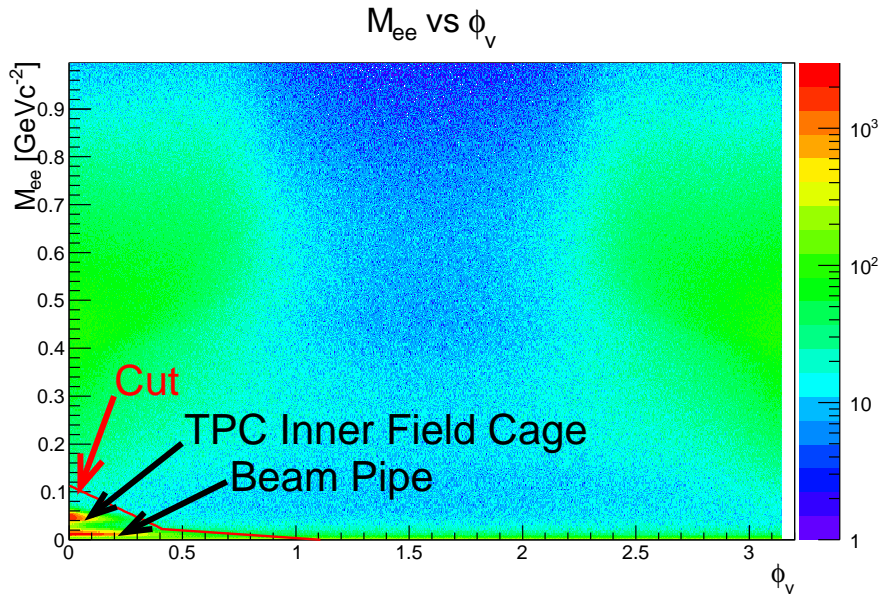


Figure 4.6 : Invariant mass as a function of ϕ_v .

To estimate the correlated and combinatorial backgrounds (BG), a geometric mean, which has been corrected for different charge acceptances, is used

$$\text{BG} = 2\sqrt{N_{++}N_{--}} \frac{ME_{+-}}{2\sqrt{ME_{--}ME_{++}}}.
 \tag{4.9}$$

The BG is estimated with a geometric mean of the like-sign pairs (e^+e^+ and e^-e^-) because e^- and e^+ are only generated in pairs and predominately from independent sources, where this conclusion has been derived in [115]. In Eq. 4.9, N_{--} and N_{++} are the e^-e^- and e^+e^+ pair counts within the same event and ME_{--} , ME_{++} , and ME_{+-} are the e^-e^- , e^+e^+ , and e^+e^- pair counts from pairs that have been formed with electrons from different events. The charge-acceptance correction factor is needed because while the detector is hermetic, the detector is not perfect—there are non-fiducial regions in the detector. Since electrons and positrons bend in opposite directions in the magnetic field, pairs of the same charge have a different acceptance than the pairs of the unlike charges. This is why the ratio of unlike-sign pairs to like-sign pairs have been used as a correction factor (*c.f.* = $\frac{ME_{+-}}{2\sqrt{ME_{--}ME_{++}}}$). Mixed events are used to ensure that the pairs are uncorrelated, and the events that are mixed are required to have similar event properties (*i.e.*, belong to the same event class).

The three properties used to distinguish different event classes are the z position of the primary vertex (V_z), centrality, and event plane angle. Since collisions are delivered with a relatively flat V_z distribution across the STAR detector, events are divided into 25 equi-distance dV_z pools, 12 event pools based on the event plane angle (Ψ_2 , see Eq. 4.10), and 16 event pools based on centrality (*i.e.*, 0 to 80% centrality grouped into pools by 5% increments). Therefore, there are $25 \times 12 \times 16 = 4800$ event pools used for mixing tracks from different events.

The primary vertex position and centrality class definitions are event-level characteristics and provided by the data sample without any additional calculations; however, Ψ_2 definitions was not readily available and needed to be measured. The

Ψ_2 [116] is measured by following:

$$\begin{aligned}\Psi_2 &= \text{ATan2}(Q_x, Q_y)/2, \\ Q_x &= \sum_{tracks} \hat{Q}_x = \sum_{tracks} p_T \cos 2\phi, \\ Q_y &= \sum_{tracks} \hat{Q}_y = \sum_{tracks} p_T \sin 2\phi,\end{aligned}\tag{4.10}$$

where Q_x and Q_y are the total momentum of the event in the x and y directions and \hat{Q}_x and \hat{Q}_y is the momentum in the x and y directions for a given particle track. In order to remove anisotropies caused by the detector acceptance, Q_x and Q_y have been re-centered (*i.e.*, set to (0,0)) to flatten the event plane distribution. To further flatten the event plane distribution, a shifting method has been employed based on this paper [116]. (The event plane angle is expected to be isotropic over a large number of collisions and by flattening the distribution, the distribution becomes more isotropic.) Re-centering Q_x and Q_y is conducted on an event-by-event basis, in which each \hat{Q} is corrected by the mean value $\langle \hat{Q} \rangle$, as follows:

$$\text{Corrected } Q_x = Q_x - N_{tracks} \cdot \langle \hat{Q} \rangle.\tag{4.11}$$

We found that $\langle \hat{Q}_x \rangle = 0.00116153$ and $\langle \hat{Q}_y \rangle = 0.0060679$.

After re-centering Q_x and Q_y , Ψ_2 is flattened more to reduce any remaining acceptance correlations. To flatten Ψ_2 , Ψ_2 is corrected ($\Psi_2 - \Delta\Psi_2$) on an event-by-event basis, where $\Delta\Psi_2$ is given by

$$\begin{aligned}\Delta\Psi_2 &= \frac{1}{2}(2\langle \cos 2\Psi_2 \rangle \sin 2\Psi_2 - 2\langle \sin 2\Psi_2 \rangle \cos 2\Psi_2 \\ &\quad + \sin 4\Psi_2 \langle \cos 4\Psi_2 \rangle - \langle \sin 4\Psi_2 \rangle \cos 4\Psi_2).\end{aligned}\tag{4.12}$$

In Eq. 4.12, the parameters $\langle \cos 2\Psi_2 \rangle$, $\langle \sin 2\Psi_2 \rangle$, $\langle \cos 4\Psi_2 \rangle$, and $\langle \sin 4\Psi_2 \rangle$ are found

by fitting the Ψ_2 distribution, after re-centering Q_x and Q_y , with

$$P(\Psi_2) \sim 1 + 2\langle \cos 2\Psi_2 \rangle \cos 2\Psi_2 + 2\langle \sin 2\Psi_2 \rangle \sin \Psi_2 + 2\langle \cos 4\Psi_2 \rangle \cos 4\Psi_2 + 2\langle \sin 4\Psi_2 \rangle \sin 4\Psi_2, \quad (4.13)$$

for which, we found $\langle \cos 2\Psi_2 \rangle = -2.74700\text{e-}03$, $\langle \sin 2\Psi_2 \rangle = -4.23629\text{e-}03$, $\langle \cos 4\Psi_2 \rangle = 6.59813\text{e-}04$, and $\langle \sin 4\Psi_2 \rangle = 4.15457\text{e-}03$. These parameters are unique for Au+Au collisions with a 0-80% centrality at $\sqrt{s_{NN}} = 27$ GeV.

To illustrate effect of the re-centering and shifting on Ψ_2 , Fig. 4.7 shows Ψ_2 before all of the corrections (blue), after re-centering (red), and after shifting (pink).

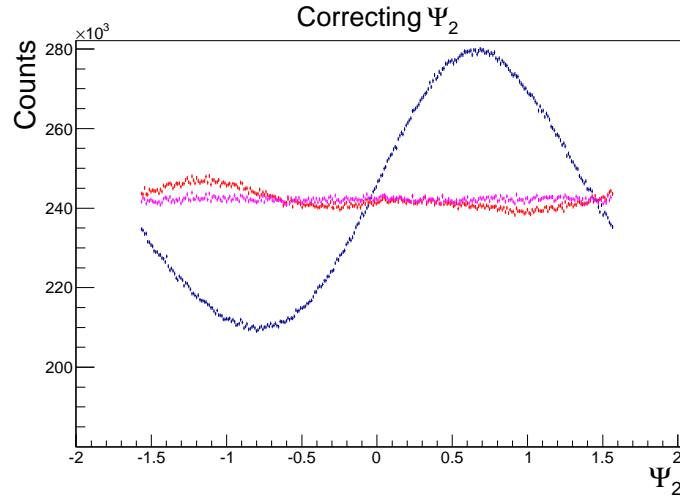


Figure 4.7 : The event plane angle Ψ_2 distribution before any corrections (blue), after re-centering (red), and after shifting (pink). The pink distribution is the event plane angle used for event pooling.

The charge acceptance-corrected background, Eq. 4.9, is subtracted from the e^+e^- continuum (foreground) as a function of invariant mass and pair transverse momentum to give the raw signal. The resulting invariant mass distributions for the foreground, combinatorial and correlated backgrounds, and signal have been normalized

to the number of events and are shown for Au+Au collisions at $\sqrt{s_{NN}} = 27$ GeV in the top panel of Fig. 4.8. The bottom panel of Fig. 4.8 is the ratio of signal to background and demonstrates that an interesting e^+e^- pair occurs once in about every 1000 minimum-bias events, with more prominent resonances such as ω and ϕ occurring at about once in about every 50 events.

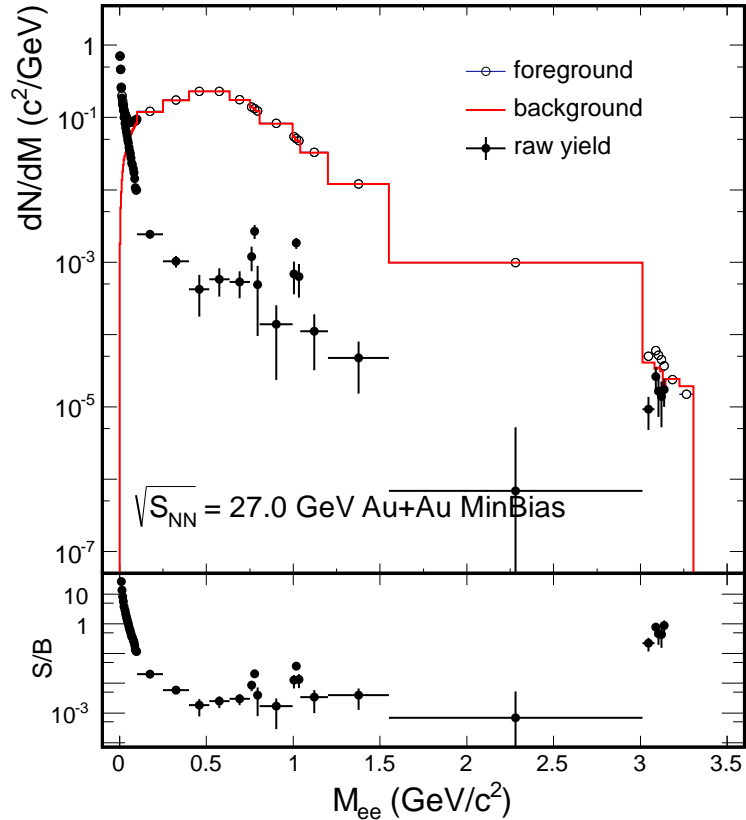


Figure 4.8 : (Top) The raw invariant mass distributions normalized by the number of events for the e^+e^- (open points), correlated and combinatorial backgrounds (red histogram), and the signal (closed points). (Bottom) The ratio of the signal to background invariant mass distributions. The vertical error bars represent the statistical uncertainties and the horizontal error bars represent the bin width.

The hadron contamination remaining in the e^+e^- continuum is approximated in Sec. 4.6.4, and the resulting signal still needs to be corrected for acceptance and

efficiency losses. The acceptance and efficiency loss corrections are covered in the following section, Sec. 4.5.

4.5 Efficiencies

This section discusses the signal losses involved in the e^+e^- measurement and the corrections for those losses. Estimates of the signal losses are broken down into the following categories: tracking, matching, electron identification, and pair formation.

4.5.1 Tracking

Tracking is performed by the TPC. To account for the efficiency in track reconstruction, an embedding technique is used. Embedding is when simulated particles (electrons in our case) are processed through a GEANT v.3 [117] description of the TPC and then the simulated TPC signals are inserted into an actual event. The real and simulated signals of the event are then reconstructed through the same software framework. This allows us to account for the number of tracks before and after reconstruction by being able to know how many simulated tracks existed before reconstruction. To measure the TPC tracking efficiency, the same selection requirements implemented to ensure a quality track (Sec. 4.2) are required of the simulated tracks after reconstruction, except for the TOF related requirements ($\beta > 0$ and $|y_{local}| < 1.8$ cm) as these are related to the TOF efficiencies discussed in the next section (Sec. 4.5.2). Efficiency is defined as the number of simulated tracks reconstructed to the number of tracks simulated, $\epsilon_{\text{tracking}} = \frac{N_{\text{Reco}}}{N_{\text{Sim}}}$.

Simulated electrons (and positrons) are embedded in collisions that occurred with a $|V_z| < 50$ cm and required to be generated from a flat p_T distribution from 0.2 to 4.0 $\text{GeV}c^{-1}$ to ensure enough statistics at higher p_T (the yield of electrons drop

exponentially as a function of p_T), and required to be generated from a flat η distribution between -1.2 to 1.2. The detector acceptance requirements for the tracking of electrons are $p_T > 0.2 \text{ GeVc}^{-1}$ and $|\eta| < 1$, in which the acceptance requirements are applied to both the simulated and reconstructed simulated tracks. The efficiency is found as a function of η , p_T , and ϕ for both electrons and positrons. Electron and positron embedding samples both consist of 200,000 events, where each event was embedded with the number of simulated tracks matching 5% of the total number of tracks in the event. The number of events ensures enough statistics to measure the tracking efficiency as a function of p_T , ϕ , and η . The number of embedded tracks was limited to 5% to prevent additional efficiency losses caused by having too many tracks in the detector.

4.5.2 Matching

Matching efficiency accounts for losses when a TPC track is not properly associated with a TOF signal. To estimate the matching efficiency, the scaled matching efficiency of a charged pion is used in place of the matching efficiency of an electron [38]. The pions are used as a substitute because there is an insufficient number of pure electrons to provide a smooth efficiency distribution across p_T —it is especially important in the low- p_T region, which has the highest yield of electrons. However, there are enough pure electrons to create an electron matching efficiency that will be used in the scaling of the pion matching efficiency. To accomplish the substitution, matching efficiencies are found for both pions and electrons, and then the pion efficiency is scaled to match the electron efficiency as a function of p_T . The matching efficiency ($\epsilon_{\text{matching}}$) is defined as a ratio of the number of tracks associated (*i.e.*, matched) with a TOF signal to

the number of all the tracks in the sample, as given by

$$\epsilon_{\text{matching}} = \frac{N_{\text{TOF}}}{N_{\text{All}}}. \quad (4.14)$$

The samples are pure pions and electrons (with a purity $> 99\%$). All of the tracks in both samples (N_{All}) satisfy the quality track requirements listed in Sec. 4.2 and the pure sample requirements listed in Sec. 4.3.1 sans the β^{-1} requirements. The matched tracks in the sample (N_{TOF}) have a TOF Match Flag > 0 (which means that each track is associated with a TOF signal), a $\beta > 0$, and $|y_{\text{local}}| < 1.8$ cm.

The pure electron sample consists of electrons from both photon conversion and π^0 decays. Because most of the pure electrons originate from photon conversion, the distribution may be distorted between matched and not matched tracks at the edges of η , where there is a larger material budget, which leads to more photon conversion. Hence, the $\frac{d^2N}{d\eta d\phi}$ of the electron sample needs to be corrected to fix the distortion. A pure pion sample is used as a reference for the proper $\frac{d^2N}{d\eta d\phi}$ distribution. The correction to $\frac{d^2N}{d\eta d\phi}$ is conducted in three steps for all tracks in the samples. First, the weights (W) to correct the electron (and positron) distribution as a function of η and ϕ are found as the ratio of charged species such that:

$$W_{\text{Match}}(d\eta, d\phi) = \frac{N_{\pi^+_{\text{Match}}}}{N_{e^+_{\text{Match}}}}. \quad (4.15)$$

Second, the weights are applied to the 3D $(p_T, d\eta, d\phi)$ yield distribution of electrons (h), as follows:

$$h'_{\text{Match}}(p_T, d\eta, d\phi) = W_{\text{Match}}(d\eta, d\phi) \times h_{\text{Match}}(p_T, d\eta, d\phi). \quad (4.16)$$

Third, the corrected distributions are normalized,

$$h''_{\text{Match}}(p_T, d\eta, d\phi) = \frac{N_{\text{Match}}^{\text{BeforeWeight}}}{N_{\text{Match}}^{\text{AfterWeight}}} \times h'_{\text{Match}}(p_T, d\eta, d\phi). \quad (4.17)$$

After correcting the $\frac{d^2 N}{d\eta d\phi}$ of both (matched and all tracks) electron samples, the matching efficiency is determined. The matching efficiency results are shown in Fig. 4.9.

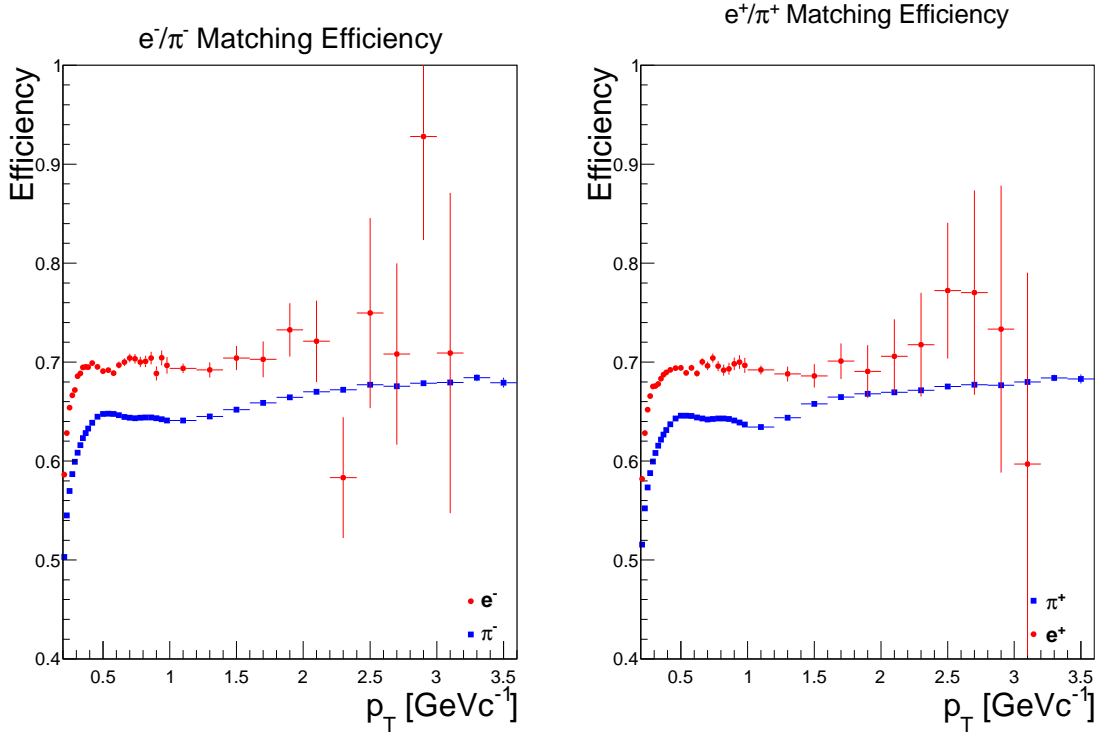


Figure 4.9 : The matching efficiency as a function of p_T for electrons (red dot) and π (blue square). (Left) Negative charge. (Right) Positive charge. The uncertainties are statistical.

To produce the scaled matching efficiency of pions, the π efficiency is multiplied by a functional form ($f(x)$)

$$f(x) = \frac{1}{a + e^{\frac{x-b}{c}}} + d, \quad (4.18)$$

where x is p_T , which describes the matching efficiency of an electron. The parameters for Eq. 4.18 is found by fitting the ratio of the electron matching efficiency to the π matching efficiency shown in Fig. 4.9, where the parameters for the negative charged

species are: $a = 10 \pm 0.9$, $b = 0.163 \pm 0.009$, $c = 0.06074 \pm 0.00349$, and $d = 1.077 \pm 0.002$, and the positive charged species are: $a = 16.71 \pm 1.06$, $b = 0.228 \pm 0.016$, $c = 0.03525 \pm 0.00569$, and $d = 1.079 \pm 0.002$.

4.5.3 Electron Identification

The efficiency of the electron identification process is determined by taking a pure electron sample (same as Sec. 4.3.1) and counting how many electrons are lost after imposing the electron identification criteria (as listed in Sec. 4.3). The efficiency is determined as a function of momentum, regardless of charge, for the β^{-1} and $n\sigma_e$ criteria (Sec. 4.3), separately. The β^{-1} efficiency (ϵ_β) has been determined by counting the number of electrons and positrons that survive the $|\beta^{-1} - 1| < 0.03$ requirement, and this method will be referred to as the counting method. The fraction of electrons after the $n\sigma_e$ requirements represents the $n\sigma_e$ efficiency. The $n\sigma_e$ efficiency ($\epsilon_{n\sigma}$) is determined through a fit method, where the Gaussian fits to the pure electron sample in Sec. 4.3.1 are used to estimate the number of electrons before and after the application of the $n\sigma_e$ requirements as a function of momentum, and this method will be referred to as the fitting method.

The resulting efficiencies are shown in Fig. 4.10, where the β^{-1} efficiencies are shown on the left and the $n\sigma_e$ and electron identification efficiencies are shown on the right. The total electron identification efficiencies ($\epsilon_{eID} = \epsilon_\beta \times \epsilon_{n\sigma}$) are shown for the combination of β^{-1} efficiencies from the counting method and $n\sigma_e$ efficiencies from the fitting method (cyan triangle). The total electron identification efficiencies are also shown for the combination of β^{-1} efficiencies from the counting method and $n\sigma_e$ efficiencies from the counting method (pink triangle). Past e^+ and e^- identification efficiencies, calculated as a function of p_T , ϕ , and η , are also shown (open and closed

squares). The $n\sigma_e$ count method is an alternative method used to calculate the efficiency and as a means to approximate the systematic uncertainty in Sec. 4.6.

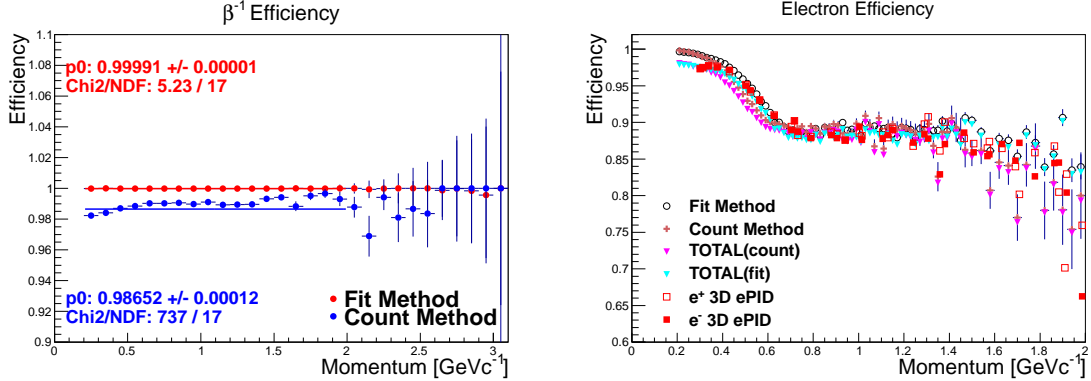


Figure 4.10 : Electron identification efficiencies as a function of momentum. (Left) β^{-1} efficiencies for the count method (blue points) and the fit method (red points). The fit method is used as an alternative calculation for systematic uncertainty approximation and discussed in Sec. 4.6. (Right) The $n\sigma_e$ efficiencies by the fit method (open circles) and count method (brown crosses).

4.5.4 Pair Formation

The efficiency of detecting an e^+e^- pair is found by simulating virtual photons (γ^*) decaying into e^+e^- pairs and reconstructing the electron pairs after the application of the single track efficiencies found from the tracking efficiencies (Sec. 4.5.1), the matching efficiencies (Sec. 4.5.2), and the electron identification efficiencies (Sec. 4.5.3). The steps taken to generate the pair efficiencies are laid out in Fig. 4.11.

Virtual photons (γ^*) are generated according to a flat distribution of center-of-mass energies (W_γ) from 0 to 5 GeVc⁻², a flat distribution of rapidities (Y) from -2 to 2, and a flat distribution of p_T from 0 to 5 GeVc⁻¹. For each event, a single photon is generated by randomly drawing a W_γ , Y , and p_T with a pseudo-random number

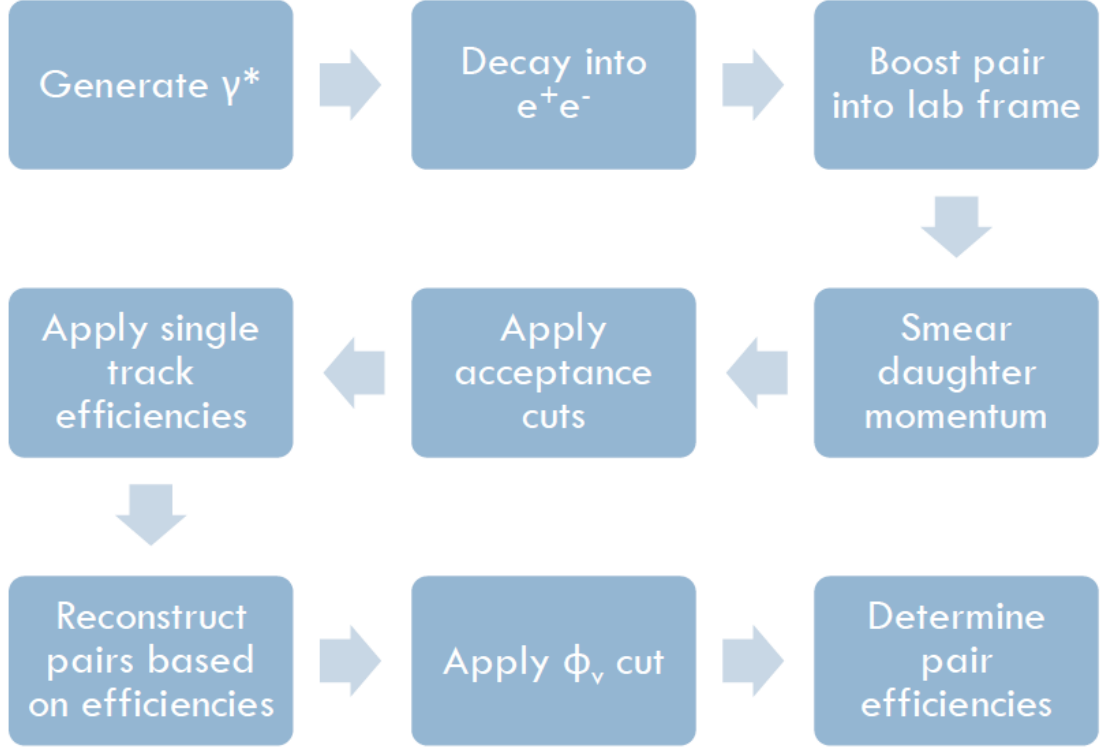


Figure 4.11 : Flowchart for the Monte Carlo virtual photon generator used to create electron pair efficiencies from the single track efficiencies.

generator, Mersenne Twistor [118]. Once the virtual photon is generated, the energy (E) and momentum in the z-direction (p_z) of the system are found via

$$E = \sqrt{W_\gamma^2 + p_T^2} \cosh Y, \quad (4.19)$$

$$p_z = \sqrt{W_\gamma^2 + p_T^2} \sinh Y \quad (4.20)$$

Then momentum in the x-direction (p_x) and y-direction (p_y) are generated with a ϕ randomly drawn from a uniform distribution of 0 to 2π and given by

$$p_x = p_T \cos \phi, \quad (4.21)$$

$$p_y = p_T \sin \phi. \quad (4.22)$$

The virtual photon is decayed into an e^+e^- pair in the center-of-mass frame, where the electron and positron decay back-to-back (*i.e.*, $\vec{p}_- = -\vec{p}_+$). The kinematics of the electron (and positron with the opposite-signed momentum) is randomly drawn from an isotropic ϕ distribution $[0, 2\pi]$ and isotropic $\cos \theta$ distribution $[-1, 1]$ are:

$$p_1 = \sqrt{\frac{W^2}{4} - m_e^2}, \quad (4.23)$$

$$p_{1,x} = p_1 \sin \theta \cos \phi, \quad (4.24)$$

$$p_{1,y} = p_1 \sin \theta \sin \phi, \quad (4.25)$$

$$p_{1,z} = p_1 \cos \theta, \quad (4.26)$$

$$E_1 = \sqrt{m_e^2 + p_{1,x}^2 + p_{1,y}^2 + p_{1,z}^2}, \quad (4.27)$$

where m_e is the mass of an electron.

The daughters of the virtual photon (electron and positron) are boosted into the laboratory frame. The transverse momenta of the daughters are then smeared to simulate the detector momentum resolution, as will be mentioned in Ch. 5. After smearing, the STAR detector acceptance ($p_T^e > 0.2 \text{ GeV}c^{-1}$, $|\eta^e| < 1$, and $|Y_{ee}| < 1$) for reconstructing e^+e^- pairs is applied. The tracks are then reconstructed based on the total single track efficiencies

$$\epsilon_{total} = \epsilon_{tracking} \times \epsilon_{matching} \times \epsilon_{eID}, \quad (4.28)$$

where the total single track efficiency is the product of the tracking efficiency ($\epsilon_{tracking}$), the matching efficiency ($\epsilon_{matching}$), and the electron identification efficiency (ϵ_{eID}) for a given track.

The e^+e^- pair efficiencies are formed by counting the number of pairs that were reconstructed after applying the total single track efficiencies to the number of pairs within the STAR acceptance before the application of the total single track efficiencies.

There is one more requirement applied at the electron pair level that needs to be folded into the pair efficiencies—the ϕ_v requirement, Eq. 4.8. The efficiency of the ϕ_v requirement is estimated through embedding, where π^0 decays have been embedded into real data from Au+Au collisions at $\sqrt{s_{NN}} = 200$ GeV. The efficiency of the ϕ_v requirement, as a function of invariant mass, is shown in Fig. 4.12. To apply the ϕ_v efficiency to the electron pair efficiencies based on single track efficiencies, the efficiencies are multiplied, producing the final electron pair efficiencies that are applied to the raw e^+e^- signal shown in Fig. 4.8.

4.6 Systematic Uncertainties

Systematic uncertainties provide an estimate of the uncertainty on the methods used to measure e^+e^- production. In this study, the systematic uncertainties are evaluated in the following: tracking, matching, electron identification, hadron contamination, and the charge acceptance correction.

4.6.1 Tracking

To evaluate the systematic uncertainty in tracking, a different method than embedding is used to evaluate the tracking efficiency. As described in Sections 4.5.1, 4.5.2, and 4.5.3, three different components of tracking are considered separately for syste-

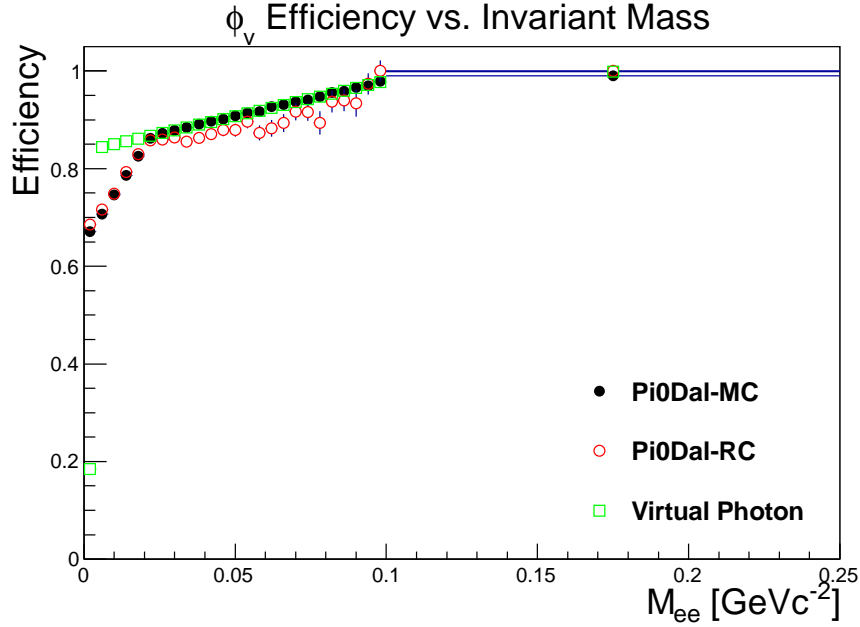


Figure 4.12 : ϕ_v efficiency as a function of invariant mass. The embedding ϕ_v efficiency from π^0 Dalitz decay based on the reconstructed track properties are used as the ϕ_v efficiencies in this analysis (open red points). An alternative embedding ϕ_v efficiency from π^0 Dalitz decays with the simulation values are also shown (solid black circles). Another alternative ϕ_v from the γ^* Monte Carlo are shown for comparison (open green squares).

matic uncertainties; (1) the number of TPC fit points used in tracking, (2) the gDCA requirement, and (3) the number of TPC fit points used in the dE/dx calculation. As an alternative method, the efficiency measurements are performed with data only, instead of embedding simulations into the data. The data consists of a pure electron sample from π^0 decays. The pure sample requires electrons that satisfy π^0 pair requirements and single track properties. The single track properties are as follows: $p_T \geq 0.2 \text{ GeV}c^1$, $|\eta| < 1$, $|n\sigma_e| < 0.5$, and $\text{gDCA} < 3 \text{ cm}$. The π^0 pair requirements are as follows: a perpendicular decay length (*i.e.*, the distance between the primary and secondary vertices in the x - y plane) $\leq 2 \text{ cm}$, $\phi_v \leq \pi$ for the e^+e^- pair, an invariant

mass $\leq 4 \text{ MeVc}^{-2}$ when using global (*i.e.*, no associated primary vertex) track properties, an invariant mass $\leq 5 \text{ MeVc}^{-2}$ when using primary track properties, and a distance of closest approach between the pair helices $\leq 1 \text{ cm}$.

The tracking efficiencies for each of the three tracking categories are the fraction of electrons surviving each constraint as a function of p_T , η , and ϕ for each charge. The tracking efficiencies are integrated over ϕ and η and presented as a function of p_T . These “alternative” tracking efficiencies are compared with the tracking efficiencies that are being used to correct the raw signal, see Sec. 4.5.1.

In Fig. 4.13, for electrons and positrons, we show the differences between the efficiency calculations for the requirements: (1) a track having ≥ 15 TPC points and (2) a ratio of fitted TPC points to possible TPC points > 0.52 . A straight line fit is performed on each difference. The mean of the two fits is the systematic uncertainty, which is 1%.

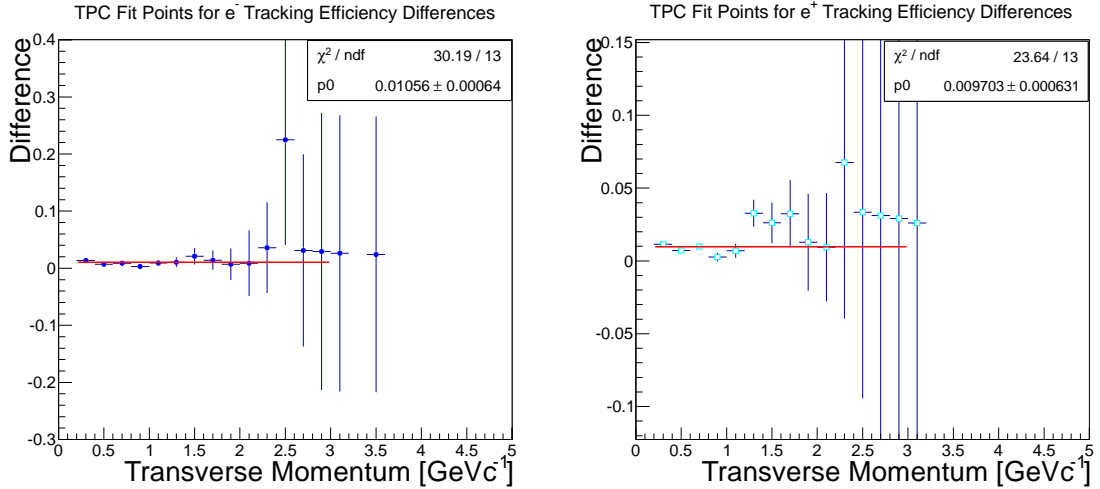


Figure 4.13 : The difference in (TPC fit points for tracking) efficiency calculations between the data and embedding driven methods as a function of transverse momentum. (Left) Electrons. (Right) Positrons. The uncertainties shown are statistical.

The difference between the efficiency calculations for the track requirements of at least 15 TPC points to calculate dE/dx is shown in Fig. 4.14 for electrons and positrons. A straight line fit is performed on each difference. The mean between the two fits is the systematic uncertainty, which is 1.1%.

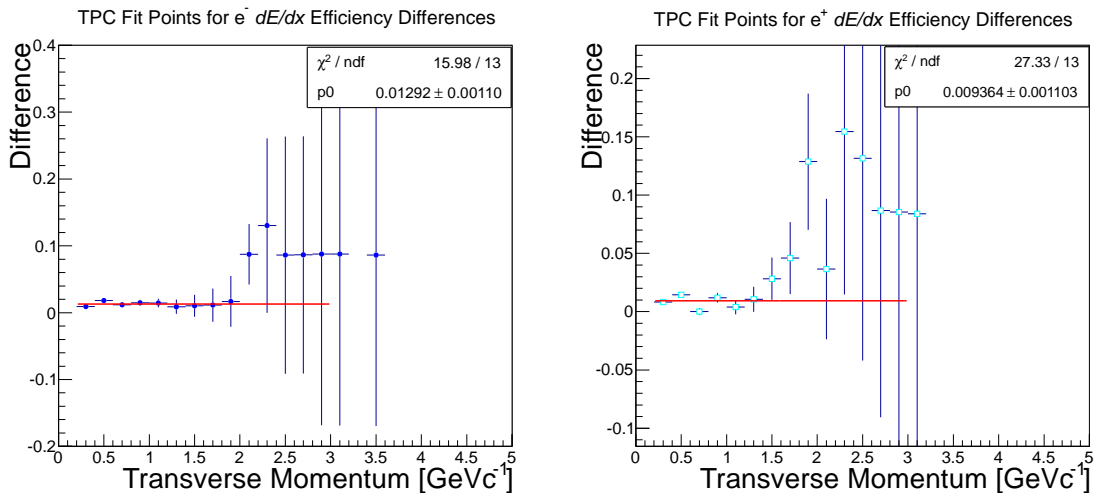


Figure 4.14 : The difference in *TPC fit points for dE/dx* efficiency calculations between the data and embedding driven methods as a function of transverse momentum. (Left) Electrons. (Right) Positrons. The uncertainties shown are statistical.

The difference between the efficiency calculations for the track requirements of $gDCA < 1$ cm is shown in Fig. 4.15 for electrons and positrons. A straight line fit is performed on each difference, and the mean of the two fits is the systematic uncertainty, which is 2.8%.

4.6.2 Matching

The systematic uncertainty in matching a TPC track to a signal in the TOF is estimated by comparing the calculated efficiencies (refer to Sec. 4.5.2) with the efficiencies calculated from a pure electron sample. The pure electron sample is the same sam-

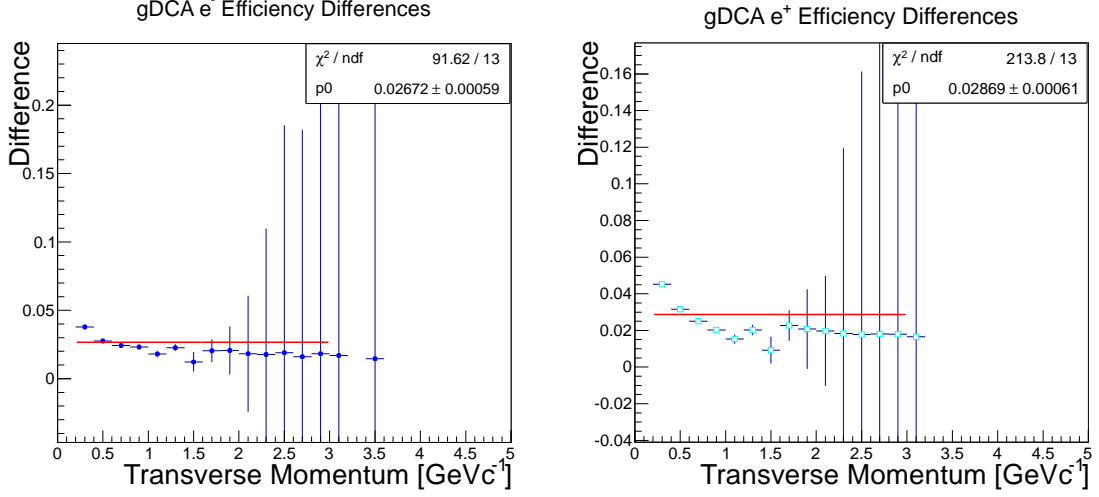


Figure 4.15 : The difference in $gDCA$ efficiency calculations between the data and embedding driven methods as a function of transverse momentum. (Left) Electrons. (Right) Positrons. The uncertainties shown are statistical.

ple that is used as a reference to scale the π matching efficiencies. In Fig. 4.16, the difference between efficiency calculations are shown as a function of transverse momentum. A straight line fit is performed on the difference between efficiencies and the fits are averaged to find an overall systematic uncertainty of 0.53%.

4.6.3 Electron Identification

The systematic uncertainty of the electron identification method is determined by comparing counting method efficiency calculations and fitting method efficiency calculations for both the β^{-1} and $n\sigma_e$ selection requirements.

A counting method is used in the efficiency calculation of the rejecting slow hadrons requirement ($|\beta^{-1} - 1| < 0.03$) that is used to correct the raw signal (as discussed in Sec. 4.5.3). An alternative method is used to compare efficiencies and evaluate the systematic uncertainty and the alternative method is a fit based method. Each β^{-1}

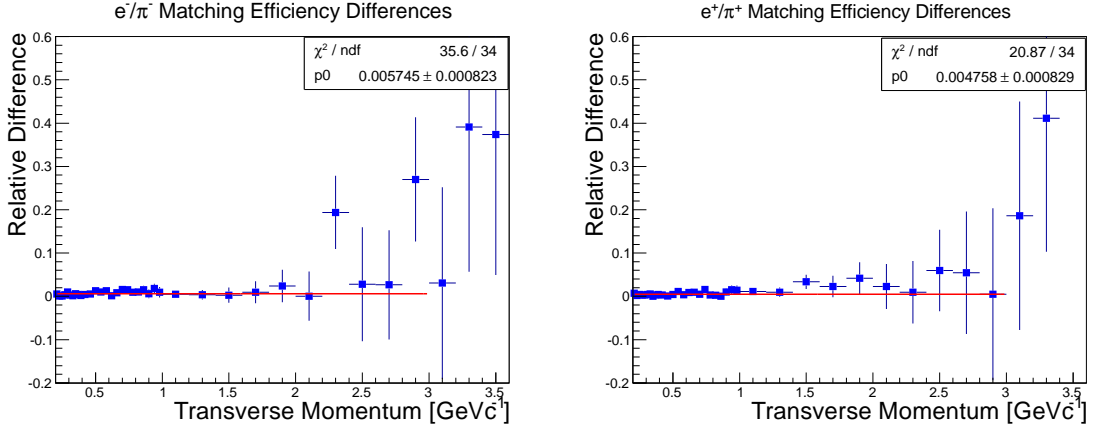


Figure 4.16 : The difference in *matching* efficiency calculations between the scaled π and pure electron methods with respect to the scaled π efficiency as a function of transverse momentum. (Left) Electrons. (Right) Positrons. The uncertainties shown are statistical.

distribution of electrons is fitted to a Gaussian curve across several momentum ranges. To calculate the “slow hadron rejection” efficiency, a ratio of the integrated fits before and after the β^{-1} criteria for different ranges of momentum is performed using:

$$\frac{\text{After}}{\text{Before}} = \frac{\frac{1}{d(\beta^{-1})} \int_{0.97}^{1.03} A \times e^{-0.5((\beta^{-1}-B)/C)^2} d(\beta^{-1})}{\frac{1}{d(\beta^{-1})} \int_{0.8}^{1.1} A \times e^{-0.5((\beta^{-1}-B)/C)^2} d(\beta^{-1})}, \quad (4.29)$$

where the ranges of integration (0.8,1.1) and (0.97,1.03) represent the β^{-1} acceptance regions before and after the selection criteria, respectively.

The resulting “slow hadron rejection” efficiency is shown in Fig. 4.10 on the left as the solid red points. The difference between the two methods is shown in Fig. 4.17. A straight line fit to the differences between the “slow hadron rejection” efficiencies is used to approximate the systematic uncertainty, which is 1.3% and shown in Fig. 4.17.

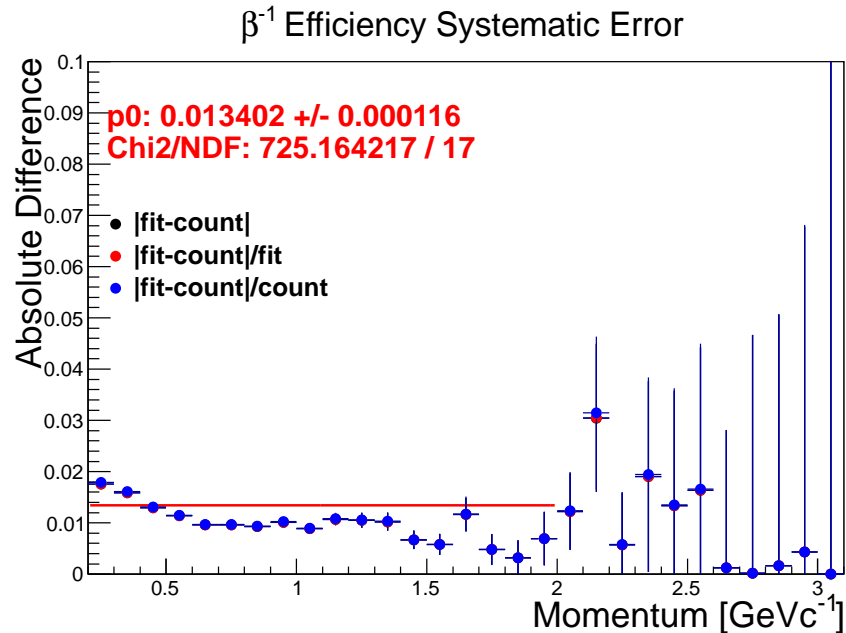


Figure 4.17 : The difference between the fit method and count method “slow hadron rejection” efficiency calculations as a function of momentum. The straight line fit to the difference is used as the systematic uncertainty.

The systematic uncertainty from the $n\sigma_e$ requirements (see Sec. 4.5.3) is estimated by comparing the $n\sigma_e$ efficiency calculations that are based on a fitting method, which is used in the raw signal correction, and a counting method (the alternative method). To calculate the $n\sigma$ efficiency via the counting method, the number of pure electrons (the sample requirements are defined in Sec. 4.5.3) is counted before and after imposing the $n\sigma_e$ requirements. In Fig. 4.10, the $n\sigma$ efficiency ($\frac{N_{\text{after}}}{N_{\text{before}}}$) via the counting method is shown as the brown crosses in the right image, labeled “Count Method”. In Fig. 4.18, the difference between the two $n\sigma$ efficiency calculations is shown to decide on a systematic uncertainty. A 2% systematic uncertainty is used as a conservative estimate. It is conservative because the majority of the identified electrons have a low momentum, where the systematic uncertainty is negligible.

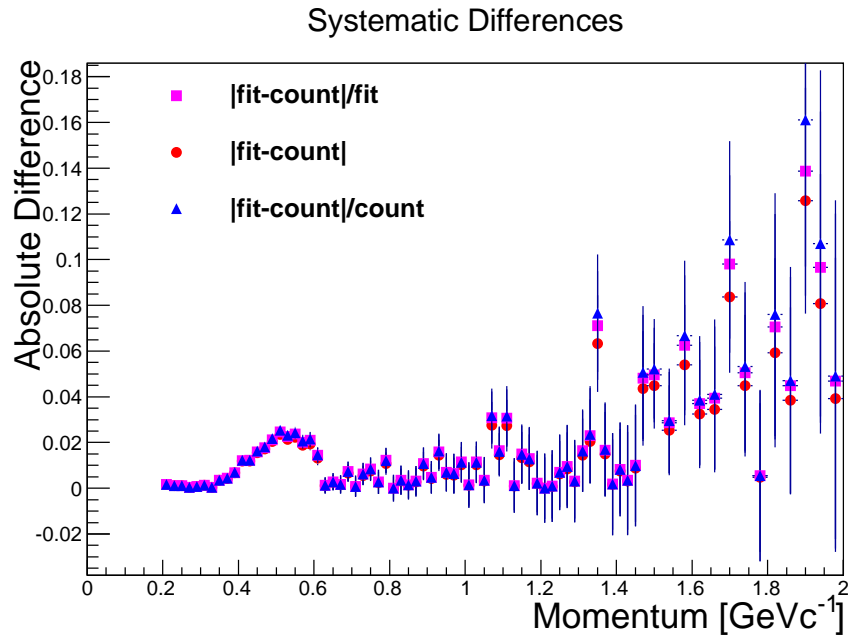


Figure 4.18 : The difference between the fit and count method efficiency calculations as a function of momentum. The different markers represent the absolute (red) and relative (blue with respect to the count method, pink with respect to the fit method) differences between the two methods.

4.6.4 Hadron Contamination

The estimation of hadron contamination in the e^+e^- continuum is taken into account as a systematic uncertainty. Estimation of the systematic uncertainty is accomplished by taking pure hadron (π , K , and p) samples and mixing the hadrons with the electron sample. This mixed sample is used to form the e^+e^- measurement in Fig. 4.8. Mixing the pure hadron sample with the electron sample results in the reconstruction of hadron-hadron ($h-h$), hadron-electron ($h-e$), and electron-electron ($e-e$) samples. Background subtraction techniques are applied to the reconstructed $h-h$, $h-e$, and $e-e$ samples to determine the relative $h-h$ and $h-e$ signal within the $e-e$ signal (*i.e.*, the relative hadron contamination in the signal).

The pure hadron sample is created with the same event and quality track criteria listed in Sec. 4.1 and 4.2, respectively. An additional requirement is appended to the particle identification criteria, where π are selected with the requirements $|\beta^{-1} - \beta_{\pi}^{-1}| < 0.01$ and $|\ln\sigma_{\pi}| < 2$, K are selected with the requirements $|\beta^{-1} - \beta_K^{-1}| < 0.01$ and $|\ln\sigma_K| < 2$, and p are selected with the requirements $|\beta^{-1} - \beta_p^{-1}| < 0.01$ and $|\ln\sigma_p| < 2$. To prevent double counting, tracks that satisfy the requirements for more than one particle species are omitted. When creating $h-h$ and $h-e$ pairs, each hadron is scaled by a weight based on their relative purity (P_x , where x is π , K, or p) levels with respect to the electron purity (P_e) as indicated by

$$W_{had} = \frac{P_{had}}{P_e} \times \frac{N_e}{N_h}, \quad (4.30)$$

where P is determined in Sec. 4.3.1 and N is the total number of hadrons ($h = \pi$, p, or K) and electrons (e) used in this analysis.

To demonstrate that the pure hadron samples are indeed pure, an example of the K-K foreground and background invariant mass distributions are shown in Fig. 4.19. Notice the bump in the K-K counts (red line) at $\sim 0.250 \text{ GeV}c^{-2}$. This bump corresponds to the reconstruction of the ϕ -meson, which is able to decay following $\phi \rightarrow K^+K^-$. The reason the bump is at $\sim 0.250 \text{ GeV}c^{-2}$, instead of $\sim 1.02 \text{ GeV}c^{-2}$, is because the hadrons are assumed to be electrons in the pair reconstruction (*i.e.*, the Ks have an electron mass instead of a K mass).

The uncorrected invariant mass signal of $e-e$ and the pure hadron contaminated sample ($h-h$ and $h-e$) are shown in Fig. 4.20. The uncorrected signals are the result of subtracting the geometric mean of the like-sign distributions with a charge-acceptance correction (Eq. 4.9) as a function of invariant mass and transverse momentum from the foreground. This method is also used to generate the uncorrected e^+e^- invariant mass signal in Fig. 4.8.

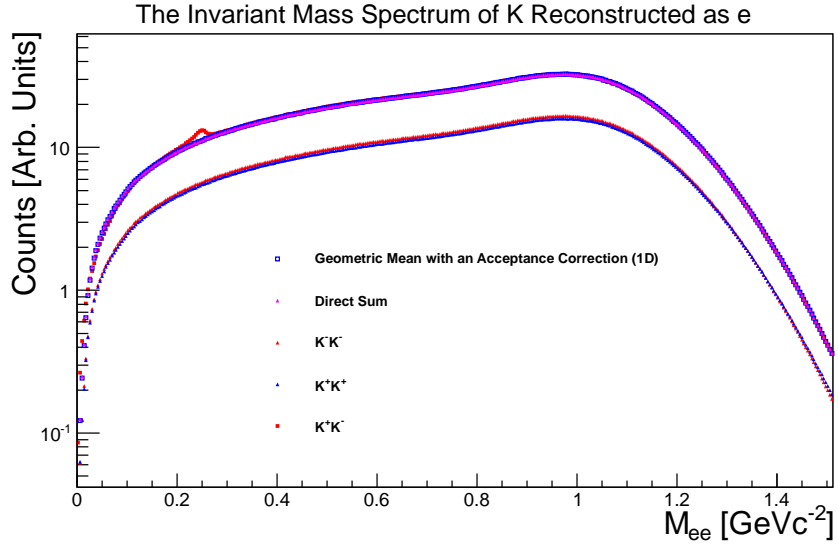


Figure 4.19 : The invariant mass distribution of K^+K^- (red square), K^+K^+ (blue triangle), K^+K^- (red triangle), the direct sum (pink triangle), and geometric mean (open square).

The relative systematic uncertainty from hadron contamination is found by dividing the pure hadron contaminated sample ($h-h$ and $e-h$) signal by the e^+e^- ($e-e$) signal. Because the amount of events recorded during the Au+Au collisions at $\sqrt{s_{NN}} = 27$ GeV is on the smaller side and this sample size leads to a large statistical uncertainty on the systematic uncertainty, the hadron contamination uncertainty in this analysis uses the systematic uncertainty from a similar analysis performed on Au+Au collisions at $\sqrt{s_{NN}} = 39$ GeV. In the analysis for Au+Au collisions at $\sqrt{s_{NN}} = 39$ GeV, the purity values are from the analysis of Au+Au collisions at $\sqrt{s_{NN}} = 39$ GeV, while the data samples for the hadron contamination study are from Au+Au collisions at $\sqrt{s_{NN}} = 200$ GeV. The 39 GeV sample is selected because it is close in collision energy ($\sqrt{s_{NN}} = 39$ GeV vs. 27 GeV), used a larger data sample in the purity estimation than the 19 GeV sample (another e^+e^- study available), and is

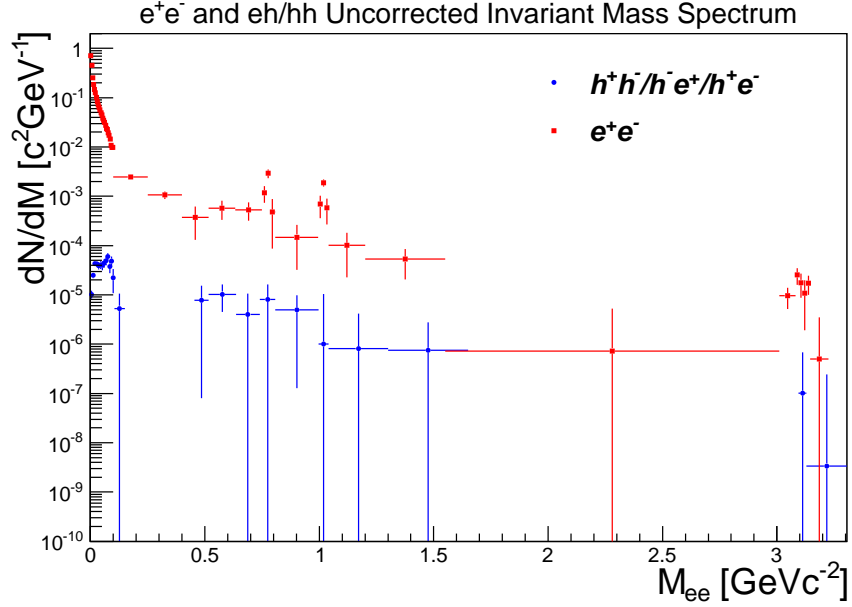


Figure 4.20 : The invariant mass distribution of e^+e^- (red) and $h^+h^-/h^+e^-/h^-e^+$ (blue). The uncertainties are statistical only.

being prepared for the same publication. The uncertainty from the Au+Au collisions at $\sqrt{s_{NN}} = 39$ GeV study and the relative uncertainties from Au+Au collisions at $\sqrt{s_{NN}} = 27$ with and without a charge-acceptance correction are shown in Fig. 4.21 as a function of invariant mass.

4.6.5 Charge Acceptance

In this study, the charge-acceptance correction factor ($c.f. = \frac{ME_{+-}}{2\sqrt{ME_{--}ME_{++}}}$) is used as a function of invariant mass (M_{ee}) and transverse momentum (p_T^{ee}) of the e^+e^- pair (*i.e.*, a 2D correction). The systematic uncertainty is approximated by comparing the charge-acceptance correction factor as a 1D correction (invariant mass of the e^+e^- pair) to the charge-acceptance correction factor as a 2D correction. Each correction factor is applied to the geometric mean of the like-sign distributions (Eq. 4.9). Due to

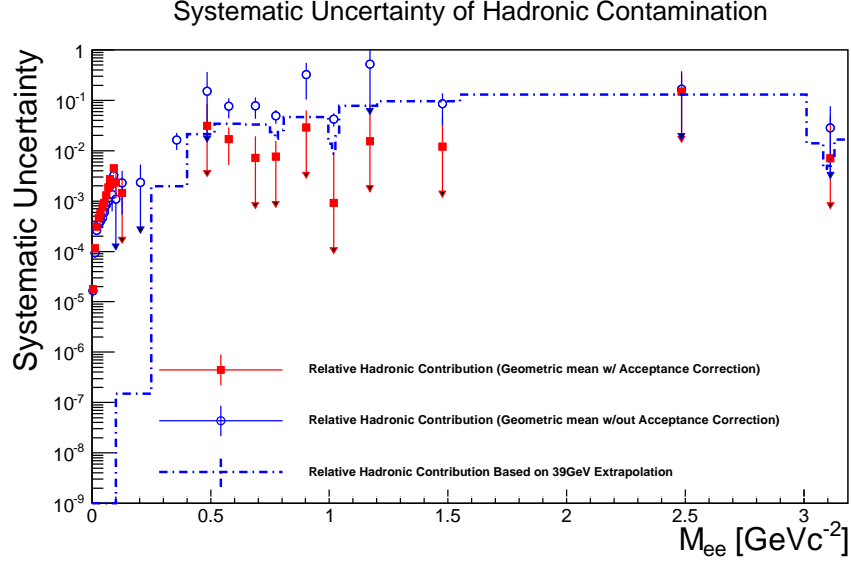


Figure 4.21 : The relative systematic uncertainty of hadron contamination as a function of invariant mass. The quoted uncertainty in this analysis is from a similar study on Au+Au collisions at $\sqrt{s_{NN}} = 39$ GeV. For reference, the relative uncertainties from Au+Au collisions at $\sqrt{s_{NN}} = 27$ are shown for when the geometric mean was corrected with a charge acceptance correction (red square) and without a charge acceptance correction (blue open point). Vertical error bars shown are statistical.

a limited amount of data, the geometric mean ($2\sqrt{N_{++}N_{--}}$) has been calculated with e^+e^- pairs reconstructed with electrons from different events within the same event class (*i.e.*, mixed events) instead of e^+e^- pairs reconstructed with electrons from the same event. To ensure that using a mixed event sample of e^+e^- pairs is an acceptable replacement of a sample with e^+e^- pairs from the same event, the ratio of e^+e^+ to e^-e^- as a function of invariant mass is compared for mixed and same events samples. In Fig. 4.22, the ratios are shown to be in agreement.

The relative difference between the charge acceptance-corrected geometric mean calculated as a function of M_{ee} and (M_{ee}, p_T^{ee}) is shown in Fig. 4.23, where the differences are relative to the geometric mean calculated as a function of (M_{ee}, p_T^{ee}) . The

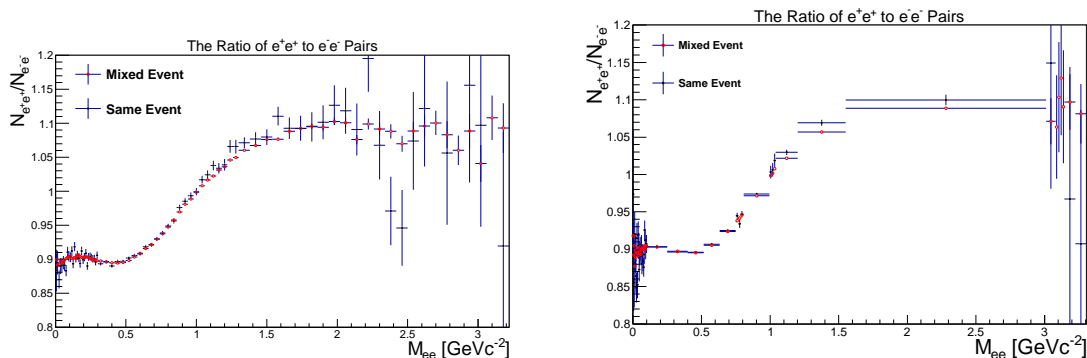


Figure 4.22 : The ratio e^+e^+ to e^-e^- as a function of invariant mass for pairs constructed from the same event and from mixed event samples. (Left) The ratio with a finer invariant mass binning for quality assurance. (Right) The ratio with the invariant mass binning used in the presentation of the final figures. The error bars are statistical uncertainties.

relative difference between the charge-acceptance correction factor methods is used to estimate the systematic uncertainty.

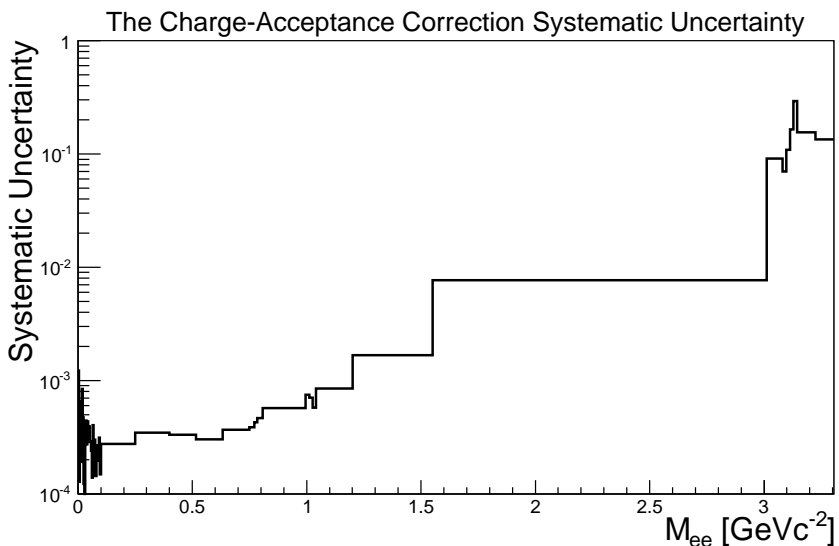


Figure 4.23 : The systematic uncertainty of the charge-acceptance correction as a function of invariant mass.

4.6.6 Total Systematic Uncertainty

The individual systematic uncertainties, listed Table 4.1, are added together to give a total systematic uncertainty. The total systematic uncertainty is applied as a function of invariant mass to the final e^+e^- invariant mass spectrum. The single track uncertainties are added in quadrature to find the total single track uncertainty. The total single track uncertainty is doubled to find the systematic uncertainty of paired tracks. In an effort to be conservative with the total systematic uncertainty, the uncertainty of the paired tracks is summed with the pair-based systematic uncertainties of the charge-acceptance correction factor and hadron contamination as a function of invariant mass. In Fig. 4.24, we show the total systematic uncertainty (solid black line), the charge-acceptance correction factor (dashed black line), the hadron contamination (dot-dashed blue line), and the pair efficiency uncertainties from single-track uncertainties (dot-long dashed pink line).

Table 4.1 : Systematic Uncertainties

Category	Systematic Uncertainty (%)	Section
Tracking	3.17	4.6.1
Matching	0.53	4.6.2
β^{-1}	2.0	4.6.3
$n\sigma_e$	1.3	4.6.3
Total Single Track	4.0	4.6.6
Paired Tracks	8.0	4.6.6

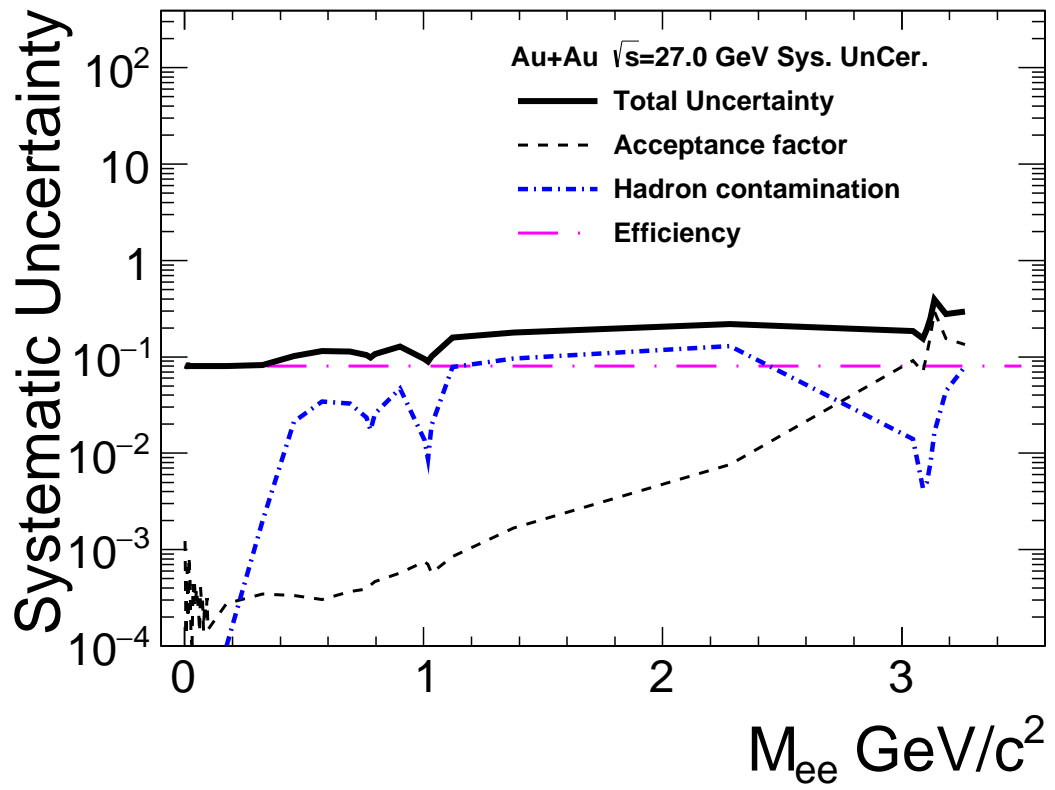


Figure 4.24 : The total systematic uncertainty as a function of the e^+e^- invariant mass for the top 80% most central Au+Au collisions at $\sqrt{s_{NN}} = 27$ GeV.

Chapter 5

Hadronic Cocktail

The hadronic cocktail is a mixture of known hadronic contributions to the e^+e^- continuum. The purpose of the cocktail is to separate the known hadronic contributions from the corrected e^+e^- signal. The separation is conducted by subtracting the hadronic cocktail from the corrected signal, which will leave behind the signal of interest. Expected known contributions to the e^+e^- continuum are $\pi^0 \rightarrow \gamma e^+e^-$, $\eta \rightarrow \gamma e^+e^-$, $\eta' \rightarrow \gamma e^+e^-$, $\omega \rightarrow e^+e^-$, $\omega \rightarrow \pi^0 e^+e^-$, $\phi \rightarrow e^+e^-$, $\phi \rightarrow \eta e^+e^-$, $J/\Psi \rightarrow e^+e^-$, $c\bar{c} \rightarrow e^+e^-$, and Drell-Yan production ($q\bar{q} \rightarrow \gamma^* \rightarrow e^+e^-$). Contributions from the ρ and QGP are expected as well, but are unknown and need to be separated from the signal. Hence, the hadronic cocktail must include the expected contributions to separate out the ρ and QGP. In the hadronic cocktail, the $c\bar{c}$ and Drell-Yan processes are handled by PYTHIA [104], a program that simulates high-energy particle physics events, and will be discussed in Sec. 5.2. The remaining processes are handled by Monte Carlo calculations and will be discussed in Sec. 5.1.

5.1 Monte Carlo Cocktail

The Monte Carlo simulation works by generating events where a parent hadron is created based on its invariant mass, rapidity (y), and transverse momentum (p_T) distributions and then decayed into e^+e^- pairs, where the e^+e^- pairs are then reconstructed. The reconstructed e^+e^- pair distributions are normalized and scaled to

match the e^+e^- production with a $M_{ee} < 0.1 \text{ GeV}c^{-2}$ in Au+Au collisions at $\sqrt{s_{NN}} = 27 \text{ GeV}$.

5.1.1 Parent Invariant Mass

The parent hadron mass is handled differently if the decay process is a direct decay into a e^+e^- pair ($\omega \rightarrow e^+e^-$, $\phi \rightarrow e^+e^-$, and $J/\Psi \rightarrow e^+e^-$) than if the decay process is a Dalitz decay into a e^+e^- pair ($\pi^0 \rightarrow \gamma e^+e^-$, $\omega \rightarrow \pi^0 e^+e^-$, $\phi \rightarrow \eta e^+e^-$, $\eta \rightarrow \gamma e^+e^-$, and $\eta' \rightarrow \gamma e^+e^-$). The mass distribution for a direct decay follows a narrow Breit-Wigner given by

$$\frac{dN}{dM_{ee}} = \frac{2\Gamma_0}{(M_{ee} - M_h)^2 + \Gamma_0^2/4}, \text{ for } M_{ee} \geq 2M_e, \quad (5.1)$$

where M_{ee} is the e^+e^- invariant mass, M_h is the pole mass of the parent hadron, and Γ_0 is the Particle Data Group (an organization dedicated to reviewing and maintaining a comprehensive list of particle data) width [45].

Dalitz decays follow the Kroll-Wada formula [119],

$$\frac{dN}{dM_{ee}} = PS \times |F(M_{ee}^2)|^2 \times G, \quad (5.2)$$

where PS is the phase space factor, $F(M_{ee}^2)$ is the form factor, and G is the quantum electrodynamics term.

The phase space factor for a three-body decay is described by

$$PS = \left(\left(1 + \frac{M_{ee}^2}{M_h^2 - M_d^2} \right)^2 - \frac{4M_h^2 M_{ee}^2}{(M_h^2 - M_d^2)^2} \right)^{\frac{3}{2}}, \quad (5.3)$$

where M_d is the pole mass of the daughter, and if the daughter is massless (*i.e.*, a photon), the phase space factor (Eq. 5.3) can be simplified to

$$PS = \left(1 - \frac{M_{ee}^2}{M_h^2} \right)^3. \quad (5.4)$$

The quantum electrodynamic kinematic term (G) supplies the universal decay rate factor [115, 119] for the process $\gamma^* \rightarrow e^+e^-$ and is given by

$$G = \frac{N}{3\pi} \sqrt{1 - \frac{4M_e^2}{M_{ee}^2}} \left(1 + \frac{2M_e^2}{M_{ee}^2}\right) \frac{1}{M_{ee}}, \quad (5.5)$$

where M_e is the electron mass and N is a degeneracy factor that depends on how many photons can convert. $N = 4$ for ω and ϕ , and $N = 2$ for π^0 , η , and η' .

The electromagnetic transition form factor is given by [120, 43, 121]

$$|F(M_{ee}^2)|^2 = \frac{1}{(1 - M_{ee}^2\Lambda^{-2})^2 + \Gamma_0^2\Lambda^{-2}}, \quad (5.6)$$

where Λ^{-2} and Γ_0^2 are listed in Table 5.1. The Γ_0^2 factor was implemented in [42] to account for the fact that the $\eta' \rightarrow \mu^+\mu^-\gamma$ allowed region for the $\mu^+\mu^-$ pairs invariant mass spectrum overlaps with the ω and ρ poles [43]. In the special case of π^0 , the form factor is as follows [45]:

$$|F(M_{ee}^2)|^2 = (1 + M_{ee}^2\Lambda^{-2})^2. \quad (5.7)$$

Table 5.1 : Form factor parameters used in Eq. 5.6 and Eq. 5.7. The parameters for η' have been derived by refitting [42] the data presented in [43].

Particle	$\Lambda^{-2} (GeV/c^2)^{-2}$	$\Gamma_0^2 (GeV/c^2)^2$
π^0 [45]	1.756	N/A
η [120]	1.95	0
η'	1.8396	0.1989
ω [120]	2.24	0
ϕ [121]	3.8	0

5.1.2 Parent Rapidity

The rapidity distribution of the parent is taken from CERES' Monte Carlo event generator GENESIS [122, 123, 124], which has been parameterized by CERES data, and is defined as

$$\frac{dN}{dy} = \cosh^{-2} \left(\frac{3y}{4\sigma_L \left(1 - \frac{y^2}{2\sqrt{s}/M_h} \right)} \right),$$

$$\sigma_L = \sqrt{\log \left(\frac{\sqrt{s}}{2M_N} \right)}. \quad (5.8)$$

In Eq. 5.8, \sqrt{s} is the center-of-mass energy per nucleon pair (27 GeV) and M_N is the nucleon mass, which has been approximated to be $0.939 \text{ GeV}c^{-2}$ (the average of the proton and neutron mass).

5.1.3 Parent Transverse Momentum

The transverse momentum of the parent is given by a Tsallis Blast Wave function [125] for π^0 , η , η' , ω , and ϕ , and a Boltzmann distribution for J/Ψ . The Tsallis Blast Wave model has been used to account for the collective motion of particles that have been produced in the later stages of the heavy-ion collisions. The Boltzmann distribution is used for J/Ψ because J/Ψ are generally produced in the earlier stages of the heavy-ion collisions before the collective motion of particles develops in the collision.

The Tsallis Blast Wave model is given by*

$$\frac{dN}{dp_T} \propto p_T m_T \int_{-\pi}^{\pi} d\phi \int_{-Y}^Y \cosh(y) dy \int_0^R r dr \left(1 + \frac{q-1}{T} E_T(r, y, \phi) \right)^{\frac{-1}{q-1}}, \quad (5.9)$$

*This equation is based on the $dN/m_T dm_T$ equation listed in [125], but with a change of variables.

where r is the radial direction, y is the rapidity, ϕ is the azimuthal angle of the particle, q represents the degree of non-equilibrium of the system with the range $[0,1]$ and when $q \rightarrow 1$ the Boltzmann distribution is recovered [126] from the equation, T is the temperature, $m_T = \sqrt{p_T^2 + m^2}$, and E_T is given by

$$E_T(r, y, \phi) = m_T \cosh(y) \cosh(\rho(r)) - p_T \sinh(\rho(r)) \cos(\phi). \quad (5.10)$$

In Eq. 5.10, ρ represents the flow profile and is defined as

$$\rho(r) = \arctan\left(\beta_s \left(\frac{r}{R}\right)^n\right). \quad (5.11)$$

The flow profile is zero at the center of the collision and expands radially to β_s at the hard spherical edge (R), where β_s is the maximum flow velocity and may be expressed as a function of the average flow velocity (β) as given by

$$\beta_s = \beta \left(1 + \frac{1}{n+1}\right). \quad (5.12)$$

In Eq. 5.12, n is taken to be 1, as done in [125]. For this study, the limits for y and r are taken to be $[-6,6]$ and $[0,R]$, respectively.

To setup the Tsallis Blast Wave model for use in the cocktail, the model is fitted to measured spectra. Fits are performed on $\pi^{+/-}$, $K^{+/-}$, p , and \bar{p} spectra from Au+Au collisions at $\sqrt{s_{NN}} = 27$ GeV [19]. The measured spectra are provided for the following centralities: 0-5%, 5-10%, 10-20%, 20-30%, 30-40%, 40-50%, 50-60%, 60-70%, and 70-80%. The centralities are combined to estimate the 0-80% centrality by weighting each distribution by 5%, 5%, 10%, 10%, 10%, 10%, 10%, 10%, 10%, and 10%, respectively, and then dividing by 0.8 to account for the 0-80% centrality coverage. The fits are performed simultaneously over the 6 sets of spectra with a p_T range of 0 to 2 GeVc⁻¹, where 13 variables are used (see Table 5.2), and the fits are shown in Fig. 5.1. The π^+ and π^- are treated as the same species and share the same amplitude

to help constrain the fits. The resulting fit parameters $q = 1.014$, $T = 0.1222$ GeV, and $\beta = 0.3927$ c are used to generate the dN/dp_T curves in the hadronic cocktail. All of the variables and fit results are listed in Table 5.2.

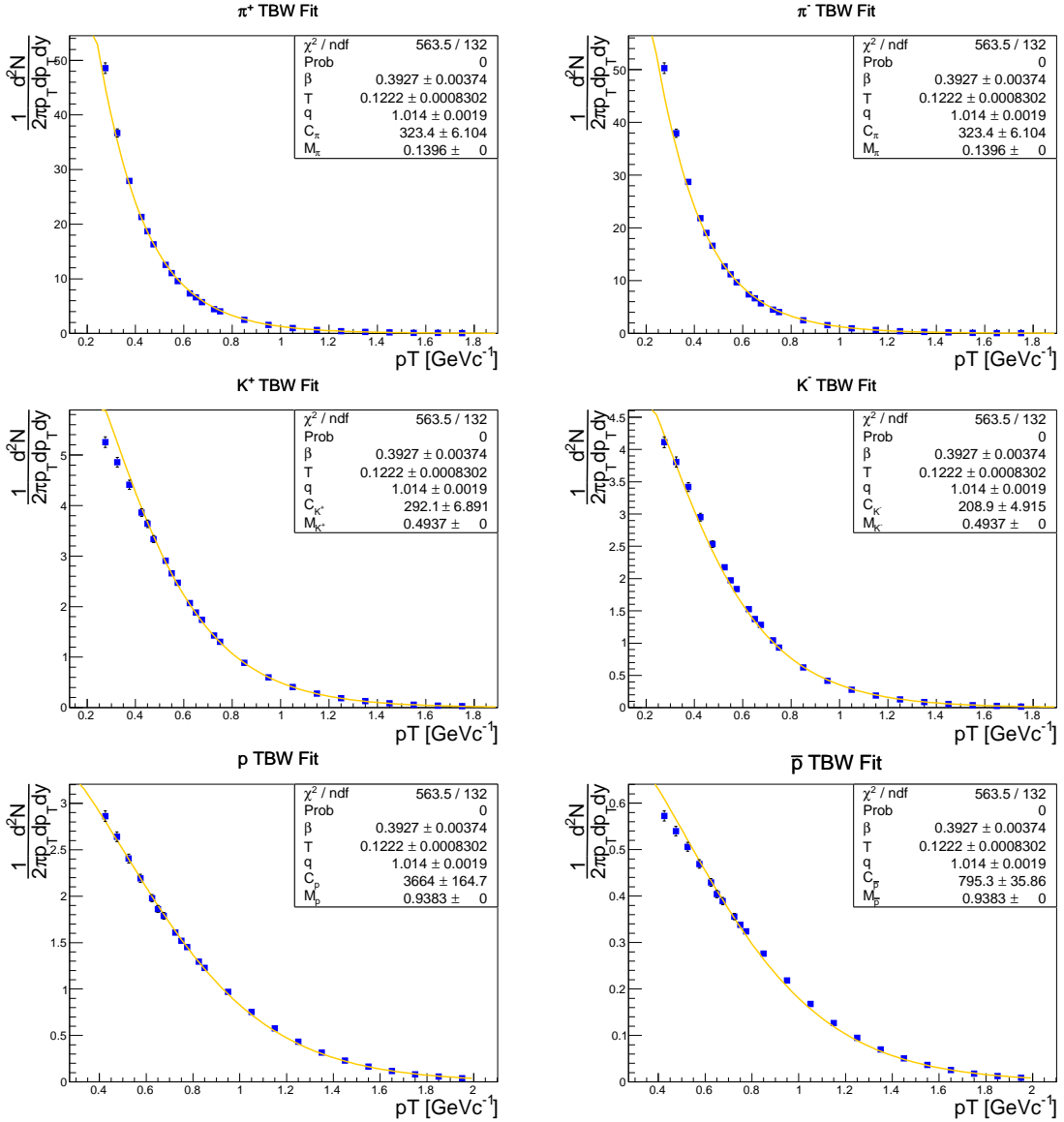


Figure 5.1 : The Tsallis Blave Wave fits on π , K , p spectra from [19, 20].

Table 5.2 : Tsallis Blast Wave fit parameters. β [c] is the average flow velocity, T [GeV] is temperature, q is the non-equilibrium of the system, C is a constant/amplitude, and M [GeVc⁻²] is the hadron mass.

Parameter	Initial Value	Step Size	Limits	Final Value
β	0.4	0.001	0, 0.7	0.3927 ± 0.00374
T	0.08825	0.001	0.040, 0.2	0.1222 ± 0.0008302
q	1.0535	0.001	0.8, 1.2	1.014 ± 0.0019
C_π	300	5	0, 1E4	323.4 ± 6.104
M_π	0.13957	Fixed	Fixed	0.13957
C_{K^+}	300	5	0, 1E4	292.12 ± 6.891
M_{K^+}	0.493677	Fixed	Fixed	0.493677
C_{K^-}	300	5	0, 1E4	208.948 ± 4.915
M_{K^-}	0.493677	Fixed	Fixed	0.493677
C_{p^+}	300	5	0, 1E4	3664.37 ± 164.676
M_{p^+}	0.938272	Fixed	Fixed	0.938272
C_{p^-}	300	5	0, 1E4	795.264 ± 35.8599
M_{p^-}	0.938272	Fixed	Fixed	0.938272

The Boltzmann distribution is given by

$$\frac{dN}{dp_T} \propto p_T \times \frac{dN}{dy} \frac{1}{2\pi T (T + m_{J/\Psi})} e^{-\left(\frac{\sqrt{p_T^2 + m_{J/\Psi}^2} - m_{J/\Psi}}{T}\right)}, \quad (5.13)$$

where $T = 0.4049$ GeV, $m_{J/\Psi} = 3.096916$ GeVc⁻²- J/Ψ mass [45], and $\frac{dN}{dy} = 3.237E-5$. These parameters are from the Au+Au collisions at $\sqrt{s_{NN}} = 39$ GeV simulation, based on a study of the J/Ψ p_T spectra [127].

5.1.4 Parent Decay

The parent hadrons are generated by randomly selecting a p_T , rapidity, and mass from the appropriate distributions mentioned in Sec. 5.1.3 Parent Transverse Momentum, Sec. 5.1.2 Parent Rapidity, and Sec. 5.1.1 Parent Invariant Mass, respectively, while the azimuthal angle (ϕ) is selected from a flat distribution $[0,2\pi]$. Once the parent hadron is generated, the parent hadron either follows a two-body (direct) decay or a three-body (Dalitz) decay.

For two-body decays, the e^+e^- pair is decayed in the rest frame of the parent hadron and then the pair is boosted into the laboratory frame. Below, the kinematic equations for each daughter are listed as follows:

$$p_{1;2} = \sqrt{\frac{M_{ee}^2}{4} - m_e^2}, \quad (5.14)$$

$$p_{1;x} = p \sin \theta \cos \phi; \quad p_{2;x} = -p_{1;x}, \quad (5.15)$$

$$p_{1;y} = p \sin \theta \sin \phi; \quad p_{2;y} = -p_{1;y}, \quad (5.16)$$

$$p_{1;z} = p \cos \theta; \quad p_{2;z} = -p_{1;z}, \quad (5.17)$$

$$E_{1;2} = \sqrt{m_e^2 + p_{1,2;x}^2 + p_{1,2;y}^2 + p_{1,2;z}^2}, \quad (5.18)$$

where M_{ee} is selected randomly based on the distribution given by Eq. 5.1, $\cos \theta$ is randomly selected from a flat distribution $[-1,1]$, ϕ is randomly selected from a flat distribution $[0,2\pi]$, p is the magnitude of the momentum, E is the energy, and the numeric subscript represents daughter 1 and daughter 2.

For three-body decays, the e^+e^- pair and the third body, either a daughter γ or daughter hadron (γ/h), are decayed as a two-body decay in the rest frame of the parent hadron. The e^+e^- pair then decays in their center-of-mass frame. The daughter e^+e^- pair and γ/h are boosted into the frame of the parent, and all three particles are then boosted into the laboratory frame. The kinematics for the first decay frame are as follows:

$$P_{h/\gamma/ee} = \frac{\sqrt{\left(M_{\text{parent}}^2 - (M_{ee} + M_{h/\gamma})^2\right) \left(M_{\text{parent}}^2 - (M_{ee} - M_{h/\gamma})^2\right)}}{2M_{\text{parent}}}, \quad (5.19)$$

$$p_{h/\gamma;x} = P_{h/\gamma/ee} \sin \theta \cos \phi; \quad p_{ee;x} = -p_{h/\gamma;x}, \quad (5.20)$$

$$p_{h/\gamma;y} = P_{h/\gamma/ee} \sin \theta \sin \phi; \quad p_{ee;y} = -p_{h/\gamma;y}, \quad (5.21)$$

$$p_{h/\gamma;z} = P_{h/\gamma/ee} \cos \theta; \quad p_{ee;z} = -p_{h/\gamma;z}, \quad (5.22)$$

$$E_{ee} = \sqrt{M_{ee}^2 + p_{ee;x}^2 + p_{ee;y}^2 + p_{ee;z}^2}, \quad (5.23)$$

$$E_{h/\gamma} = \frac{\sqrt{M_{\text{parent}}^2 + M_{h/\gamma}^2 - M_{ee}^2}}{2M_{\text{parent}}}, \quad (5.24)$$

where $\cos \theta$ is selected from a flat distribution of $[-1,1]$, ϕ is selected from a flat distribution of $[0,2\pi]$, M_{ee} is selected from Eq. 5.2, and M_{parent} is the mass of the parent hadron. Once in the laboratory frame, the transverse momentum for each track is smeared to simulate what the measured e^+e^- pairs look like when detected.

5.1.5 Momentum Resolution

Smearing of the transverse momentum follows a double Crystal Ball function [128] as given by

$$\frac{dN}{dx} = \begin{cases} A(B - \frac{x-\bar{x}}{\sigma})^{-n} & \text{if } \frac{x-\bar{x}}{\sigma} < -\alpha \\ e^{-\frac{(x-\bar{x})^2}{2\sigma^2}} & \text{if } -\alpha \leq \frac{x-\bar{x}}{\sigma} < \beta \\ C(D + \frac{x-\bar{x}}{\sigma})^{-m} & \text{if } \frac{x-\bar{x}}{\sigma} \geq -\alpha \text{ and } \geq \beta \end{cases} \quad (5.25)$$

with

$$A = \left(\frac{n}{|\alpha|} \right)^n e^{-\frac{|\alpha|^2}{2}}, \quad (5.26)$$

$$B = \frac{n}{|\alpha|} - |\alpha|, \quad (5.27)$$

$$C = \left(\frac{m}{|\beta|} \right)^m e^{-\frac{|\beta|^2}{2}}, \quad (5.28)$$

$$D = \frac{m}{|\beta|} - |\beta|, \quad (5.29)$$

where x is the relative shift between the original (p_T^{sim}) and reconstructed (p_T^{reco}) momenta $\left(\frac{p_T^{reco} - p_T^{sim}}{p_T^{reco}} \right)$ of simulated tracks that have been embedded into real events, α and β are the limits that define ranges of the two power-law tails and the Gaussian core, and the parameters \bar{x} , α , β , σ , n , and m are determined by fitting the double Crystal ball function to embedding and are defined in Table 5.3.

Table 5.3 : The double Crystal Ball and resolution parameters used to describe the resolution of the transverse momentum.

N	n	α	m	β	\bar{x}	σ	a [c/GeV]	b
1	1.224	1.812	4.325	2.145	-3.278E-4	9.319E-3	9.6E-3	7.934E-3

The smearing of the transverse momentum of each track is performed by

$$p_T = p_T + \frac{dN}{dx} \frac{\delta p_T}{0.01}. \quad (5.30)$$

The initial transverse momentum of the simulated track is smeared by adding the double Crystal Ball parameterization (refer to Eq. 5.25) to the initial transverse momentum, where δp_T (the p_T resolution) is given by

$$\delta p_T = \frac{\sigma}{p_T} = \sqrt{a^2 p_T^2 + b^2}. \quad (5.31)$$

The relative shift between the original and reconstructed momenta is scaled up to a p_T resolution of 1%. This is because the reconstruction of the simulated tracks in the real events (*i.e.*, embedding) typically underestimate the amount of momentum smearing, and the $\left(\frac{p_T^{reco} - p_T^{sim}}{p_T^{reco}}\right)$ fitted by the double Crystal Ball function is presented over a range of p_T from 0.2 to 2.0 GeVc⁻¹ (the amount of smearing increases as p_T increases, so a large p_T range is less than ideal). To scale the relative shift between the original and reconstructed momenta to 1%, the p_T resolution of the simulated tracks reconstructed in real events is determined and performed in a similar fashion as the resolution definition in Fig. 10 of Ref. [26], where the Gaussian widths (σ) of $\left(\frac{p_T^{reco} - p_T^{sim}}{p_T^{reco}}\right)$ are determined as a function of the transverse momentum. To determine a and b in Eq. 5.31, the Gaussian width of the relative shift between the original and reconstructed tracks is found as a function of p_T and fit with Eq. 5.31. The result of the fit (*i.e.*, the relative p_T resolution as a function of p_T) is shown in Fig. 5.2.

After scaling $\left(\frac{p_T^{reco} - p_T^{sim}}{p_T^{reco}}\right)$ to match the 1% resolution based on the resolution fit (refer to Eq. 5.31), the double Crystal Ball function (refer to Eq. 5.25) is fitted to $\frac{p_T^{reco} - p_T^{sim}}{p_T^{sim}}$ for p_T from 0.2 to 2.0 GeVc⁻¹ to obtain the tail shape of the p_T smearing (as shown in Fig. 5.3).

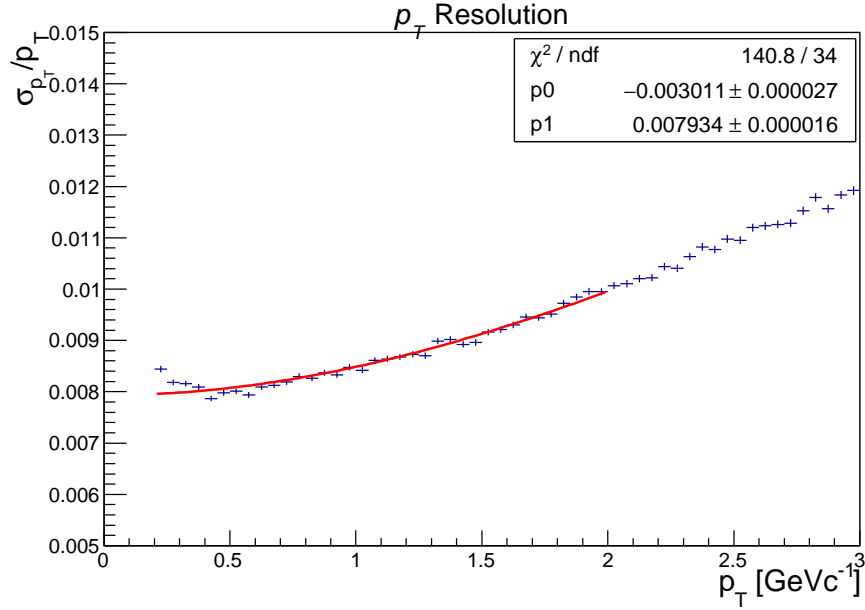


Figure 5.2 : The p_T resolution of the embedding sample as a function of p_T [GeVc^{-1}]. The p_T resolution is given as the Gaussian σ of $\left(\frac{p_T^{\text{reco}} - p_T^{\text{sim}}}{p_T^{\text{reco}}}\right)$ as a function of p_T . The red line is the result of fitting Eq. 5.31.

Now that the tail shape (*i.e.*, double Crystal Ball) and initial p_T resolution (Eq. 5.31) parameters have been determined, a χ^2 minimization is used to adjust the resolution parameters to match data. This is because the smearing of simulated tracks reconstructed in real events may be underestimated and data can be used as a reliable means to determine the p_T resolution. The J/Ψ is chosen as the data sample because the width of the J/Ψ 's invariant mass distribution is narrow and broadening of the width can be attributed to Bremsstrahlung and detector resolution effects. In the χ^2 minimization, the parameter a in Eq. 5.31 is varied while b is fixed from the fit to embedding sample shown in Fig. 5.2. Here, a represents the TPC calibration effect on the resolution and b represents the single hit effect on the resolution, which is modeled correctly in the reconstruction of simulated tracks

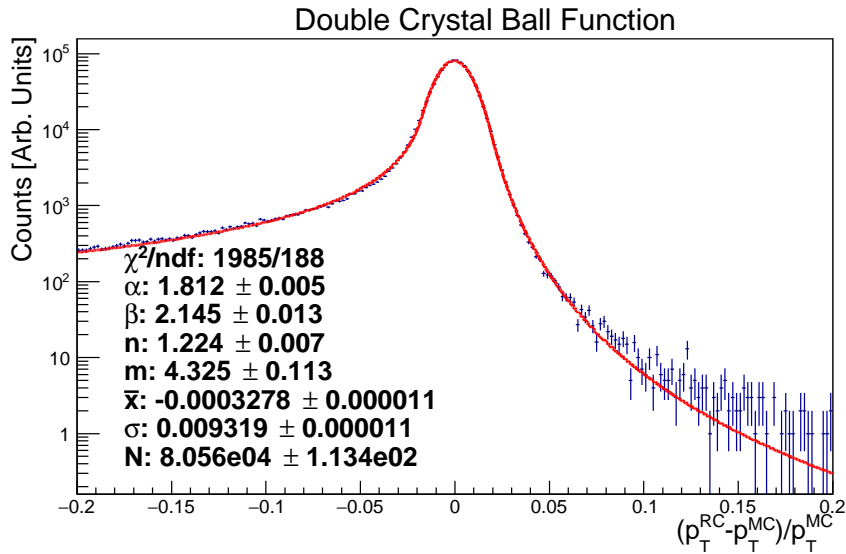


Figure 5.3 : The double Crystal Ball function (Eq. 5.25) fit to $\frac{p_T^{reco} - p_T^{sim}}{p_T^{sim}}$ for p_T from 0.2 to 2.0 $\text{GeV}c^{-1}$.

implemented in real events. The χ^2 is found by fitting the cocktail histogram to the data in the J/Ψ invariant mass region. The cocktail in the J/Ψ invariant mass region (*i.e.*, 2.8-3.2 $\text{GeV}c^{-2}$) is comprised primarily of J/Ψ , $c\bar{c}$, and Drell-Yan contributions. To determine the lowest χ^2 , many hadronic cocktails are generated and each cocktail has a different a parameter. The fit to the data with the lowest χ^2 (*i.e.*, the best fitting cocktail) provides the a parameter that is used in the final cocktail. The parameter a is found to be $9.6\text{E-}3$ c/GeV with $b = 7.9\text{E-}3$.

5.2 $c\bar{c}$ and Drell-Yan

The $c\bar{c}$ and Drell-Yan contributions to the e^+e^- continuum are modeled by taking the kinematics distributions given by PYTHIA [104] and then scaling the normalized distributions based on the number of nucleon-on-nucleon collisions (N_{coll}) to produce

the e^+e^- contribution from Au+Au collisions at $\sqrt{s_{NN}} = 27$ GeV.

PYTHIA version 6.416 is used to simulate the production of $c\bar{c}$ pairs from proton-on-proton ($p + p$) collisions at $\sqrt{s} = 27$ GeV. PYTHIA is configured to run with the following program settings: $MSEL = 1$, $PARP(91) = 1$, $PARP(67) = 1$, and the rest of the settings are the default values. The simulated events are only considered if there are exactly two strings from either c or \bar{c} , where a string is considered an object that stretches from an anti-quark end to the of another quark via some number of intermediate gluons and has an invariant mass above a threshold defined by PYTHIA. The $c\bar{c}$ pair production is measured through the decay of charmed mesons ($D^{+/-}$, D^0 , \bar{D}^0 , and $D_s^{+/-}$) and baryon ($\Lambda_c^{+/-}$) into e^+e^- pairs. These charmed hadrons could decay into other particles, but those decays are disabled in this simulation configuration. The e^+e^- pairs are reconstructed within the STAR detector acceptance. The yield e^+e^- pairs from $c\bar{c}$ production will be discussed in Sec. 5.3.

The Drell-Yan contributions are also based on the kinematic distributions by PYTHIA and scaled by N_{coll} . These contributions are modeled with PYTHIA 6.416 and the PYTHIA setup in this study uses the same settings as Refs. [17, 38], which are as follows: $MSEL = 11$, $MSTP(43) = 1$, $MSTP(33) = 1$, $MSTP(32) = 4$, $PARP(31) = 1.8$, $PARP(91) = 1.5$, $PARP(67) = 4$, $MDME(174-189,1) = 0$, $MDME(182,1) = 1$, and $CKIN(1) = 1.0$.

5.3 Scaling

Once the e^+e^- pairs are reconstructed and the kinematic distributions are known, the kinematic distributions need to be scaled such that the yields match the expected channel production in Au+Au collisions at $\sqrt{s_{NN}} = 27$ GeV. The yields for π^0 , η , η' ,

ω , and ϕ are scaled by following

$$\frac{1}{N} \frac{dN}{dM} = \frac{1}{nDecays} \left(\frac{dN}{dy} \right)_{\pi^0} dY \frac{\sigma_{had}}{\sigma_{\pi^0}} BR_{had \rightarrow (X)e^+e^-} \frac{dN}{dM}, \quad (5.32)$$

where $nDecays$ is the number of generated events, $\left(\frac{dN}{dY} \right)_{\pi^0}$ is the mean of STAR's measured $\left(\frac{dN}{dY} \right)_{\pi^-}$ and $\left(\frac{dN}{dY} \right)_{\pi^+}$ [19], dy is the differential rapidity from CERES' GENESIS (Sec. 5.1.2), $\frac{\sigma_{had}}{\sigma_{\pi^0}}$ is the cross-section ratio of the hadron to π^0 production at SPS [44] as listed in Table 5.4 (except for J/Ψ , which is mentioned later in this section), and $BR_{had \rightarrow (X)e^+e^-}$ is the branching ratio (*i.e.*, the rate a hadron decays into a given set of particles) given by the Particle Data Group [45] as found in Table 5.5.

Table 5.4 : The ratio of the cocktail hadron cross-sections to the π^0 cross-section taken from [44].

Channel	Ratio to σ_{π^0}
π^0	1.
η	0.085
ω	0.069
ϕ	0.018
η'	0.0078
J/Ψ	5.47859E-6

The $c\bar{c}$ yield is given by

$$\frac{1}{N} \frac{dN}{dM} = \frac{1}{nDecays} \left(\frac{dN}{dM} \right)_{pp} \frac{\sigma_{c\bar{c}}}{\sigma_{mb}} N_{coll} BR(c \rightarrow e^+) BR(\bar{c} \rightarrow e^-). \quad (5.33)$$

In Eq. 5.33, $nDecays$ is the number of generated $c\bar{c}$ events, $\sigma_{c\bar{c}}$ is the $p + p$ $c\bar{c}$ cross-section and $\sigma_{c\bar{c}} = 26.4 \pm 7.5 \mu\text{b}$, $\sigma_{mb} = 33 \text{ mb}$, $N_{coll} = 238.7$ [129], and BR is

Table 5.5 : The branching ratios used in the hadronic cocktail are taken from the Particle Data Group [45].

Channel	Branching Ratio
$\pi \rightarrow \gamma e^+ e^-$	1.174E-2
$\eta \rightarrow \gamma e^+ e^-$	6.9E-3
$\omega \rightarrow \pi^0 e^+ e^-$	7.7E-4
$\omega \rightarrow e^+ e^-$	7.28E-5
$\phi \rightarrow \eta e^+ e^-$	1.15E-4
$\phi \rightarrow e^+ e^-$	2.954E-4
$\eta' \rightarrow \gamma e^+ e^-$	9E-4
$J/\Psi \rightarrow e^+ e^-$	5.94E-2
$D^{+/-} \rightarrow e^{+/-} + X$	0.1607
$D^0/\bar{D}^0 \rightarrow e^{+/-} + X$	0.0649
$D_s^{+/-} \rightarrow e^{+/-} + X$	0.0605
$\Lambda_c^{+/-} \rightarrow e^{+/-} + X$	0.045

the branching ratio for a given decay and is found in Table 5.5. The $\sigma_{c\bar{c}}$ is determined by taking the midpoint between the upper Fixed-Order Next-to-Leading Logarithm (FONLL) calculation [34] limit and the FONLL upper limit curve fitted to the data in Fig. 5.4, where FONLL is software that calculates heavy quark (*i.e.*, c , b , and t) production cross-sections in $p + p$ collisions. The uncertainty of $\sigma_{c\bar{c}}$ is the absolute difference. The σ_{mb} is determined by subtracting the elastic cross-section (7 mb) from the total cross-section (40 mb) as given by the Particle Data Group [45].

The Drell-Yan scaling follows a similar method as $c\bar{c}$ in Eq. 5.33 except for a couple differences. One difference in methods is that charmed hadron branching

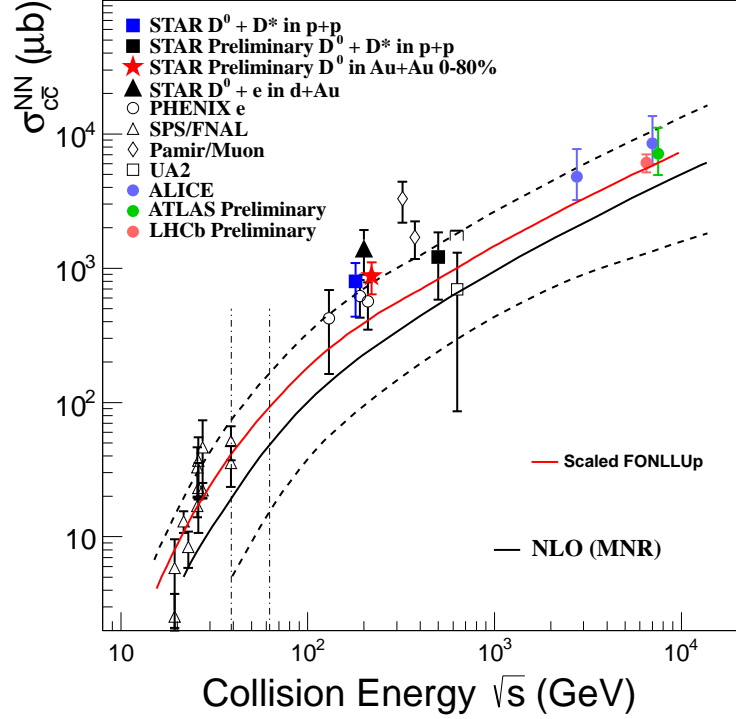


Figure 5.4 : The $c\bar{c}$ cross-section measurements as a function of collision energy [29, 30, 31, 32, 33]. The dashed curves represent the upper and lower limits of the FONLL predictions [34] and the red curve is the upper FONLL limit curve fitted to the measurements.

ratios are not applicable in the Drell-Yan simulation. The other major difference is in the determination of the Drell-Yan cross-section (σ_{DY}) for $p + p$ collisions at $\sqrt{s} = 27$ GeV. The σ_{DY} is approximated by taking the PYTHIA cross-section ($\sigma_{\text{DY}27}^{\text{PYTHIA}} = 17.27$ nb) at $\sqrt{s} = 27$ GeV and weighting the cross-section with the ratio between the cross-section for $p + p$ collisions at $\sqrt{s} = 19.6$ GeV given by PYTHIA ($\sigma_{\text{DY}19}^{\text{PYTHIA}} = 13.44$ nb) and the quoted cross-section in [37] ($\sigma_{\text{DY}19}^{\text{paper}} = 9.88$ nb), or

$$\sigma_{\text{DY}} = \sigma_{\text{DY}27}^{\text{PYTHIA}} \sigma_{\text{DY}19}^{\text{paper}} / \sigma_{\text{DY}19}^{\text{PYTHIA}}. \quad (5.34)$$

Since we estimate the dN/dM_{ee} of J/Ψ from the best fit of the cocktail to the data (refer to Sec. 5.1.5), the dN/dy of J/Ψ can be estimated and, ultimately, is used

to tune the cocktail's $\frac{\sigma_{J/\Psi}}{\sigma_{\pi^0}}$.

To estimate dN/dy , the following equation is used:

$$\frac{dN}{dy} = \frac{dN}{dM} \times dM \times \frac{1}{dy} \times \frac{J/\Psi_r}{J/\Psi_r + c\bar{c}_r + DY_r} \times \frac{J/\Psi_t}{J/\Psi_r} \times \frac{J/\Psi_t^N}{J/\Psi_t} \times \frac{1}{BR_{J/\Psi \rightarrow ee}}, \quad (5.35)$$

where $\frac{1}{dy}$ is CERES' rapidity parameterization from -3 to 3 (Sec. 5.1.2) the subscript r denotes the contribution in the M_{ee} range from 2.8 to 3.2 $\text{GeV}c^{-2}$, the subscript t denotes the total invariant mass range, the superscript N denotes contributions inside and outside the STAR acceptance, and BR is the J/Ψ to e^+e^- branching ratio.

The dN/dy for J/Ψ was found to be 1.6E-4 and the cross-section ratio comes out to be 5.47859E-6. However, because the overall cocktail is scaled to match the data in the 0-0.1 $\text{GeV}c^{-2}$ region, the ratio was shifted to match the rest of the cocktail's relative shift.

After scaling, the hadronic cocktail is shifted as a whole to match the corrected invariant mass distribution in the very low mass region (0.0-0.1 $\text{GeV}c^{-2}$). The resulting scale factor is 0.847134. We scale in the very low mass region because the region is dominated by the π^0 contribution with minimal contributions from other sources, making it a safe known source of e^+e^- pairs to scale to.

5.4 Cocktail Uncertainties

The uncertainties of the cross-sections used in the construction of the hadronic cocktail are listed in Table 5.6. In addition to the uncertainty of $\sigma_{c\bar{c}}$, the $c\bar{c}$ contributions also have a systematic uncertainty, where the correlation of $c\bar{c}$ decays is expected to be modified in Au+Au collisions with respect to $p + p$ collisions. To account for this uncertainty in the level of modification, the correlation between e^+e^- pairs is wiped out. This is accomplished by selecting, for each electron, a randomized azimuthal

angle (ϕ), pseudo-rapidity (η), and transverse momentum (p_T) based on the electron distributions from PYHTIA's $c\bar{c}$ production. The relative uncertainty is the difference between the “Default” and “Decorrelated ϕ , η , and p_T ” distributions with respect to the “Default” distribution shown in Fig. 5.5.

Table 5.6 : The uncertainties of the cross-sections used in the scaling of the hadronic cocktail. The uncertainties for the ratios of the cocktail hadron cross-sections to the π^0 cross-section are taken from [44]

Contribution	Uncertainty (%)
$\left(\frac{dN}{dy}\right)_{\pi^0}$	8
$\frac{\sigma_\eta}{\sigma_{\pi^0}}$	14
$\frac{\sigma_{\eta'}}{\sigma_{\pi^0}}$	16
$\frac{\sigma_\omega}{\sigma_{\pi^0}}$	13
$\frac{\sigma_\phi}{\sigma_{\pi^0}}$	17
$\frac{\sigma_{J/\Psi}}{\sigma_{\pi^0}}$	24
$\sigma_{c\bar{c}}$	28.4
σ_{DY}	30

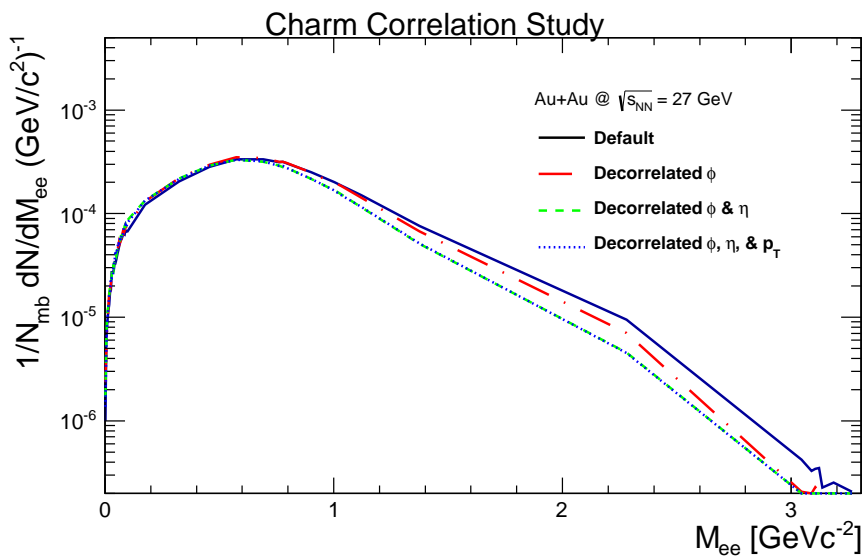


Figure 5.5 : The e^+e^- invariant mass distribution from $c\bar{c}$ decays with different assumptions for the correlation between the daughters. The black solid line is the distribution as is from PYTHIA. The red dot-dashed line is the distribution after randomizing each daughter's ϕ . The green dashed line is the distribution after randomizing both ϕ and η for each daughter. The blue dotted line is the distribution after randomizing each daughter's ϕ , η , and p_T .

Chapter 6

Results

The uncorrected e^+e^- measurements (shown in Fig. 4.8 of Sec. 4.4) are corrected with the e^+e^- pair efficiencies, as presented in Sec. 4.5.4, to give the efficiency corrected e^+e^- invariant mass spectrum in the STAR detector acceptance (the electron transverse momentum (p_T^e) $> 0.2 \text{ GeV}c^{-1}$, the electron absolute pseudo-rapidity ($|\eta^e|$) < 1 , and the absolute rapidity of the e^+e^- pair ($|Y_{ee}|$) < 1). In the upper panel of Fig. 6.1, the corrected e^+e^- invariant mass spectrum is shown as the blue points, with the errors bars representing the statistical uncertainty and the open boxes representing the systematic uncertainty. Also in the upper panel of Fig. 6.1, the hadronic cocktail is shown as the solid black curve with the cocktail uncertainty represented by the gray band and the hadronic components of the cocktail drawn as various curves. We observe an excess of e^+e^- pairs between the measured data and the hadronic cocktail in the low invariant mass region. In the bottom panel of Fig. 6.1, another quantification of the excess e^+e^- yield is presented as the ratio of the invariant mass measurements to the hadronic cocktail.

Contributions to the e^+e^- signal, which require some theoretical interpretation, are omitted from the hadronic cocktail (*e.g.*, the ρ and QGP contributions); hence, there is an expectation that some excess yield (*i.e.*, signal - cocktail) is present in the e^+e^- invariant mass spectrum. Because the expected ρ and QGP contributions and their kinematics are not trivial, model calculations that include the ρ and QGP contributions are used to compare and describe the excess yield in the e^+e^- invariant

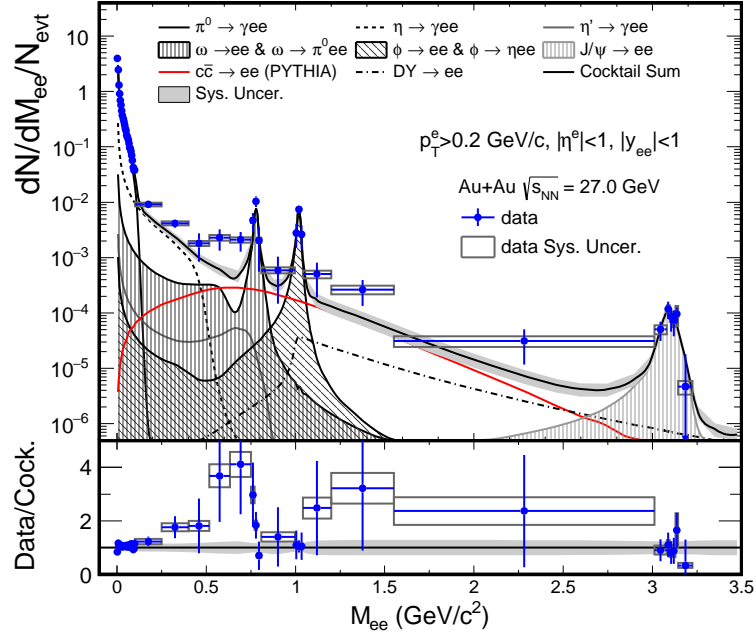


Figure 6.1 : (Top) The corrected e^+e^- invariant mass spectrum (blue points) in the STAR detector acceptance. For comparison, the hadronic cocktail is shown as the solid black curve. (Bottom) The ratio of the measurements (*i.e.*, data) to cocktail as a function of invariant mass. The error bars represent the statistical uncertainties. The open boxes represent the systematic uncertainties. The gray band represents the cocktail uncertainties.

mass spectrum. One such model calculation is provided by Rapp *et al.* [79, 80, 35, 36] where the spectral function of the ρ is modified by the hot, dense medium, which includes contributions from the QGP phase, as discussed in Sec. 2.3. These model calculations of the ρ and QGP e^+e^- production have been performed for Au+Au collisions at $\sqrt{s_{NN}} = 27$ GeV and are compared to the measurements of the e^+e^- invariant mass spectrum within the STAR detector acceptance. Comparison of the model calculations and the e^+e^- excess yield measurements are presented in Fig. 6.2, where the measurements are the black points, the hadronic cocktail is the solid black curve, calculations of the ρ and QGP provided by Rapp *et al.* are the pink

dashed and blue dashed curves, respectively, and the model calculations added to the hadronic cocktail is the solid red curve. Once the model calculations are added to the hadronic cocktail, the yields from simulations of the e^+e^- sources are consistent with the measurements of e^+e^- , within statistical and systematic uncertainties. To study the enhancement (*i.e.*, data over cocktail) in the low mass region, the model calculations by Rapp *et al.* are added to the hadronic cocktail and then divided by the hadronic cocktail (as shown in Fig. 6.3). There is agreement between the measured enhancement and simulated enhancement (ρ and QGP contributions) in the low mass region within uncertainties. The comparisons made in Fig. 6.2 and Fig. 6.3 suggest that the measurements of the e^+e^- pair production are consistent with the model calculations by Rapp *et al.* in which the ρ spectral function is being modified by the hot, dense medium.

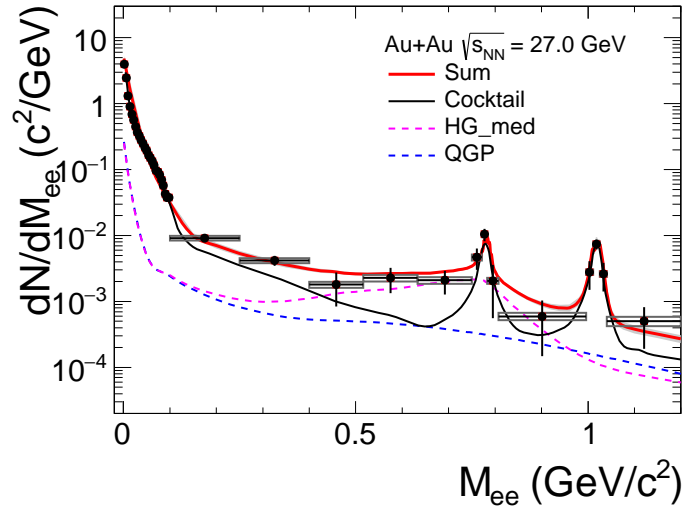


Figure 6.2 : (Top) The corrected e^+e^- invariant mass spectrum (black points) in the STAR detector acceptance shown with e^+e^- contributions from the hadronic cocktail (solid black curve), the QGP (blue dashed curve), ρ with a broadened spectral function (HG_med/pink dashed curve), and the sum of the calculations (red solid curve). The QGP and ρ calculations have been provided by Rapp *et al.* [35, 36].

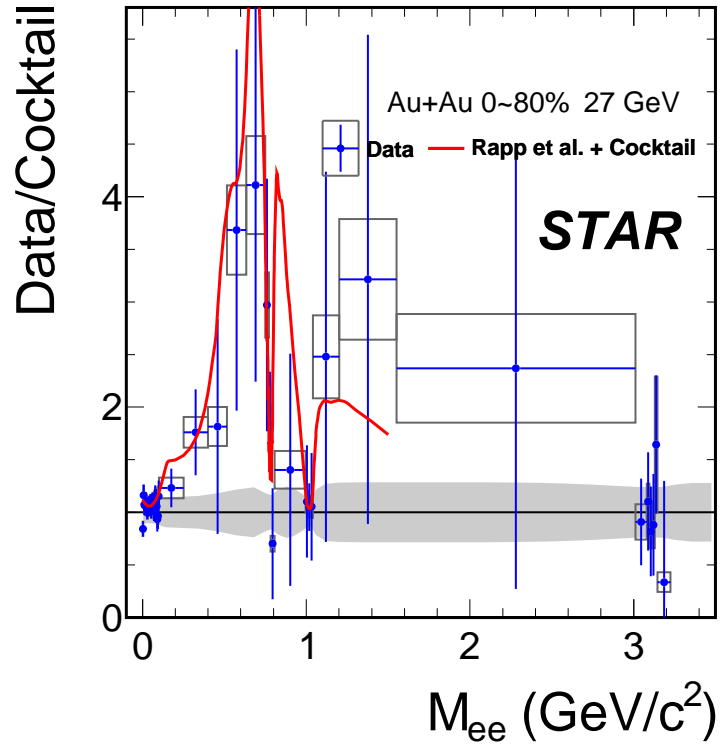


Figure 6.3 : The comparison of the hadronic cocktail plus contributions from Rapp *et al.* over the hadronic cocktail and data over the hadronic cocktail as a function of invariant mass. The cocktail uncertainties are represented by the gray band. The data statistical and systematic uncertainties are represented by the error bars and open boxes, respectively.

To enable comparisons between our excess yield measurements and the excess yields measured by other heavy-ion experiments and to explore the possible relationship between the excess yield and the lifetime of heavy-ion collisions [13], our measured excess yield is corrected for the STAR detector acceptance. To correct our measured excess yield for the STAR detector acceptance, the γ^* Monte Carlo in Sec. 4.5.4 is used to determine a STAR detector acceptance correction factor (cf_{acc}). The γ^* Monte Carlo is used to avoid an assumption about the ρ and QGP kinematics within the STAR detector acceptance and the corrected STAR detector acceptance.

The cf_{acc} is the ratio of the number of e^+e^- pairs before (N_{Before}) and after (N_{After}) the application of the STAR detector acceptance in the Monte Carlo, as given by

$$cf_{acc} = \frac{N_{Before}}{N_{After}}. \quad (6.1)$$

Then to correct the excess yield, the excess yield is multiplied by cf_{acc} as a function of invariant mass, but not as a function of invariant mass and transverse momentum. This is because there are not enough e^+e^- pairs in the measurement of the excess yield to apply a two dimensional correction (*i.e.*, as a function of invariant mass and transverse momentum). The effect of the STAR detector acceptance (cf_{acc}^{-1}) as a function of invariant mass and transverse momentum is shown in Fig. 6.4.

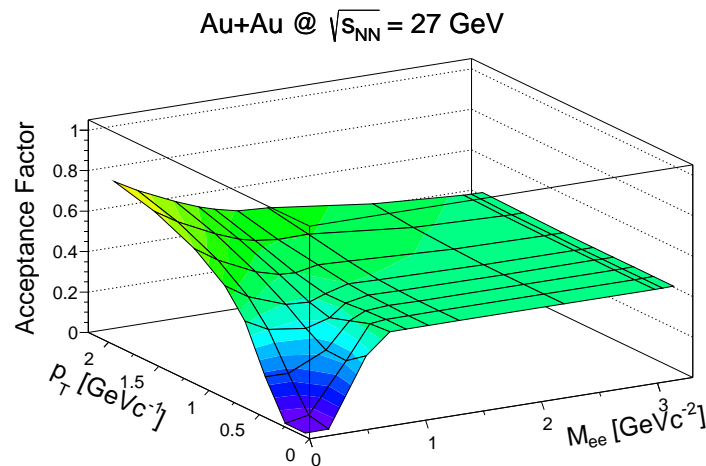


Figure 6.4 : The STAR detector acceptance correction factor as a function of invariant mass and transverse momentum.

The systematic uncertainties of the STAR detector acceptance correction are estimated by comparing the cf_{acc}^{-1} to the ratio of theoretical predictions of the excess yield within the STAR detector acceptance to predictions of the excess yield within

a corrected STAR detector acceptance cf_{accTH}^{-1} . The relative difference of cf_{acc}^{-1} and cf_{accTH}^{-1} with respect to cf_{acc}^{-1} is shown in Fig. 6.5. A conservative estimate for the systematic uncertainty of 6% is used because the largest relative difference in Fig. 6.5 is just under 6%.

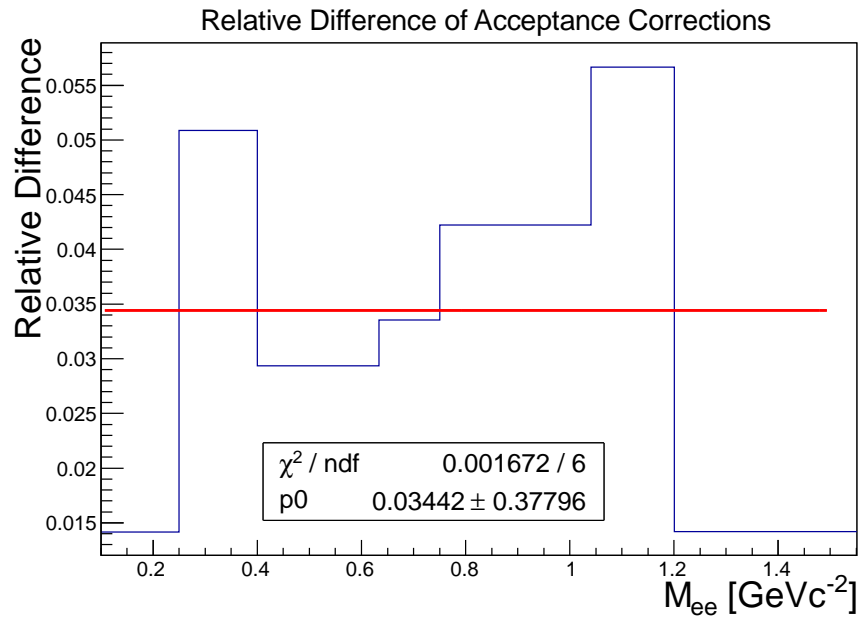


Figure 6.5 : The relative difference between the STAR detector acceptance effect from the γ^* Monte Carlo simulation in Sec. 4.5.4 and Rapp *et al.*'s STAR detector acceptance effect with respect to the γ^* Monte Carlo simulation. To be conservative, a flat 6% systematic uncertainty is used.

The acceptance-corrected e^+e^- excess yield, normalized to the charged particle multiplicities at mid-rapidity (dN_{ch}/dy), as a function of invariant mass is shown in Fig. 6.6. Normalization of the excess yield by dN_{ch}/dy removes the effect that the size of the colliding ions have on the yield. The $dN_{ch}/dy = 145$, which is derived from the summation of the dN/dy of π , K, and p in [19]. Comparisons to the measured normalized acceptance-corrected e^+e^- excess yield are made with the model calcula-

tions by Rapp *et al.*, which include e^+e^- pair contributions from the ρ with a spectral function that is modified by the hot, dense medium and the thermal radiation from the QGP. As shown in Fig. 6.6, the model calculations remain in agreement with the measurements within uncertainties.

Integrating the normalized excess yield of e^+e^- pairs over an invariant mass range is another way to capture and quantify the excess yield. If the normalized excess yield of e^+e^- pairs is integrated over 0.4-0.75 $\text{GeV}c^{-2}$, the normalized acceptance-corrected excess yield from the top 80% most central Au+Au collisions at $\sqrt{s_{NN}} = 27$ GeV is 5.11 ± 2.07 (stat.) ± 0.95 (sys.).

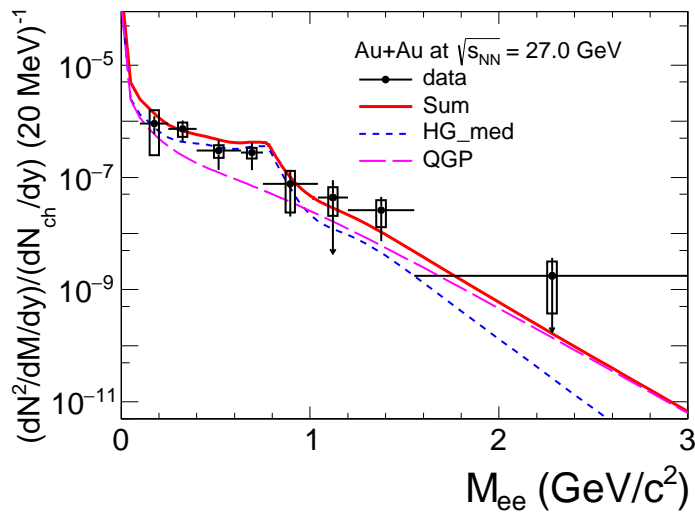


Figure 6.6 : The acceptance-corrected excess yields, normalized by dN_{ch}/dy at mid-rapidity, as a function of invariant mass shown as the black points with statistical and systematic uncertainties as the error bars and open boxes, respectively. Model calculations by Rapp *et al.* are also shown to make comparisons with the data. Their calculations (red line, “Sum”) consist of contributions from the ρ (blue short-dashed line, “HG_med”), which has a spectral function that is modified by the hot, dense medium, and the QGP (pink long-dashed line, “QGP”).

6.1 Beam Energy Scan Program Results

The production of e^+e^- pairs is also studied at other collision energies while maintaining the same experimental setup and colliding species. The data, as shown in Table 3.1, collected at $\sqrt{s_{NN}} = 19.6, 39,$ and 62.4 GeV provided powerful enough statistics to perform meaningful e^+e^- measurements in the low-mass region. The results on low-mass region of the production of e^+e^- in Au+Au collisions at $\sqrt{s_{NN}} = 19.6$ GeV have been published [37]; however, the findings in this thesis and the production of e^+e^- in Au+Au collisions at $\sqrt{s_{NN}} = 39$ and 62.4 GeV are in preparation of journal submission. Together, these measurements of e^+e^- are a systematic study of the low-mass region production of e^+e^- that fills in the collisional energy gap between measurements made at SPS energies [44, 15, 16] (*i.e.*, $\sqrt{s_{NN}} = 17.3$ GeV) and the top RHIC energy [17, 18, 38] (*i.e.*, $\sqrt{s_{NN}} = 200$ GeV), and provide a first systematic scan of the low-mass region excitation function over one order of $\sqrt{s_{NN}}$.

The corrected e^+e^- invariant mass spectrum in STAR acceptance in Au+Au collisions at $\sqrt{s_{NN}} = 19.6$ is shown in Fig. 6.7(left) [37] with the hadronic cocktail and the model calculations from Rapp *et.al.* In Fig. 6.7(right) [37], the normalized acceptance-corrected excess yield is shown as a function of invariant mass for STAR's Au+Au at $\sqrt{s_{NN}} = 19.6$ and 200 GeV and NA60's In+In at $\sqrt{s_{NN}} = 17.3$ GeV with model calculations by Rapp *et al.* for Au+Au collisions at $\sqrt{s_{NN}} = 19.6$ GeV. Notice in Fig. 6.7(right), the agreement between the measurements at $\sqrt{s_{NN}} = 19.6$ GeV and the model calculations.

The measurements of e^+e^- in Au+Au collisions at $\sqrt{s_{NN}} = 27, 39,$ and 62.4 GeV along with theory calculations are shown in Fig. 6.8. The left panel compares the hadronic cocktail (solid black curve) with the data (blue points) within the STAR detector acceptance as a function of invariant mass. Notice the excess of e^+e^- between

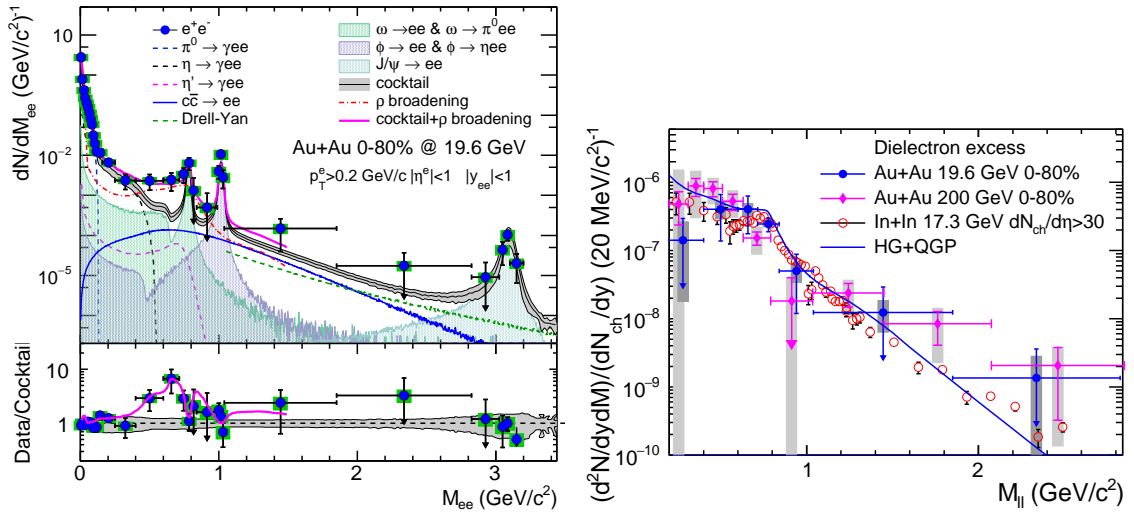


Figure 6.7 : (Left) The top panel contains the e^+e^- invariant mass spectrum in the STAR acceptance ($p_T^e > 0.2 \text{ GeV}c^{-1}$, $p_T^e < 3 \text{ GeV}c^{-1}$, $|\eta^e| < 1$, and $|Y^{ee}| < 1$) with a hadronic cocktail and calculations from Rapp *et al.* The bottom panel contains the ratio of data to cocktail as a function of invariant mass and the ratio of calculations from Rapp *et al.*+cocktail to cocktail as a function of invariant mass. The statistical and systematic uncertainties are represented by the error bars and green boxes, respectively. The hadronic cocktail uncertainties are represented by the gray band. (Right) The acceptance-corrected excess yields, which have been normalized by dN_{ch}/dy , as a function of invariant mass, with theory calculations. The excess yields in Au+Au at $\sqrt{s_{NN}} = 19.6 \text{ GeV}$ are from [37]. The excess yields in Au+Au at $\sqrt{s_{NN}} = 200 \text{ GeV}$ are from [17, 38]. The excess yields in In+In are from [16, 39]. Both figures are from [37].

the data and cocktail in the low mass region for each collision energy. The middle panel of Fig. 6.8 presents the enhancement (*i.e.*, data over cocktail) (blue points) as a function of invariant mass. Also shown in the middle panel of Fig. 6.8, the theory calculations added to the cocktail over the cocktail (red curve) as a function of invariant mass. There is agreement between the two curves of enhancement in the low mass region for all collision energies, given uncertainties. The right panel of Fig. 6.8 presents the acceptance-corrected excess yields, normalized by dN_{ch}/dy at mid-

rapidity, as function of invariant mass for the three collision energies (black points). Overlaid are the theory calculations for the expected ρ (blue dashed curve) and the QGP (pink dashed curve) e^+e^- contributions. These model contributions together give the *Sum* (sold red curve) and are consistent with the data measurements, given uncertainties.

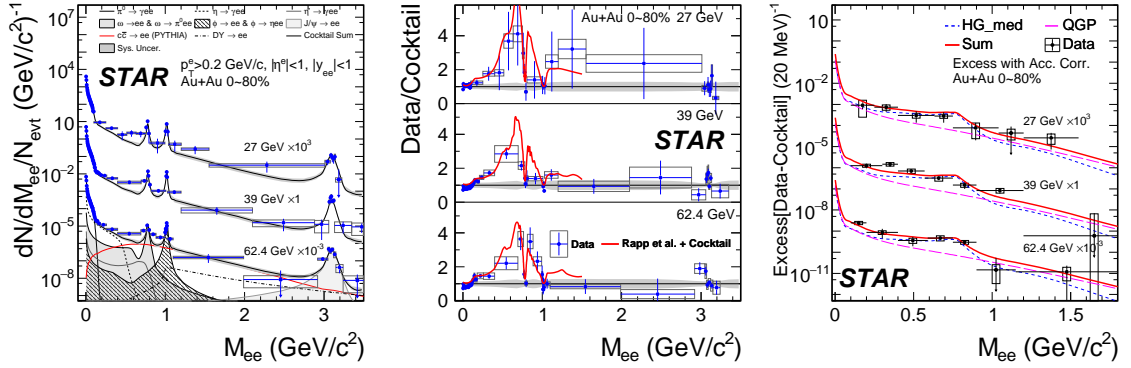


Figure 6.8 : (Left) The corrected e^+e^- invariant mass spectrum within the STAR acceptance for Au+Au collisions at $\sqrt{s_{NN}} = 27, 39,$ and 62.4 GeV with the hadronic cocktail for Au+Au at $\sqrt{s_{NN}} = 62.4$ GeV added for reference. (Middle) The ratio of the data to the cocktail as a function on invariant mass as represented by the blue points. The ratio of the cocktail plus contributions from the Rapp *et al.* calculations to the cocktail as a function of invariant mass as represented by the red curve. (Right) The acceptance-corrected excess yields, normalized by dN_{ch}/dy at mid-rapidity, as a function of invariant mass are shown as black points. Calculations by Rapp *et al.* are added to the cocktail to give the *Sum* of contributions to the e^+e^- invariant mass spectrum as shown by the red curve. The calculations for the contributions from the ρ , which is modeled with a spectral function that is modified by the medium, and the QGP. The statistical and systematic uncertainties are represented by the error bars and open boxes, respectively. Cocktail uncertainties are represented by the gray bands.

For the integrated excess yield of each beam energy scan collision energy, a χ^2 -test is performed to test the null hypothesis of no excess yield where only statistical uncertainties are considered. To consider the influence of the systematic uncertainties on the measurement of integrated excess yields, the χ^2 -tests are performed again, but

this time the excess yields are set at the lower limit determined by the systematic uncertainties. Table 6.1 lists the χ^2 , p-value, and σ found using a two-tailed z-test. These statistical results suggest that a statistically significant excess yield is observed during the Beam Energy Scan Program.

Table 6.1 : χ^2 -tests of the null hypothesis, no excess yield.

$\sqrt{s_{NN}}$ [GeV]	χ^2	p-value	σ
19.6	6.1185	0.0133775	2.2
27	6.0936	0.0135673	2.2
39	47.7766	4.77657e-12	>5
62.4	16.3333	5.31227e-5	3.5
19.6 (low sys.)	4.21421	0.0400867	1.7
27 (low sys.)	4.50231	0.033849	1.8
39 (low sys.)	30.6278	3.12581e-8	>5
62.4 (low sys.)	10.2123	0.00139506	2.9

A similar χ^2 -test is performed, where the calculations by Rapp *et al.* are integrated over the invariant mass range 0.4-0.75 GeVc⁻². The integrated calculations are used as the true value in the χ^2 -test, where only the statistical uncertainties on the integrated experimental measurements are considered; the results are presented in Table 6.2. The $\chi^2 = 4.70909$ corresponds to a p-value = 0.452405 and 1.65 σ based on a two-tailed z-test.

To study the possibility of a total excess yield dependence on system size (*i.e.*, dN_{ch}/dy), collision energy, and predicted lifetimes of the collision system, the acceptance-corrected excess yields normalized by dN_{ch}/dy are integrated from 0.4-0.75 GeVc⁻².

Table 6.2 : χ^2 -tests of Rapp *et al.* calculations as expected value.

$\sqrt{s_{NN}}$ [GeV]	χ^2
19.6	0.08181
27	1.98556
39	0.31195
62.4	0.87078
200	1.45899
Total	4.70909

The integrated normalized yields are shown as a function of collision energy in Fig. 6.9 as the closed markers. Corresponding integrated yields from theoretical calculations are also shown in Fig. 6.9 as the open markers. The theoretical calculations demonstrate a slight dependence on collision energy. The data measurements do not demonstrate a statistically significant dependence on collision energy, but are consistent with model calculations, within uncertainties.

The integrated acceptance-corrected excess yields, normalized by dN_{ch}/dy , are studied as a function dN_{ch}/dy to explore the possibility of a charged particle density dependence (and centrality or number of participants dependence), as shown in Fig. 6.10. Presented are the measurements from Au+Au collisions at $\sqrt{s_{NN}} = 19.6, 27, 39, 62.4, 200$ GeV at 0-80% centrality, Au+Au collisions at $\sqrt{s_{NN}} = 200$ GeV with centralities of 0-10%, 10-40%, and 40-80%, and In+In collisions at $\sqrt{s_{NN}} = 17.3$ GeV with $dN_{ch}/d\eta > 30$. The corresponding dN_{ch}/dy are listed in Table 6.3. As we observed in [37], the central Au+Au collisions at $\sqrt{s_{NN}} = 200$ GeV have a larger acceptance-corrected excess yield, normalized by dN_{ch}/dy , than the peripheral

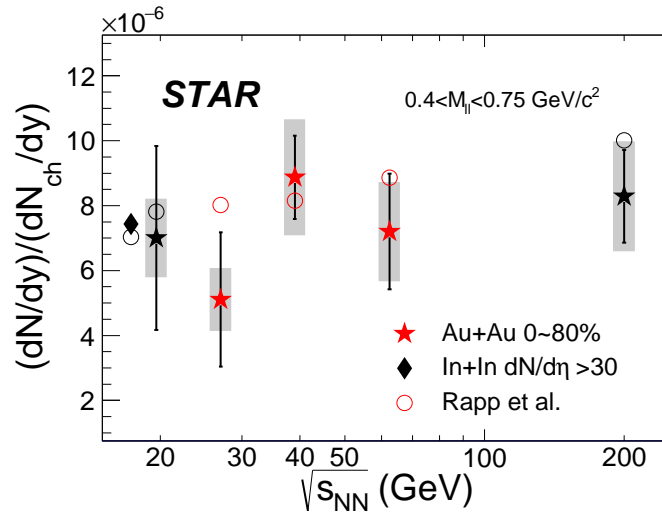


Figure 6.9 : The acceptance-corrected excess yields, normalized by dN_{ch}/dy , integrated over 0.4 to 0.75 $\text{GeV}c^{-2}$ as a function of collision energy (closed markers). The data points are from STAR's Au+Au collisions at $\sqrt{s_{NN}} = 19.6, 27, 39, 62.4,$ and 200 GeV and NA60's In+In collisions at $\sqrt{s_{NN}} = 17.3$ GeV. The statistical and systematic uncertainties are represented as the error bars and boxes, respectively. The corresponding model calculations by Rapp *et al.* are shown for comparison (open circles).

collisions of the same collision system and collisions at lower collision energies with a 0-80% centrality.

As mentioned in Sec. 2.3, the model by Rapp *et al.* relates the total e^+e^- excess yield, normalized by dN_{ch}/dy , to the lifetime of the fireball. To investigate a possible relationship between the fireball lifetime and the excess yield, the acceptance-corrected excess yields, normalized by dN_{ch}/dy , are integrated over the invariant mass range of 0.4 to 0.75 $\text{GeV}c^{-2}$ and plotted against predicted fireball lifetimes for a given collision system [13, 36] as shown in Fig. 6.11. The correspondence between the predicted lifetime and collision system (*e.g.*, Au+Au at $\sqrt{s_{NN}} = 27$ GeV) are given in Table 6.3. Also, shown in Fig. 6.11 are the predicted yields given by Rapp *et al.*

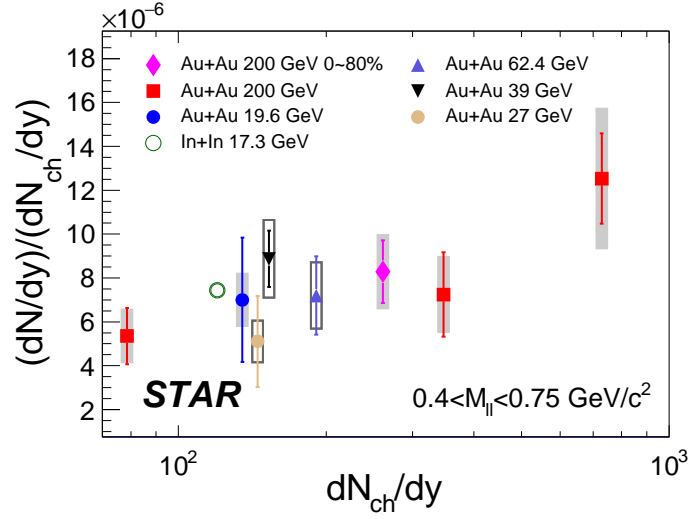


Figure 6.10 : The acceptance-corrected excess yields, normalized by dN_{ch}/dy , integrated over 0.4 to 0.75 $\text{GeV}c^{-2}$ as a function of dN_{ch}/dy . The data points are from STAR's Au+Au collisions at $\sqrt{s_{NN}} = 19.6, 27, 39, 62.4,$ and 200 GeV with 0-80% centrality, STAR's Au+Au collisions at $\sqrt{s_{NN}} = 200$ GeV with centralities of 40-80%, 10-40%, and 0-10% (red squares), and NA60's In+In collisions at $\sqrt{s_{NN}} = 17.3$ GeV. The statistical and systematic uncertainties are represented as the error bars and boxes, respectively.

integrated from 0.4 to 0.75 $\text{GeV}c^{-2}$ as a function of the predicted fireball lifetime. The measured excess yield demonstrates no statistically significant dependence on lifetime and appear to be systematically lower than theoretical calculations. However, there are large uncertainties on the measured yields, and the measured yields remain in agreement with the calculations.

6.2 Conclusions

In this thesis, I presented measurements of the e^+e^- invariant mass spectrum from Au+Au collisions at $\sqrt{s_{NN}} = 27$ GeV with a 0-80% centrality. These measurements are compared with theoretical calculations that include e^+e^- contributions from the

Table 6.3 : The fireball lifetimes given by model calculations [13, 36] and the corresponding collision systems. These are used in Fig. 6.11.

Lifetime (fm/c)	Species	$\sqrt{s_{NN}}$ (GeV)	Centrality	dN_{ch}/dy
6.8 ± 1.0	In+In	17.3	$dN_{ch}/d\eta > 30$	120
7.0	Au+Au	200	40-80%	78.6
7.7 ± 1.5	Au+Au	19.6	00-80%	135
8	Au+Au	27	00-80%	145
8.2	Au+Au	39	00-80%	153
9.2	Au+Au	62.4	00-80%	191
10.5 ± 2.1	Au+Au	200	00-80%	261
11.5	Au+Au	200	10-40%	347
14.5	Au+Au	200	00-10%	729

QGP and ρ (as discussed in detail in Sec. 2.3). Figures 6.2 and 6.3 show the model calculations describing the e^+e^- excess and enhancement in the STAR acceptance, respectively, which contain a ρ spectral function that is broadened in the hot, dense medium. The acceptance-corrected excess yields, normalized by dN_{ch}/dy , shown in Fig. 6.6 are also shown to be consistent with model calculations by Rapp *et al.* that include a broadening of the ρ spectral function in the medium. All of which support the claim that the ρ spectral function is modified by the medium.

The e^+e^- results from Au+Au collisions at $\sqrt{s_{NN}} = 27$ GeV are part of a larger study that systematically measured the e^+e^- pair production in the low invariant mass region as a function of collision energy for Au+Au systems. The Beam Energy Scan Program produced enough good Au+Au collisions to make a meaningful study

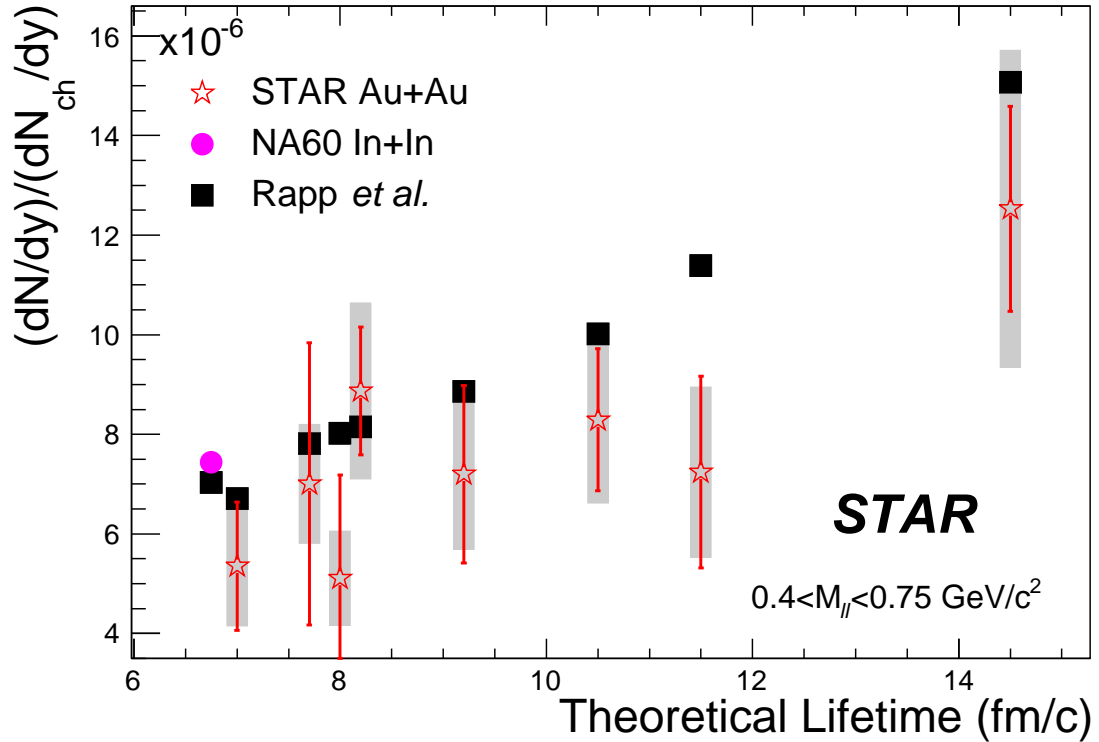


Figure 6.11 : The acceptance-corrected excess yields, normalized by dN_{ch}/dy , integrated over 0.4 to 0.75 $\text{GeV}c^{-2}$ as a function of predicted fireball lifetimes by Rapp *et al.* The data points are from STAR's Au+Au collisions at $\sqrt{s_{NN}} = 19.6, 27, 39, 62.4,$ and 200 GeV with 0-80% centrality, STAR's Au+Au collisions at $\sqrt{s_{NN}} = 200$ GeV with centralities of 40-80%, 10-40%, and 0-10% (red squares), and NA60's In+In collisions at $\sqrt{s_{NN}} = 17.3$ GeV. The predicted yields by Rapp *et al.*, normalized by dN_{ch}/dy , integrated from 0.4 to 0.75 $\text{GeV}c^{-1}$ are plotted against predicted fireball lifetimes for comparison. The statistical and systematic uncertainties are represented as the error bars and boxes, respectively.

of the production in the low-mass region at $\sqrt{s_{NN}} = 19.6, 27, 39,$ and 62.4 GeV. The previously published $\sqrt{s_{NN}} = 19.6$ GeV results, together with the $\sqrt{s_{NN}} = 27, 39,$ and 62.4 GeV results (part of an upcoming publication), fill in the order of magnitude gap in collision energy between the top SPS and top RHIC energies. Presented together, the e^+e^- measurements within the STAR acceptance exhibit an

excess of e^+e^- that can be described by a model that includes the broadening of the ρ spectral function by a hot, dense medium. This agreement between the data and the model is shown in Figs. 6.7 and 6.8. Also shown in the Figs. 6.7 and 6.8 are the acceptance-corrected excess yields, normalized by dN_{ch}/dy , described by the same model calculations. In Fig. 6.9, the data measurements do not rule out a constant integrated acceptance-corrected excess yield, normalized by dN_{ch}/dy , as a function of collision energy; however, the measurements are consistent with model calculations that show an increase in excess yields as the collision energy increases, given uncertainties. Without greater precision in the integrated excess yields, the flat trend in the integrated excess yields is not unexpected. As stated in Sec. 2.6, the total baryon density across these collision energies is relatively constant and the ρ spectral function depends primarily on ρ 's strong coupling to baryons instead of mesons. Hence, with the removal of the system size dependence (dN_{ch}/dy), the excess yields are not expected to vary greatly.

Figure 6.10 demonstrates that central (0-10% centrality) Au+Au collisions at $\sqrt{s_{NN}} = 200$ GeV have a higher integrated normalized acceptance-corrected excess yield than peripheral Au+Au collisions at $\sqrt{s_{NN}} = 200$ GeV and Au+Au collisions with a 0-80% at $\sqrt{s_{NN}} = 19.6, 27, 39,$ and 62.4 GeV. This is consistent with Rapp *et al.*'s model [79, 35, 80, 13, 36] that predicts a longer lifetime in more central collisions and thus, more excess production. Finally, the integrated acceptance-corrected excess yields, normalized by dN/dy , are shown as a function of theory lifetime in Fig. 6.11 along with corresponding model excess yield calculations. While a constant lifetime cannot be ruled out for the data measurements, the measurements are consistent with model calculations that demonstrate an increase in excess yield as lifetime increases, given uncertainties.

To summarize, an excess in the e^+e^- measurements is observed and is described by a model that incorporates a broadening of ρ 's spectral function, which is presented in Sec. 2.3. As mentioned in Ch. 2's Chiral Symmetry Restoration Observable (Sec. 2.3.2), Hohler and Rapp have been working on a model [14] that tries to establish indirectly an observation of chiral symmetry restoration. The model connects the ρ spectral function, which has been successful in describing the excess production of e^+e^- presented in this thesis, and an ansatz a_1 spectral function in hot, dense medium calculations. These calculations show the degeneracy of the spectral functions at $T = 170$ MeV, where the degeneracy of the ρ and a_1 are an observable of chiral symmetry restoration. Of course, this is an indirect way to try and claim that chiral symmetry restoration in heavy-ion collisions is observed. Nonetheless, it pushes us to see how this model can be tested further.

6.3 Future Studies

Better precision in the measurement of e^+e^- pairs is needed to claim a successful description of the e^+e^- -invariant mass spectrum by model calculations and to study dependencies with collision energy, dN_{ch}/dy , and fireball lifetime. In 2019 and 2020, Beam Energy Scan Phase II is scheduled to take place at RHIC. In the second phase of the Beam Energy Scan Program, collisions of Au+Au at $\sqrt{s_{NN}} = 7.7, 9.1, 11.5, 14.5,$ and 19.6 GeV with higher luminosities has been proposed. The new program will also usher in new and upgraded detectors at STAR, such as endcap Time-of-Flight (eTOF) system [130] and inner Time-Projection-Chamber (iTPC) upgrade [40]. The iTPC upgrade will replace the current inner TPC sector pad rows with a greater density of readout pads. This upgrade will lead to better measurements of the momentum and dE/dx resolutions and allows for forward tracking (at $|\eta| < 1.5$).

The eTOF system is comprised of MRPC modules from the Compressed Baryonic Matter (CBM) experiment at the Facility for Antiproton and Ion Research (FAIR). These MRPC modules are of similar technology as the MRPCs used in the TOF system. The eTOF system will cover $-1.6 < |\eta| < -1.1$ and extend the forward particle identification region. The extended forward coverage complements the iTPC and the pair of upgrades could be used in a similar fashion as the TPC and TOF are used to enable the identification of electrons in the low and intermediate momentum regions.

For future studies on e^+e^- production, the increase in luminosity and improved detectors will lead to an improvement in statistics and systematic uncertainties. For reference, the increase in luminosity will result in statistical uncertainties similar to the statistical uncertainty presented for the e^+e^- pair production in Au+Au collisions at $\sqrt{s_{NN}} = 200$ GeV with 0-80% centrality [17, 38]. Figure 6.12 illustrates the expected improvements from an increased luminosity and iTPC upgrade. In Fig. 6.12(left), the e^+e^- excess yields, as a function invariant mass for Au+Au collisions at $\sqrt{s_{NN}} = 19.6$ GeV as reported in [37], are shown. The blue points are the published measurements of the e^+e^- invariant mass spectrum. The black points represent the scenario where only the luminosity is increased and no iTPC upgrade is installed. This scenario results in an increase in statistics and hence, a decrease in statistical uncertainty. The red points represent the scenario where both the luminosity is increased and the iTPC has been implemented. In addition to the improved statistical uncertainty from the luminosity increase, the iTPC upgrade will reduce the systematics. The leading improvement in systematic uncertainties will be in the hadron rejection, or electron purity, as a result of the improved dE/dx resolution. It is with these improvements that competing models of ρ broadening, such as PHSD (Sec. 2.4) and Rapp *et al.* (Sec. 2.3), may be distinguished. Also in Fig. 6.12(left),

the solid red curve represents the model predictions by Rapp *et al.* with a ρ spectral function that broadens in the medium. The dashed pink curve represents the model predictions by Rapp *et al.* with a vacuum ρ spectral function. The dashed blue curve represents the model calculations by PHSD with a ρ spectral function that broadens in the medium. In Fig. 6.12(right), measurements of the acceptance-corrected excess yield, normalized by dN_π/dy , are shown as a function of collision energy (red points). Projected uncertainties with the iTPC for Phase II collision energies are shown as blue points. Predictions of e^+e^- production given by Rapp *et al.* (dashed red curve) and PHSD (shaded orange area) are shown too. The projected uncertainties present the possibility to test PHSD's prediction that excess yield will increase as the total baryon density increases at lower collision energies. Finally, the increased statistics means that we will be able to explore the dN_{ch}/dy dependence at each collision energy as performed with Au+Au collisions at $\sqrt{s_{NN}} = 200$ GeV. STAR should be able to reach as low as $dN_{ch}/dy = 27$ for Au+Au collisions at $\sqrt{s_{NN}} = 7.7$ GeV with a centrality between 40-80% and make a statistically significant e^+e^- invariant mass measurement. These improvements will lead to an exciting future program and build upon the results presented in this thesis.

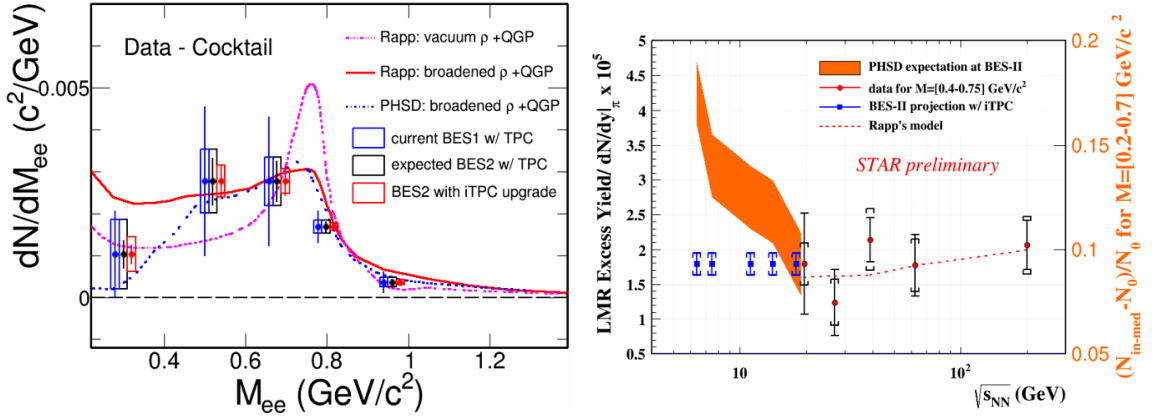


Figure 6.12 : (Left) The e^+e^- excess yield from Au+Au collisions at $\sqrt{s_{NN}} = 19.6$ GeV. (Right) The acceptance-corrected excess yields, normalized by dN_π/dy , integrated over 0.4 to 0.75 GeV/c^2 as a function of collision energy. The red points are actual measurements, while the blue points are the 19.6 GeV value projected on the Phase II collision energies with the expected uncertainties with iTPC and more collisions. The statistical and systematic uncertainties are represented by the error bars and open brackets, respectively. For details, please refer to the text. The left and right figures are from [40, 41], respectively.

Bibliography

- [1] F. Halzen and A. D. Martin, *Quarks & Leptons: An Introductory Course in Modern Particle Physics*. John Wiley & Sons, 1984. The authors noted that they are in a special debt to (now Professor) Paul Stevenson. Professor Stevenson has amazing notes on QFT.
- [2] C. Patrignani *et al.*, “Review of Particle Physics,” *Chinese Physics C*, vol. 40, no. 100001, 2016.
- [3] V. Koch, “Aspects of Chiral Symmetry,” *International Journal of Modern Physics E*, vol. 6, pp. 203–250, 1997.
- [4] L. Adamczyk *et al.*, “Studying the Phase Diagram of QCD Matter at RHIC,” 2014. <https://drupal.star.bnl.gov/STAR/starnotes/public/sn0598>.
- [5] S. Bass, “Microscopic Reaction Dynamics at SPS and RHIC.” Quark Matter Presentation, 2001.
- [6] K. A. Olive *et al.* Particle Data Group, 2015. <http://www.particleadventure.org/history-universe.html>.
- [7] J. Adams *et al.*, “Evidence from d +Au Measurements for Final-State Suppression of High- p_T Hadrons in Au+Au Collisions at RHIC,” *Physical Review Letters*, vol. 91, no. 072304, 2003.

- [8] X. Dong, S. Esumi, P. Sorensen, N. Xu, and Z. Xu, “Resonance decay effects on anisotropy parameters,” *Physics Letters B*, vol. 597, pp. 328–332, 2004.
- [9] J. Adams *et al.*, “Experimental and theoretical challenges in the search for the quark-gluon plasma: The STAR Collaboration’s critical assessment of the evidence from RHIC collisions,” *Nuclear Physics A*, vol. 757, pp. 102–183, 2005.
- [10] R. Chatterjee, L. Bhattacharya, and D. K. Srivastava, *Lecture Notes in Physics 785: The Physics of the QGP*, ch. Electromagnetic Probes. Springer-Verlag, 2010.
- [11] A. Drees, “Low Mass Dilepton and Photon Production at the CERN SPS,” in *Workshop Nuclear Matter in Different Phases and Transitions*, (Les Houches, France), April 1998.
- [12] B. Müller, “Hadronic signals of deconfinement at RHIC,” *Nuclear Physics A*, vol. 750, no. 1, pp. 84 – 97, 2005.
- [13] R. Rapp and H. van Hees, “Thermal dileptons as fireball thermometer and chronometer,” *Physics Letters B*, vol. 753, pp. 586–590, 2016.
- [14] P. Hohler and R. Rapp, “Is ρ -meson melting compatible with chiral restoration?,” *Physics Letters B*, vol. 731, pp. 103–109, 2014.
- [15] D. Adamová *et al.*, “Modification of the ρ meson detected by low-mass electron-positron pairs in central Pb-Au collisions at 158A GeV/c,” *Physics Letters B*, vol. 666, no. 5, pp. 425–429, 2008.
- [16] R. Arnaldi *et al.*, “NA60 results on thermal dimuons,” *The European Physical Journal C*, vol. 61, pp. 711–720, 2009.

- [17] L. Adamczyk *et al.*, “Dielectron Mass Spectra from Au+Au Collisions at $\sqrt{s_{NN}} = 200$ GeV,” *Phys. Rev. Lett.*, vol. 113, no. 2, p. 022301, 2014. [Addendum: *Phys. Rev. Lett.*113,no.4,049903(2014)].
- [18] A. Adare *et al.*, “Dielectron production in Au + Au collisions at $\sqrt{s_{NN}} = 200$ GeV,” *Phys. Rev. C*, vol. 93, p. 014904, Jan 2016.
- [19] L. Adamczyk *et al.*, “Bulk properties in relativistic heavy ion collisions from the Beam Energy Scan Program,” *Phys. Rev. C*, vol. XX, p. XXX, 2017. Submitted. arXiv:1701.07065.
- [20] B. I. Abelev *et al.*, “Systematic measurements of identified particle spectra in pp , $d + Au$, and $Au + Au$ collisions at the STAR detector,” *Phys. Rev. C*, vol. 79, p. 34909, 2009.
- [21] Image downloaded from RHIC’s flickr on January 30, 2017. <https://www.flickr.com/photos/brookhavenlab/7979381212/in/album-72157613690851651>.
- [22] A. Schmah and M. Schmah. The authors created this presentation of the detector sans the labels.
- [23] STAR Beam Beam Counter group. The front view drawing at <http://www.star.bnl.gov/public/bbc>.
- [24] W. J. Llope, J. Butterworth, *et al.*, “The STAR Vertex Position Detector,” *Nuclear Instruments and Methods in Physics Research A*, vol. 759, pp. 23–28, 2014.

- [25] C. Adler, A. Denisov, E. Garcia, M. Murray, H. Strobele, and S. White, “The RHIC Zero Degree Calorimeter,” *Nuclear Instruments and Methods in Physics Research A*, vol. 470, pp. 488–499, 2001.
- [26] M. Anderson *et al.*, “The STAR Time Projection Chamber: a Unique Tool for Studying High Multiplicity Events at RHIC,” *Nuclear Instruments and Methods in Physics Research A*, vol. 499, p. 659, 2003.
- [27] G. Eppley *et al.*, “Proposal for a Large Area Time of Flight System for STAR,” 2004. STAR Note 621, <http://www.star.bnl.gov/star/starlib/doc/www/sno/ice/sn0621.html>.
- [28] J. Butterworth, “Tof calibration,” in *STAR at Rice Group Meeting*, September 2013.
- [29] G. A. Alves *et al.*, “Forward cross sections for production of d^+ , d^0 , d_s , d^{*+} , and Λ_c in 250 gev π^\pm , k^\pm , and p interactions with nuclei,” *Phys. Rev. Lett.*, vol. 77, pp. 2388–2391, Sep 1996.
- [30] G. A. Alves *et al.*, “Erratum: Forward cross sections for production of d^+ , d^0 , d_s , d^{*+} , and Λ_c in 250 gev π^\pm , k^\pm , and p interactions with nuclei [phys. rev. lett. 77, 2388 (1996)],” *Phys. Rev. Lett.*, vol. 81, pp. 1537–1537, Aug 1998.
- [31] S. P. K. Tavernier, “Charmed and bottom flavoured particle production in hadronic interactions,” *Reports on Progress in Physics*, vol. 50, no. 11, p. 1439, 1987. and references therein.
- [32] L. Adamczyk *et al.*, “Measurements of D^0 and D^* production in $p+p$ collisions at $\sqrt{s}=200$ GeV,” *Phys. Rev. D*, vol. 86, p. 072013, Oct 2012.

- [33] A. Adare *et al.*, “Measurement of high- p_T single electrons from heavy-flavor decays in $p+p$ collisions at $\sqrt{s} = 200$ GeV,” *Phys. Rev. Lett.*, vol. 97, p. 252002, Dec 2006.
- [34] R. E. Nelson, R. Vogt, and A. D. Frawley, “Narrowing the uncertainty on the total charm cross section and its effect on the J/ψ cross section,” *Physical Review C*, vol. 87, p. 014908, 2013.
- [35] R. Rapp, “Dilepton Spectroscopy of QCD Matter at Collider Energies,” *Advances in High Energy Physics*, vol. 2013, no. 148253, pp. 1–17, 2013.
- [36] R. Rapp. Private Communications.
- [37] L. Adamczyk *et al.*, “Energy dependence of acceptance-corrected dielectron excess mass spectrum at mid-rapidity in Au+Au collisions at $\sqrt{s_{NN}} = 19.6$ and 200 GeV,” *Physics Letters B*, vol. 750, p. 64, 2015.
- [38] L. Adamczyk *et al.*, “Systematic Measurements of Dielectron Production in Au + Au Collisions at $\sqrt{s_{NN}} = 200$ GeV from the STAR Experiment,” *Physical Review C*, vol. 92, p. 024912, 2015.
- [39] H. J. Specht *et al.*, “Thermal Dileptons from Hot and Dense Strongly Interacting Matter,” *AIP Conference Proceedings*, vol. 1322, p. 1, 2010.
- [40] STAR Collaboration, “Technical Design Report for the iTPC Upgrade,” 2015. STAR Note 644, <https://drupal.star.bnl.gov/STAR/starnotes/public/sn0644>.
- [41] F. Geurts, “Dilepton measurements at rhic,” in *Erice School 2016: Nuclear Matter under Extreme Conditions-Relativistic Heavy-Ion Collisions*, September 2016.

- [42] A. Adare *et al.*, “Detailed measurement of the e^+e^- pair continuum in $p + p$ and Au+Au collisions at $\sqrt{s_{NN}} = 200$ GeV and implications for direct photon production,” *Physical Review C*, vol. 81, p. 034911, 2010.
- [43] L. G. Landsberg *et al.*, “ELECTROMAGNETIC DECAYS OF LIGHT MESONS,” *Physics Reports*, vol. 128, pp. 301–376, 1985.
- [44] G. Agakichiev *et al.*, “ e^+e^- -pair production in Pb-Au collisions at 158 GeV per nucleon,” *The European Physical Journal C*, vol. 41, pp. 475–513, 2005.
- [45] K. A. Olive *et al.*, “Review of Particle Physics,” *Chinese Physics C*, vol. 38, no. 090001, 2014.
- [46] D. Griffiths, *Introduction to Elementary Particles*. John Wiley & Sons, Inc., 1987.
- [47] M. Gell-Mann, “Symmetries of Baryons and Mesons,” *Physical Review*, vol. 125, no. 3, pp. 1067–1084, 1962.
- [48] B. L. Friman, C. Höhne, J. E. Knoll, S. K. Leupold, J. Randrup, R. Rapp, and P. Senger, eds., *The CBM Physics Book*. Lecture Notes in Physics 814, Springer-Verlag, 2010.
- [49] J. F. Donoghue, E. Golowich, and B. R. Holstein, *Dynamics of the Standard Model*. Cambridge University Press, 1992.
- [50] E. Fermi, *Notes on thermodynamics and statistics*. University of Chicago Press, 1966. A reproduction of his notes for a course taught in 1951-1952.
- [51] K. Fukushima and T. Hatsuda, “The phase diagram of dense qcd,” *Reports on Progress in Physics*, vol. 74, no. 1, p. 014001, 2011.

- [52] P. Jacobs and X.-N. Wang, “Matter in extremis: ultrarelativistic nuclear collisions at {RHIC},” *Progress in Particle and Nuclear Physics*, vol. 54, no. 2, pp. 443 – 534, 2005.
- [53] R. A. Soltz, I. Garishvili, M. Cheng, B. Abelev, A. Glenn, J. Newby, L. A. L. Levy, and S. Pratt, “Constraining the initial temperature and shear viscosity in a hybrid hydrodynamic model of $\sqrt{s_{NN}} = 200$ gev au+au collisions using pion spectra, elliptic flow, and femtoscopic radii,” *Phys. Rev. C*, vol. 87, p. 044901, Apr 2013.
- [54] J.-Y. Ollitrault, “Relativistic hydrodynamics for heavy-ion collisions,” *European Journal of Physics*, vol. 29, pp. 275–302, 2008.
- [55] J. C. Collins and M. J. Perry, “Superdense matter: Neutrons or asymptotically free quarks?,” *Phys. Rev. Lett.*, vol. 34, pp. 1353–1356, May 1975.
- [56] G. Baym and S. Chin, “Can a neutron star be a giant mit bag?,” *Physics Letters B*, vol. 62, no. 2, pp. 241 – 244, 1976.
- [57] P. Braun-Munzinger and J. Stachel, “The quest for the quarkgluon plasma,” *Nature*, vol. 448, pp. 302–309, 2007.
- [58] M. L. Miller, K. Reygers, S. J. Sanders, and P. Steinberg, “Glauber Modeling in High-Energy Nuclear Collisions,” *Annual Review of Nuclear and Particle Science*, vol. 57, pp. 205–243, 2007.
- [59] D. d’Enterria and B. Betz, *Lecture Notes in Physics 785: The Physics of the QGP*, ch. High- p_T Hadron Suppression and Jet Quenching. Springer-Verlag, 2010.

- [60] P. Braun-Munzinger, I. Heppe, and J. Stachel, “Chemical equilibration in Pb+Pb collisions at the SPS,” *Physics Letters B*, vol. 465, pp. 15–20, 1999.
- [61] F. Karsch, “Lecture Notes in Physics,” vol. 583, p. 209, 2002.
- [62] R. Vogt, *Ultrarelativistic Heavy-Ion Collisions*. Elsevier, 2007.
- [63] M. Creutz, *Quarks, gluons and lattices*. Cambridge University Press, 1983.
- [64] J. B. Kogut, “An introduction to lattice gauge theory and spin systems,” *Reviews of Modern Physics*, vol. 51, no. 4, pp. 659–713, 1979.
- [65] J. B. Kogut, “The lattice gauge theory approach to quantum chromodynamics,” *Reviews of Modern Physics*, vol. 55, no. 3, pp. 775–836, 1983.
- [66] K. G. Wilson, “Confinement of quarks,” *Physical Review D*, vol. 10, no. 8, pp. 2445–2459, 1974.
- [67] L. Adamczyk *et al.*, “Direct virtual photon production in Au+Au collisions at $\sqrt{s_{NN}} = 200$ GeV,” *Phys. Lett. B*, vol. TBD, p. TBD, 2016.
- [68] A. Adare *et al.*, “Enhanced production of direct photons in Au + Au collisions at $\sqrt{s_{NN}} = 200$ GeV and implications for the initial temperature,” *Phys. Rev. Lett.*, vol. 104, p. 132301, Mar 2010.
- [69] J. Kapusta, P. Lichard, and D. Seibert, “High-energy photons from quark-gluon plasma versus hot hadronic gas,” *Physical Review D*, vol. 44, pp. 2774–2788, Nov 1991.
- [70] J. Kapusta, P. Lichard, and D. Seibert, “Erratum: High-energy photons from quark-gluon plasma versus hot hadronic gas,” *Phys. Rev. D*, vol. 47, pp. 4171–4171, May 1993.

- [71] T. Sakaguchi, “Thermal photon and Dilepton results from PHENIX,” in *RHIC & AGS Annual Users’ Meeting*, 2015.
- [72] T. Matsui and H. Satz, “ J/ψ suppression by quark-gluon plasma formation,” *Phys. Lett. B*, vol. 178, pp. 417–422, 1986.
- [73] S. Chatrchyan *et al.*, “Measurement of isolated photon production in pp and PbPb collisions at $\sqrt{s_{NN}} = 2.76$ TeV,” *Phys. Lett. B*, vol. 710, pp. 256–277, 2012.
- [74] R. Rapp and H. van Hees, “Thermal Electromagnetic Radiation in Heavy-Ion Collisions,” *European Physics Journal A*, vol. 52, p. 257, 2016.
- [75] G. David, R. Rapp, and Z. Xu, “Electromagnetic probes at RHIC-II,” *Physics Reports*, vol. 462, pp. 176–217, 2008.
- [76] G. E. Brown and M. Rho, “Scaling Effective Lagrangians in a Dense Medium,” *Physical Review Letters*, vol. 66, pp. 2720–2723, May 1991.
- [77] G. E. Brown and M. Rho, “Chiral Restoration in Hot And/Or Dense Matter,” *Physics Reports*, vol. 269, pp. 333–380, 1996.
- [78] R. Rapp and J. Wambach, “Chiral symmetry restoration and dileptons in relativistic heavy-ion collisions,” in *Advances in Nuclear Physics* (J. W. Negele and E. Vogt, eds.), pp. 1–205, Boston, MA: Springer US, 2002.
- [79] R. Rapp and J. Wambach, “Low-mass dileptons at the CERN-SpS: evidence for chiral restoration?,” *European Physical Journal A*, vol. 6, pp. 415–420, 1999.
- [80] R. Rapp, “Signatures of thermal dilepton radiation at ultrarelativistic energies,” *Physical Review C*, vol. 63, no. 054907, pp. 1–13, 2001.

- [81] R. Rapp, J. Wambach, and H. van Hess, “The chiral restoration transition of QCD and low mass dileptons,” in *Relativistic Heavy Ion Physics* (R. Stock, ed.), vol. 23 of *Group I: Elementary Particles, Nuclei and Atoms*, ch. 4, pp. 1–37, Springer-Verlag, 2010.
- [82] O. Linnyk, E. L. Bratkovskaya, and W. Cassing, “Effective QCD and transport description of dilepton and photon production in heavy-ion collisions and elementary processes,” *Progress in Particle and Nuclear Physics*, vol. 87, pp. 50–115, 2016.
- [83] W. Cassing and E. L. Bratkovskaya, “Parton-hadron-string dynamics: An off-shell transport approach for relativistic energies,” *Nuclear Physics A*, vol. 831, pp. 215–242, 2009.
- [84] E. L. Bratkovskaya, W. Cassing, V. P. Konchakovski, and O. Linnyk, “Parton-Hadron-String Dynamics at relativistic collider energies,” *Nuclear Physics A*, vol. 856, pp. 162–182, 2011.
- [85] O. Linnyk, W. Cassing, J. Manninen, E. L. Bratkovskaya, and C. M. Ko, “Analysis of dilepton production in Au+Au collisions at $\sqrt{s_{NN}} = 200$ GeV within the parton-hadron-string dynamics transport approach,” *Physical Review C*, vol. 85, no. 024910, pp. 1–10, 2012.
- [86] T. H. R. Skyrme, “A Unified Field Theory of Mesons and Baryons,” *Nuclear Physics*, vol. 31, pp. 556–569, 1962.
- [87] J. Ellis *Nuclear Physics*, vol. B22, p. 478, 1970.
- [88] K. Kawarabayashi and M. Suzuki, “Partially conserved axial-vector current and the decays of vector mesons,” *Phys. Rev. Lett.*, vol. 16, p. 255, 1966.

- [89] Riazuddin and Fayyazuddin, “Algebra of Current Components and Decay Widths of ρ and K^* Mesons,” *Phys. Rev.*, vol. 147, p. 1071, 1966.
- [90] I. Zahed and G. E. Brown, “The Skyrme Model,” *Physics Reports*, vol. 142, p. 1, 1986.
- [91] M. Rho, “Axial currents in nuclei and the skyrmion size,” *Phys. Rev. Lett.*, vol. 54, p. 767, 1988.
- [92] G. E. Brown and M. Rho, “On the manifestation of chiral symmetry in nuclei and dense nuclear matter,” *Physics Reports*, vol. 363, pp. 85–171, 2002.
- [93] E. L. Feinberg, “Direct Production of Photons and Dileptons in Thermodynamical Models of Multiple Hadron Production,” *Il Nuovo Cimento*, vol. 34A, pp. 391–412, August 1976.
- [94] L. D. McLerran and T. Toimela, “Photon and dilepton emission from the quark-gluon-plasma: Some general considerations,” *Physical Review D*, vol. 31, pp. 545–563, February 1985.
- [95] J. Sakurai, *currents and mesons*. University of Chicago Press, 1969.
- [96] M. Urban, M. Buballa, R. Rapp, and J. Wambach, “Momentum dependence of the pion cloud for ρ -mesons in nuclear matter,” *Nuclear Physics A*, vol. 641, pp. 433–460, 1998.
- [97] H. van Hees and R. Rapp, “Dilepton radiation at the CERN super-proton synchrotron,” *Nuclear Physics A*, vol. 806, pp. 339–387, 2008.
- [98] H.-T. Ding, A. Francis, O. Kaczmarck, F. Karsch, E. Laermann, and W. Soeldner, “Thermal dilepton rate and electrical conductivity: An analysis of vector

- current correlation functions in quenched lattice QCD,” *Physical Review D*, vol. 83, no. 3, pp. 1–17, 2011.
- [99] M. He, R. Fries, and R. Rapp, “Ideal Hydrodynamics for bulk and multistrange hadrons in $\sqrt{s_{NN}} = 200$ A GeV Au-Au collisions,” *Physical Review C*, vol. 85, no. 044911, pp. 1–9, 2012.
- [100] P. F. Kolb, J. Sollfrank, and U. Heinz, “Anisotropic transverse flow and the quark-hadron phase transition,” *Physical Review C*, vol. 62, no. 054909, 2000.
- [101] P. F. Kolb and R. Rapp, “Transverse flow and hadrochemistry in Au+Au collisions at $\sqrt{s_{NN}} = 200$ GeV,” *Physical Review C*, vol. 67, no. 044903, 2003.
- [102] S. A. Bass, M. Belkacem, M. Bleicher, M. Brandstetter, L. Bravina, C. Ernst, L. Gerland, M. Hofmann, S. Hofmann, J. Konopka, G. Mao, L. Neise, S. Soff, C. Spieles, H. Weber, L. A. Winkelmann, H. Stöcker, W. Greiner, C. Hartnack, J. Aichelin, and N. Amelin, “Microscopic Models for Ultrarelativistic Heavy Ion Collisions,” *Progress in Particle and Nuclear Physics*, vol. 41, pp. 225–370, 1998.
- [103] B. Anderson, G. Gustafson, G. Ingelman, and T. Sjöstrand, “Parton fragmentation and string dynamics,” *Phys. Rept.*, vol. 97, p. 31, 1983.
- [104] T. Sjöstrand, P. Edén, C. Friberg, L. Lönnblad, G. Miu, S. Mrenna, and E. Norrbin, “High-energy-physics event generation with PYTHIA 6.1,” *Computer Physics Communications*, vol. 135, pp. 238–259, 2001.
- [105] Z.-. W. Lin, C. M. Ko, B.-. A. Li, B. Zhang, and S. Pal, “Multiphase transport model for relativistic heavy ion collisions,” *Physical Review C*, vol. 72, no. 064901, pp. 1–29, 2005.

- [106] W. Cassing, “From Kadanoff-Baym dynamics to off-shell parton transport,” *European Physical Journal Special Topics*, vol. 168, pp. 3–88, 2009.
- [107] W. Ehehalt and W. Cassing, “Relativistic transport approach for nucleus-nucleus collisions from SIS to SPS energies,” *Nuclear Physics A*, vol. 602, pp. 449–486, 1996.
- [108] O. Linnyk, “Dilepton production by dynamical quasi-particles in the strongly interacting quarkgluon plasma,” *Journal of Physics G: Nuclear and Particle Physics*, vol. 38, no. 025105, pp. 1–25, 2011.
- [109] O. Linnyk, S. Leupold, and U. Mosel, “Quark initial state interaction in deep inelastic scattering and the Drell-Yan process,” *Physical Review D*, vol. 71, no. 034009, pp. 1–14, 2005.
- [110] O. V. Doce, “Measurements of the dielectron continuum in pp, p-pb, and pb-pb collisions with alice at the lhc,” in *Quark Matter*, 2017.
- [111] G. Charpak. Discovered/invented in 1968 and awarded the Nobel Prize in 1992.
- [112] H. Bichsel, “Energy loss in thin layers of argon.” STAR Note 418, <http://www.star.bnl.gov/star/starlib/doc/www/sno/ice/sn0418.html>.
- [113] H. Bichsel, “Comparison of Bethe-Bloch and Bichsel Functions.” STAR Note 439, <http://www.star.bnl.gov/star/starlib/doc/www/sno/ice/sn0439.html>.
- [114] H. Masui and A. Schmah. <http://www.star.bnl.gov/cgi-bin/protected/cvsweb.cgi/offline/users/hmasui/StRefMultCorr/>, 2011. Information on the StRefMultCorr package and simulations may be found at the following location:

<http://www.star.bnl.gov/protected/common/common2011/centrality/27GeV/>.

For those with the proper credentials, the source code may be found in the listed StRefMultCorr directory.

- [115] L. Adamczyk *et al.*, “Di-electron spectrum at mid-rapidity in $p + p$ collisions at $\sqrt{s} = 200$ GeV,” *Physical Review C*, vol. 86, p. 024906, 2012.
- [116] A. Poskanzer and S. Voloshin, “Methods for analyzing anisotropic flow in relativistic nuclear collisions,” *Physical Review C*, vol. 58, p. 1671, 1998.
- [117] R. Brun, R. Hagelberg, M. Hansroul, and J. C. Lassalle, *Simulation program for particle physics experiments, GEANT: user guide and reference manual*. CERN, 1978. <https://cds.cern.ch/record/118715?ln=en>.
- [118] M. Matsumoto and T. Nishimura, “A 623-dimensionally equidistributed uniform pseudorandom number generator,” *ACM Transactions of Modeling and Computer Simulation*, vol. 8, p. 3, 1998.
- [119] N. M. Kroll and W. Wada, “Internal Pair Production Associated with the Emission of High-Energy Gamma Rays,” *Physical Review*, vol. 98, no. 5, pp. 1355–1359, 1955.
- [120] R. Arnaldi *et al.*, “Study of the electromagnetic transition form-factors in $\eta \rightarrow \mu^+ \mu^- \gamma$ and $\omega \rightarrow \mu^+ \mu^- \pi^0$ decays with NA60,” *Physics Letters B*, vol. 667, pp. 260–266, 2009.
- [121] M. N. Achasov *et al.*, “Study of conversion decays $\phi \rightarrow \eta e^+ e^-$ and $\eta \rightarrow \gamma e^+ e^-$ in the experiment with SND detector at VEPP-2M collider,” *Physics Letters B*, vol. 504, pp. 275–281, 2001.

- [122] T. Ullrich and D. Irscher, “GENESIS.” unpublished.
- [123] H. Sako, “GENESIS.” GSI Technical Report 03-24, CERES Collaboration, unpublished, 2000.
- [124] S. Damjanovic, “GENESIS.” unpublished, 2003.
- [125] Z. Tang, Y. Xu, L. Ruan, G. van Buren, F. Wang, and Z. Xu, “Spectra and radial flow in relativistic heavy ion collisions with Tsallis statistics in a blast-wave description,” *Physical Review C*, vol. 79, p. 051901(R), 2009.
- [126] C. Tsallis, “Possible Generalization of Boltzmann-Gibbs Statistics,” *Journal of Statistical Physics*, vol. 52, no. 1/2, pp. 479–487, 1998.
- [127] L. Adamczyk *et al.*, “Energy dependence of J/ψ production in Au+Au collisions at $\sqrt{s_{NN}} = 39, 62.4$ and 200 GeV,” *Physics Letters B*, vol. 771, 2017.
- [128] J. E. Gasier. PhD thesis, 1982. SLAC-R-255.
- [129] “Number of collisions as a function of centrality for Au+Au collisions at $\sqrt{s_{NN}} = 27$ GeV.” http://www.star.bnl.gov/protected/common/common2011/centrality/27GeV/table/table_Ncoll_vs.centricity_systematicerror.txt.
- [130] STAR Collaboration and CBM Collaboration, “Physics Program for the STAR/CBM eTOF Upgrade,” 2016. arXiv:1609.05102.